Solid-State NMR Studies of the Guest Molecules in Urea Inclusion Compounds

Von der Fakultät Chemie der Universität Stuttgart Zur
Erlangung der Würde eines Doktors der Naturwissenschaften
(Dr. rer. nat.) genehmigte Abhandlung

vorgelegt von

Xiaorong Yang

aus Sichuan, China

Hauptberichter: Prof. Dr. K. Müller
Mitberichter: Priv.–Doz. Dr. G. Majer
Tag der mündlichen Prüfung: 26.02.2007

Institut für Physikalische Chemie der Universität Stuttgart
2007

Acknowledgement

I am very grateful to many individuals who gave me active support in different ways during this thesis work.

I would like to express my sincere thanks firstly to Prof. Dr. Klaus Müller for providing me such an interesting research field. I thank him for his invaluable advice and guidance throughout these years of research.

I would also thank Priv.-Doz. Dr. Günter Majer for his role as co-examiner and for the corrections of the doctoral thesis. I am grateful to Prof. Dr. Helmut Bertagnolli for taking the chair in the examination board.

I want to acknowledge my colleagues at the University of Stuttgart, Dr. Thomas Handel and Dr. Jorge Antonio Villanueva Garibay for introducing me to the NMR instrument and for their help in lineshape simulations. My thanks are extended to Dr. Shashikala Neumann-Singh, Dr. René Lehnert, Dr. Frank Berger, Dr. Tillmann Viefhaus, Dr. Gokulakrishnan Srinivasan, Dr. Fabrizia Poli, M.Sc. Otgontuul Tsetsgee, M.Sc. Kamalakannan Kailasam, M.Sc. Christiane Heuber, M.Sc. Lida Ghassemzadeh, M.Sc. Poonkodi Balasubramaniyan and Mr. Keisuke Watanabe for their help and suggestions.

I would like to thank Mrs. Gabi Bräuning and Ms. Annette Hirtler for their help in sample preparations, Mr. Walter Ottmüller, Mr. Jochen Graf and Mr. Peter Haller for mechanical workshop support, Mr. Jürgen Hußke for electronical help and Mr. Werner Hopf for all the glass stuff. Many thanks deliver to Mrs. Inge Blankenship for her assistance in administrative works as well.

The work was funded by the Graduate College (*Modern Methods of Magnetic Resonance in Materials Science*) and IPC. I am grateful to their support.

Finally, I want to express my heartfelt gratitude to my family, especially to my husband, and my friends for their enormous support in every aspect of living and working.

Contents

Chapter 1 Introduction

Inclusion compounds can be formed by various types of organic or inorganic host components, such as urea, thiourea, cyclophosphazenes or cyclodectrins. Due to the high selectivity with respect to the guest molecules, inclusion compounds are of great importance in pure and applied chemistry [1-3]. Moreover, inclusion compounds can serve as model systems for the study of molecules under very restricted spatial conditions, from which information about the molecular interactions among various components can be obtained. The most prominent examples for host systems are urea and thiourea, which both form hexagonal channel structures. Primarily they differ by the average diameter of the host channels, resulting in a different selectivity for the enclathrated guest species. The urea channels are of smaller diameter, and thus favour the inclathration of n-alkanes and n-alkane derivatives while bulkier species remain excluded [4-9].

During recent years, inclusion compounds have been studied in great detail, addressing mainly the structural properties or the dynamic behavior of the guest species [4-11], i.e. many efforts to explore the thermal and structural properties of the host lattice as well as the dynamic and ordering features of the guest species have been reported [12-16].

The study of molecular motions in condensed matter is of fundamental importance, for instance, for the understanding of transport phenomena or of the role that microscopic dynamics plays in determining bulk physical properties [17-19]. A wide range of techniques have been applied to investigate the dynamic properties of urea inclusion compounds, including solid-state NMR spectroscopy [20-26], incoherent quasi-elastic neutron scattering [27-29], EPR spectroscopy [30-32], molecular dynamics simulation [33], Raman spectroscopy [34], IR spectroscopy [35], dielectric loss spectroscopy [23] and X-ray diffraction [36-38]. The vast majority of these

investigations have probed the dynamic properties of the guest molecules [20-32], and some studies about the dynamics of the urea molecules have also been done [39-43]. Among these different techniques for studying molecular motions, dynamic NMR spectroscopy is well established because various pulse experiments are available, which give access to different motional time-scales. Hence, from the combined data analysis of relaxation, line shape, and stimulated echo experiments, molecular motions with motional rate across several orders of magnitude can be followed [6, 7, 44-46]. ^{2}H NMR studies on selectively deuterated compounds have demonstrated their particular applicability since the data analysis is simplified by the presence of only one dominant magnetic interaction, namely the quadrupolar interaction [45, 46]. In the past, dynamic ^{2}H NMR spectroscopy was successfully employed during the molecular characterization of quite different materials, such as molecular and liquid crystals, polymers, biomembranes, guest-host systems, etc [4, 6, 46-48].

Dynamic ^{2}H NMR studies for urea inclusion compounds containing alkane guests have been performed extensively [7, 49-52]; attentions were also paid to urea inclusion compounds comprising functionalized alkane guest molecules [4, 8, 53]. In this thesis work we primarily deal with the conformational order and dynamic properties of several bromoalkanes, such as 1,6-dibromohexane and 1,10-dibromodecane, in their urea inclusion compounds. Although ^{2}H NMR studies for 1,6-dibromohexane-d_4/urea [8] and 1,10-dibromodecane-d_{20}/urea [53] inclusion compounds have been reported, quantitative studies about the dynamic properties of these urea guest molecules are still missing.

^{2}H NMR spectroscopy on perdeuterated 1,10-dibromodecane-d_{20}/urea suggested [53] that all CD_2 groups experience the same dynamics – rotational diffusion in a six-fold cosine potential. However in the temperature range ca. 151 – 200 K, the experimental spectra could not be reproduced due to additional broadening.

In the first part of this thesis, investigations of UICs with 1,10-dibromodecane and

1,11-dibromoundecane, both are selectively deuterated at two end positions, are reported. ^{2}H NMR spectroscopy is employed to investigate the dynamic properties of guest molecules in these systems. By assuming appropriate motional models, the analysis of temperature-dependent experiments, comprising line shape, relaxation measurements, provides an insight into the dynamic characteristics of the guest molecules. The kinetic parameters are derived on the basis of a quantitative description of the guest molecular dynamics. In addition, ^{1}H MAS and ^{13}C CP/MAS NMR studies (variable spin rate spectra, variable temperature T_1 and $T_{1\rho}$ relaxation measurements) are performed and the relevant information about the structural and dynamic characteristics of samples with non-deuterated guests in urea and urea-d_4 is derived.

It is known that the urea inclusion compound (UIC) with 1,6-dibromohexane [54, 55] differs in several aspects from most other UICs, as for instance UICs with long-chain α,ω-dibromoalkanes $Br(CH_2)_nBr$ (n = 7 – 11) [9] or n-alkanes $CH_3(CH_2)_nCH_3$ ($n \geq 8$) [12-14]. ^{2}H NMR line shape was employed previously to determine the dynamics of selectively deuterated 1,6-dibromohexane in urea [8], and to extract the kinetic parameters. However, it turned out that the overall effects are rather small, since the motional correlation times fall in the fast exchange limit, and are thus outside the sensitive range of line shape effects [5-7, 56].

The second part of this work presents a comprehensive variable temperature ^{2}H NMR study on two samples of 1,6-dibromohexane/urea with guest molecules deuterated either at the α- or β-position, and, for the first time, a comprehensive relaxation study of this system is performed. The data analysis primarily relies on spin-lattice relaxation data (T_{1Z} and T_{1Q}) which turn out to match the time-scale of the guest motions. It is shown that a data analysis, comprising relaxation times as well as relaxation time anisotropy, provides consistent and reliable results for the gauche-gauche exchange dynamics of the guest species. Additionally, ^{13}C CP/MAS and ^{1}H MAS NMR studies (variable spin rate spectra, variable temperature T_1 and $T_{1\rho}$

relaxation measurements) are performed, for the first time, on samples with non-deuterated guests in urea and urea-d_4. It is demonstrated that the derived data from these additional studies agree with those employed during the ^{2}H NMR data analysis. Furthermore, additional information about the structural and dynamic features of these materials is obtained.

For urea inclusion compounds containing asymmetric guest species $X(CH_2)_nY$, it is possible to arrange the guest molecules in three different ways, i.e., with the end groups as, Y…..Y (HH), X…..Y (HT) and X…..X (TT). High-resolution ^{13}C solid-state NMR is suitable for quantitative studies on the properties of these systems [57, 58]. Since rapid motions of the guests give rise to sharp NMR lines, it is possible to use the resonances of the terminal functional groups to identify the HH, HT and TT sites. The ^{13}C NMR chemical shift values of n-alkanes, as well as of substituted alkanes were also employed for the structural characterizations of these UIC compounds [11, 25].

In the third part of the present work, the structural properties of the asymmetric guest, 1-bromodecane, in urea are studied by ^{1}H MAS and ^{13}C CP MAS NMR spectroscopy. Dynamic ^{2}H NMR spectroscopy, including variable temperature ^{2}H NMR line shape, spin-spin (T_2) and spin-lattice (T_{1Z} and T_{1Q}) relaxation studies, is used to explore the dynamic properties of the guests. A qualitative analysis of the experimental data provides a clear picture about the arrangement, dynamics and conformation of the guest molecules in the urea nano-channels. Moreover, a comparison between the obtained results and those from the dibromoalkane/urea is done.

In organic chemical reactions and the assemblies of supermolecules, the functional groups play an important role. The study of guest molecules isolated by urea channels has the potential to provide the interaction strength between functional groups, which can be used to optimize the reactions. Hence, the last part of this thesis work is dedicated to the understanding of the effect of the end functional group on the local

structure and dynamics of the guest molecules in nano-channels of the urea. Urea inclusion compounds with n-alkane (n-hexadecane, decane and pentadecane) or n-alkane of different di- or mono-substituting end functional groups (–COOH, –F) are investigated by ^{1}H MAS and ^{13}C CP MAS NMR spectra and spin lattice relaxation experiments (^{1}H $T_{1\rho}$, ^{13}C $T_{1\rho}$ and ^{13}C T_1). In addition, variable temperature spin-lattice relaxation experiments in the rotating frame (^{13}C $T_{1\rho}$) are performed on samples with the guests of hexadecane and pentadecane in urea or urea-d_4. By analyzing the experimental data, dynamic properties of the guest molecules in the microsecond time scale are derived. The dynamic parameters are compared with the available data from the ^{2}H NMR studies.

In summary, the present solid state NMR studies provide new information about the dynamics and ordering of the guest molecules in urea inclusion compounds which indirectly also affect the guest-guest and the guest-host interactions in these systems.

Chapter 2 Systems

2.1 Urea inclusion compounds

Ever since the urea inclusion compounds (UICs) were discovered accidentally by Bengen in 1940 [59-61] while studying the effects of urea on proteins in pasteurized milk, numerous studies have been performing on the inclusion compounds of urea, thiourea and selenourea. With respect to the structure, Smith's crystal structure obtained from X-ray diffraction investigation on the hexadecane–UICs [36, 62] is thought as the conventional host structure found for most UICs. By extensive hydrogen-bonds the urea molecules are connected to form helical ribbons, which are woven together to form an array of linear, hexagonal channels that can comprise guest molecules (figure 2.1). Much like the well-known double helix of DNA, each channel of a given UIC crystal is composed of helical ribbons which run in opposite directions. Each UIC crystal contains either right-handed (space groups $P6_122$) or left-handed (space group $P6_522$) helical ribbons.

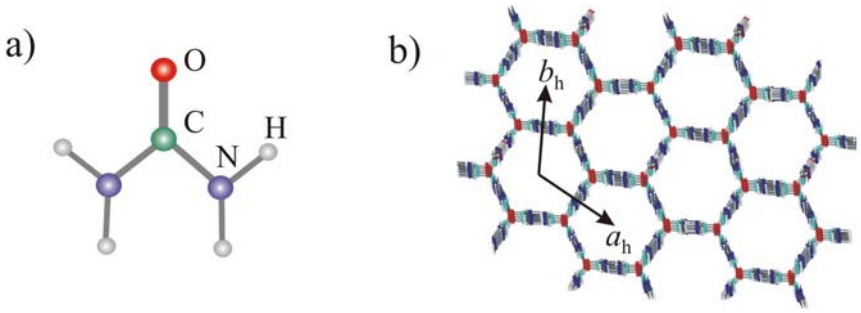

Figure 2.1 a) Molecule structure of urea; b) Schematic representation of the host structure of a conventional urea inclusion compounds viewed parallel to the channel axis (c_h) (note: $a_h = b_h \approx 8.22$ Å; $c_h \approx 11.02$ Å).

In UICs the urea substructure is hexagonal. However, in the absence of guest molecules, due to the poor packing efficiency of the empty host structure, the

hexagonal host collapses immediately to tetragonal urea [63-66]. The hexagonal urea substructure in UICs differs from the tetragonal structure of pure urea, but the two systems have related hydrogen bonding schemes, i.e. each oxygen is tethered to four hydrogens [63]. Thus all of the hydrogen bond donors and acceptors are matched in both structures. In hexagonal urea each *anti* hydrogen is bonded to a different carbonyl, whereas in tetragonal urea, the carbonyl oxygen is tethered to both of the *anti* hydrogens of an adjacent molecule. The distance between the nitrogen and oxygen atoms in the N–H···O hydrogen bonds are nearly identical in the hexagonal and tetragonal structures. The main difference, regarding molecular structure, lies in the C=O···H_a angle, which is close to 119° in hexagonal urea [67], but somewhat larger (149°) in tetragonal urea [68].

The hydrogen bonds of the urea molecules that form the channel walls give rise to the majority of the unique properties of UICs. The hydrogen bond donors and acceptors form a tightly woven, complementary network, which constructs the walls. Thus the included guest molecules can only contact the faces of the urea molecules. If the urea molecules turn toward the guest molecules, they have to either break or weaken hydrogen bonds with other urea molecules [67], which restricts the potential of hydrogen bonding between the host and guest. These strong host-host interactions, along with the relatively smooth features of the channel wall, give rise to a system in which the guest molecules are held only loosely, and undergo substantial torsions, librations and translations, as well as reorientations about the channel axis. Due to these structural features, urea inclusion compounds are frequently nonstoichiometric, with the guest molecules normally packing within van der Waals contact of each other. For most UICs, it is the dynamic disorder of the guest molecules about the channel axis that maintains the average hexagonal symmetry of the host structure [69].

In UICs the host-guest interaction is not specific, the suitability of a guest molecule

for UIC formation depends largely on its shape and size. The linear channels are one-dimensional, parallel, nonintersecting of infinite length, and have an inner diameter of *ca*. 5.25 Å [13, 70], which displays the discriminator for the guest molecules accommodated. Only linear, branched, or functionalized hydrocarbons with typical substituents such as methyl and ethyl groups or halogen atoms fit into the urea channels. The van der Waals envelope of the guest molecules is the determinative factor for the formation of a urea inclusion compound. If the guest is only moderately larger than the channel (e.g., benzene), complexation is usually quite difficult. In general (with certain exceptions [43, 71]), extremely short-chain guests typically do not form inclusion compounds with urea due to their higher volatility determined by their lower binding energy and smaller effective surface areas in contact with the urea host. UICs containing short-chain guests have a greater proportion of regions of low electron density between guest molecules in the channel, and the hexagonal host structure can not gain the necessary stabilization from its interaction with the included molecules. Once a critical length is reached, the complexation energy of the guest and the concomitant host stabilization are large enough to form stable inclusion compounds. Due to the special requirement on size and shape compatibility between the host and guest components, urea inclusion compounds can be used in applications based on molecular separation, such as the separation of linear and branched alkanes from mixtures or as a method for isolating linear molecules in synthetic organic chemistry.

For the preparation of urea inclusion compounds, there exist a number of problems (such as the inclusion of solvent, forming the extremely small crystals) associated with formation of high quality crystals for physical or chemical studies. The only solvent that will yield UICs reliably is methanol. By slowly evaporating the solvent or slowly cooling the methanol solution which contains urea and the guest, normally, hexagonal needles, prisms, or plates that range from micrometers to tens of millimetres in size can form well. If only microcrystalline samples are required, the

possible way is to simply grind the host and guest together in the presence of traces of methanol.

For conventional UICs, an important fundamental property is related to the periodicities, c_h and c_g, of the host and guest substructures along the tunnel axis. In classical terms, the UICs can be assigned as incommensurate if there are no sufficiently small integers m and n to suffice $mc_g \approx nc_h$ [72], and as commensurate if sufficiently small integers can be found to satisfy this equality. If the host and guest are truly incommensurate, as a consequence, each guest molecule within a given channel, in principle, has a slightly different host substructure environment. If the host and guest substructures are commensurate, the guest molecules are in a well-defined host environments, and the urea channel structure is substantially distorted, which reflects that specific host-guest interactions are established in these UICs [73-76].

In incommensurate UICs, it is found that the guest molecules generally exhibit sufficient positional ordering, if one focuses on the positional relationship between guest molecules in adjacent channels, to allow an average three-dimensional lattice to be defined, and measured [77, 78]. Host and guest molecules interact and each subsystem exerts an incommensurate modulation on the other. Hence, each subsystem can be regarded [67] as an incommensurately modulated basic structure, which can be described by using conventional crystallographic principles (e.g. three-dimensional space group symmetry). The basic structure itself is a hypothetical entity, which is used to represent the structure that the real substructure would relax to in the absence of host-guest interaction. Clearly, an incommensurate UIC can be considered in terms of an intergrowth of two incommensurately modulated substructures because the incommensurate modulation in one subsystem has the same periodicity as the basic structure of the other subsystem.

The mode of interchannel ordering of the guest molecules can be defined conveniently [79] in terms of two parameters, c_g and Δ_g, where Δ_g is the smallest

offset along the channel axis between the mass centers of two guest molecules in adjacent channels (see figure 2.2). The nature of the interchannel ordering of the guest molecules depends on the functional groups present in the guest molecule, with different families of guest molecule exhibiting different characteristic modes of interchannel ordering [77-80].

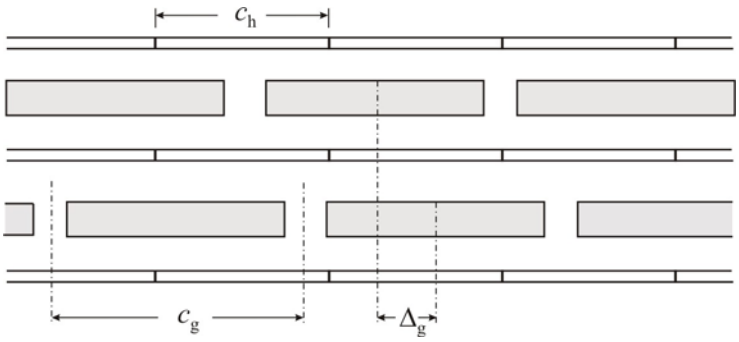

Figure 2.2 Schematic two-dimensional representation of a urea inclusion compound, viewed perpendicular to the channel axis, indicating the definitions of c_h, c_g, and Δ_g.

The concept of Δ_g can be extended to the third dimension, which provides a complete description of the three-dimensional packing arrangement of the guest molecules. In UICs, if the symmetry of the basic guest structure is lower than that of the basic host structure, a given single crystal usually comprises different domains of this guest substructure, which differ in their orientation with respect to the host structure [20, 77], but have the identical packing of guest molecules (see figure 2.3). The different domains are related by rotation about the channel axis. The host-guest interaction is of predominant importance, which controls well-defined interchannel ordering of the guests in the incommensurate UICs [81]. In certain cases, direct interaction between guest molecules in adjacent channels may also contribute to the three-dimensional ordering of the guest molecules. Such interactions are necessarily long-range (with a minimum distance of ca. 8.20 Å); for example, dipole-dipole interactions between guest molecules in different channels, involved in interchannel ordering schemes, can be evaluated [82].

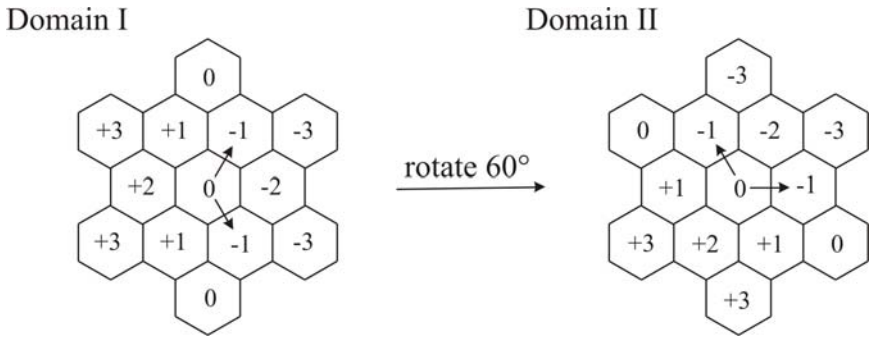

Figure 2.3 Molecular packing of guest molecules within the two domains of an incommensurate urea inclusion compound. Each channel is labelled as *r*, indicating that the relative *z*-coordinates (*z* denoted as channel axis) of the guest molecules in that channel are $r\Delta_g + sc_g$ (*s* = integer) [79].

Urea inclusion compounds possess an open host structure, which allows the migration of molecules into the channel structure of UICs [83]. Due to the fact that the guest molecules in urea channels are always loosely packed along the channel, the entry of external molecules into the channel should be associated with the concomitant loss of guest molecules from this structure via the other end of the channel. The occurrence of this exchange process indicates that the host framework in UICs, similar to zeolitic and other micro-porous inorganic host, can serve as a medium within which chemical or other transformations of guest species could be carried out with continuous removal of product molecules and insertion of fresh reactant molecules without requiring to destroy the host framework, e.g. by dissolution, in order to recover the product molecules.

For the majority of UICs, the phase transition was recorded by differential thermal analysis [23], differential scanning calorimetry [23, 84-89] and x-ray diffraction [90]. The phase transition is regarded as an order-disorder transition concerning the orientation of the guest molecules along with the deformation of the urea channels.

The ordinary hexagonal urea channels (high-temperature form) transform commonly into orthorhombic channels (low-temperature form) across the phase transition temperature, i.e. an orderly orientation of the guest molecules below the transition temperature results.

In the smooth and rigid urea channels, guest molecules are held loosely and undergo a variety of dynamical processes, such as rapid rotation around the long molecular axis ($k > 10^8\ s^{-1}$), fast torsional libration at the chain ends ($k > 10^{10}\ s^{-1}$), vibrations of mass center ($k > 10^{12}\ s^{-1}$), and rapid methyl-group rotation ($k > 10^{11}\ s^{-1}$). These motions are all much faster than, and uncorrelated with, the motion of the host (it is found that the host molecules experience 180° jumps about their C=O bonds at sufficiently high temperature [39-43]). At low temperatures, the loss of mobility of guests can lower the symmetry of the host and give rise to either first- or second-order phase transitions. Such phase transitions are chain-length dependent, and typically lead to orthorhombic structures below the transition temperature.

A wide range of techniques have been applied to investigate the dynamic properties of urea inclusion compounds [20-35]. Among these, ^2H NMR spectroscopy is an attractive technique and useful in the investigations of a diverse range of materials: surface immobilized systems [91], liquid crystals [47, 92-94], polymers [46] and lipid membranes [95-99]. The low natural abundance of the deuteron means that selective labelling is possible, and this facilitates the unambiguous determination of reorientation dynamics at specific molecular sites. In addition, the dominant spin interaction is the nuclear quadrupole coupling, described by a single-spin tensor Hamiltonian. Thus, the correlated, many-body phenomena do not need to be treated explicitly and the description of reorientation dynamics of individual sites is greatly simplified. Furthermore, the principal axis of the deuteron electric-field-gradient (EFG) tensor is aligned along the chemical bond direction, which allows a very direct manner to monitor the bond reorientation. In terms of the dynamic range, various ^2H NMR experimental techniques, such as line shape and spin-spin relaxation

experiments for molecular motion with rate constant of $10^3 \sim 10^8$ s^{-1}, spin-lattice measurements [100] for $10^8 \sim 10^{12}$ s^{-1}, have been utilized.

The ^{13}C NMR chemical shift values of n-alkanes, as well as substituted alkanes are also employed as a means of determining the structure and stereochemistry of these compounds [11, 25]. The crystal structural studies of urea inclusion compounds with n-alkane [36, 90] show that the conformations of the guest molecules are all-trans, in contrast to the conformations of a long-chain molecule in solution which exist in both gauche and trans forms. Therefore, detection of solid state ^{13}C high resolution NMR spectra of urea inclusion compounds of long-chain molecules, and comparison of the chemical shift values with those in solution NMR enables us to determine the conformation dependencies of chemical shifts of normal alkanes.

2.2 1,10-dibromodecane and 1,11-dibromoundecane/urea inclusion compounds

Single crystal X-ray diffraction [77] studies for the urea inclusion compounds containing $Br(CH_2)_nBr$ guests with n = 7-10 revealed at room temperature an average interchannel ordering of the guest molecules. The offset, Δ_g, between the guests in adjacent channels relates to the length of the guest molecules, c_g, by a factor of 1/3, i.e. $\Delta_g = c_g/3$ [77]. This suggests that the offset is controlled by interchannel guest-guest interactions, which are mediated by the intervening urea molecules. The basic guest structure is rhombohedral (probable space group *R*32) and there are two domains of the basic guest structure which are related by 60° rotation about the channel axis. Along the channel axis there is an incommensurate structural relationship [77, 101, 102] between the host and guest substructures in the $Br(CH_2)_nBr/[^2H_4]$ urea inclusion compounds with n = 7-11. As a result of this incommensurate relationship, principally, each guest molecule within a given channel has a different instantaneous environment, which means there is higher mobility in these urea inclusion compounds than in those with commensurate UICs in which specific host-guest interactions exist. Raman scattering investigations [9] have shown

that the alkane chains of these α,ω-dibromoalkane guest molecules are predominantly in the 'all-trans' conformation.

It is well known [5, 85, 90] that alkane/urea inclusion compounds undergo a phase transition from a low-temperature orthorhombic phase to a high-temperature hexagonal phase. This phase transition is also believed to be associated with an abrupt change in the dynamic properties of the alkane molecules, and it has been shown that these molecules undergo a fast motion in the high-temperature phase. With powder X-ray diffraction [23, 36-38], differential thermal analysis [23], differential scanning calorimeter [85], such phase transition associated with the distortion of the host channel structure has been found to occur between 140 K and 170 K for $Br(CH_2)_nBr$/urea inclusion compounds (n =7-11).

Measurements of incoherent quasielastic neutron scattering (IQNS) [27] in $Br(CH_2)_nBr$/urea inclusion compounds (with n = 8-10) have suggested diffuse oscillatory guest motion in the low temperature phase, and in the high-temperature hexagonal phase the dynamic properties of the guest molecules can be described in terms of translation and rotational diffusion in a onefold cosine potential. In this work, two guest molecules of 1,10-dibromodecane and 1,11-dibromoundecane in urea inclusion compounds are thoroughly investigated in a quantitative way.

2.3 1,6-dibromohexane/urea inclusion compounds

1,6-dibromohexane/urea does not experience similar solid-solid state phase transition below room temperature as found for its long-chain counterparts. Upon increase of temperature, the isomorphous monoclinic structure (space group $P2_1/n$), determined by X-ray diffraction at 100 K, gradually transforms towards hexagonal symmetry [55]. Moreover, the host and guest substructures of the 1,6-dibromohexane UIC are thought to be commensurate. The 1,6-dibromohexane guest molecules are therefore

fixed in well-defined positions within the urea substructure. As a result, the end-groups of the incorporated 1,6-dibromohexane guests are exclusively stabilized in a gauche conformational state even upon cooling down to 90 K [54, 55].

From ^{2}H NMR spectroscopy and the information from a complementary X-ray diffraction study [8, 55], the dynamic properties of 1,6-dibromohexane in urea have been described in terms of a non-degenerate mutual exchange between the two gauche conformational states (with unequal equilibrium population). A data analysis including relaxation times as well as relaxation time anisotropy performed in this work, provides reliable results for the aforementioned gauche-gauche exchange dynamics.

2.4 n-alkane with mono-substituent end functional group/urea inclusion compounds

If the terminal methyl groups are replaced by different substituents, then the end-groups of two adjacent guest molecules in urea may arrange in three different ways: head-head, head-tail, tail-tail. This issue has been investigated for a wide range of asymmetrical guest molecules in UICs [35, 57, 58, 103] by high resolution ^{13}C NMR spectroscopy. However, the carboxylic acids have been reported to form exclusively head-head dimers in the urea channels due to hydrogen bonding [35].

For stearic acid alkyl chains are assumed to be in an extended all-trans configuration along the urea channel axis. It is found from the analysis of ^{2}H NMR line shapes that the reorientation of overall chains occurs through discrete jumps of C_3 symmetry, which is compatible with the site symmetry of the host lattice [26, 104-108]. The combined effect of chain hopping and end-segment fluctuations results in a predominantly diffusive-type motion of the end methyl group [26]. The studies of deuteron relaxation times (Zeeman and quadrupole order) on perdeuterated octanoic

acid-d_{15}, dodecanoic acid-d_{23} and hexadecanoic acid-d_{31} in urea showed that the dynamics of the guest molecules could be explained in terms of rapid rotation about the long molecular axis and slower, limited angle libration of individual CD bonds about a perpendicular axis [4]. Bromooctane-d_2 labelled at the α position was found to reorient by means of the diffusion about an axis perpendicular to the C-D bond, in accordance with an extended all-trans chain conformation [26]. In this work, the molecular behaviours of n-alkane with 1-bromo, 1-fluoro, 1-carboxyl and α, ω-dicarboxyl groups in urea are studied by multiple-nuclear NMR spectroscopy.

2.5 Hexadecane and pentadecane/urea inclusion compounds

For alkane/urea inclusion compounds, the offset $\Delta_g = 0$ is independent of the values of c_g; c_g increases linearly with the number of CH_2 groups in the alkane molecule. Former calorimetric [85], X-ray [23, 36-38, 102], and spectroscopic [5, 16, 34, 109-111] studies indicate that UICs with n-alkanes experience a solid-solid phase transition. The corresponding transition temperature increases monotonically with the length of the alkane guest molecules and displays a characteristic odd-even effect as function of the number of methylene chain segments. X-ray investigations have shown that the high temperature phase –being stable at room temperature– is characterized by a hexagonal symmetry of the urea channels with stretched paraffin chains in an almost all-trans conformation [23, 36-38, 102].

From variable-temperature ^2H NMR investigations of the hexadecane/urea inclusion compounds [7], the dynamic properties of the guest molecules have been established. In the low temperature phase the whole chains undergo fast but restricted rotational motions (rate constant ca. 10^7 s^{-1}). In addition, intramolecular trans-gauche isomerizations and methyl group rotation contribute to the spin relaxation of the alkane chain ends. In the high temperature phase the alkyl chains rotate rapidly (rate constant ca. 10^{10} s^{-1}) and almost unrestricted around the channel long axis.

Spin-lattice relaxation time in the rotating frame, $T_{1\rho}$ (^{13}C), provides a way to investigate the slower motions in the low to mid-kilohertz frequency range [112, 113]. On the other hand, $T_{1\rho}$ (^{1}H) provides information about spatially sensitive proton spin diffusion, which can be utilized to query the phase-separated or homogenous character of a sample [112, 114, 115], because the rate of magnetization transfer via proton spin diffusion is on the right time scale to measure phase separation over the length scale of 5-200 Å. In this work, for the first time, n-alkane/urea inclusion compounds are studied by spin-lattice relaxation time in rotating frame.

Chapter 3 Solid state NMR spectroscopy

3.1 General description of NMR experimental techniques

The theoretical description of the solid state NMR technique starts with the treatment of the density matrix operator, followed by general expressions for the spin Hamiltonian. For the spin I = 1 and 1/2 systems, the corresponding terms are explained separately. The state of the spin system is described by the density matrix operator, $\hat{\rho}(t)$, while the forces or interactions that change the state of the system are represented by the Hamiltonian.

The description of NMR experiments in general is done by considering the time evolution of the density matrix operator, $\hat{\rho}(t)$. In the absence of molecular motions the time evolution of the density matrix operator $\hat{\rho}(t)$ is described by the Liouville-von Neumann equation [116, 117]

$$\frac{d\hat{\rho}(t)}{dt} = \frac{i}{\hbar}[\hat{\rho}(t), \hat{H}] \tag{3.1}$$

where $\hat{H}$ is the time independent Hamiltonian, which contains all magnetic interactions of the nuclei. A formal solution exists for Eq. (3.1), namely

$$\hat{\rho}(t) = \hat{U}(t) \cdot \hat{\rho}(0) \cdot \hat{U}(t)^{-1} \tag{3.2}$$

where the propagator $\hat{U}(t)$ is defined as

$$\hat{U}(t) = e^{-(i/\hbar)\hat{H} \cdot t} \tag{3.3}$$

The NMR experiment is furthermore subdivided in time intervals $\tau_1, \tau_2, ..., \tau_n$ that possess a constant Hamiltonian, e.g., with and without radio frequency (r.f.) pulses and/or particular magnetic interactions. By summing the intervals with constant Hamiltonian, the density matrix operator $\hat{\rho}(t)$ at a particular time t can be easily

calculated as

$$\hat{\rho}(t) = \hat{\rho}\left(\sum \tau_i\right) \tag{3.4}$$

In the presence of molecular motions, the Stochastic Liouville equation can be used to describe $\hat{\rho}(t)$, which in general is written as [117, 118]

$$\frac{d\hat{\rho}(t)}{dt} = \frac{i}{\hbar}\left[\hat{\rho}(t), \hat{H}\right] + \left(\frac{\partial \rho}{\partial t}\right)_{dynamics} \tag{3.5}$$

Here, the second term on the right hand side accounts for the contribution due to dynamic processes, such as molecular motion or chemical exchange. By writing Eq. (3.5) in the form

$$\frac{d\hat{\rho}(t)}{dt} = \frac{i}{\hbar}\hat{L}\cdot\hat{\rho}(t) \tag{3.6}$$

$\hat{\rho}(t)$ is given by [119]

$$\hat{\rho}(t) = \hat{\rho}(0)\,\mathrm{e}^{(i/\hbar)\hat{L}\cdot t} \tag{3.7}$$

As before, the time evolution of the density matrix operator can be described by dividing the experiment in intervals with constant Hamiltonian, as expressed by Eq. (3.4). The Liouville super-operator $\hat{L}$ in Eqs. (3.6) and (3.7) is derived from the Hamiltonian by [120]

$$\hat{L} = H \otimes E - E \otimes H - i\hbar\frac{\partial}{\partial t} \tag{3.8}$$

where, E is the identity operator in Hilbert space. The final dimension of $\hat{L}$ is given to $n^2 \cdot N$, with N being the number of exchanging sites and n being the dimension of Hilbert space [119, 121].

3.2 Spin Hamiltonian and NMR spectra

The nuclei with a spin possess a magnetic moment $\vec{\mu}$, which interacts with its surroundings. Generally, these interactions can be divided into two classes which can be described by an external and an internal Hamiltonian [122-124], i.e.

$$\hat{H} = \hat{H}_{ext} + \hat{H}_{int} \tag{3.9}$$

The first term on the right hand side includes the interactions of a spin system with the external static magnetic field $\vec{B}_0$ (Zeeman interaction, $\hat{H}_Z$) and the pulsed oscillating radio-frequency (r.f.) fields ($\hat{H}_{rf}$); the second term includes the interactions of a spin system with internal local fields originating from the chemical shift interaction ($\hat{H}_{CS}$), direct dipole-dipole interaction (hetero-nuclear, $\hat{H}_{II}$, and homo-nuclear, $\hat{H}_{IS}$), quadrupole interaction ($\hat{H}_Q$), and indirect J-coupling ($\hat{H}_J$). Thus, Eq. (3.9) can also be expressed as [114, 120, 122]

$$\hat{H} = \hat{H}_Z + \hat{H}_{rf} + \hat{H}_{CS} + \hat{H}_{II} + \hat{H}_{IS} + \hat{H}_Q + \hat{H}_J \tag{3.10}$$

All internal Hamiltonian contributions reflect tensoral interactions, which depend on the orientation of the interaction tensor with respect to the external magnetic field direction. The external interactions have an identical influence on the whole spin system and contain no structural and dynamic information about the nucleus of interest; the structural and dynamic information is included in the internal interactions. In comparison with the external static field, the internal or local interactions are small. So they act only as a first-order perturbation in the high field (secular) limit and produce small shifts and splittings of the Zeeman energy levels which depend on the nature and extent of the couplings and on the number of interacting spins.

3.2.1 The Zeeman interaction

A nucleus with a spin also possesses a magnetic moment, $\vec{\mu}$, written as

$$\vec{\mu} = \gamma\hbar\hat{\vec{I}} \tag{3.11}$$

where γ (with unit of rad T^{-1} s^{-1}) is the gyromagnetic ratio of the nuclear spin $\hat{\vec{I}}$, $\hbar$ is the Planck's constant *h* divided by 2π.

When a nucleus is exposed to an external magnetic field, the interaction between the spin and the static magnetic field is described by the Hamiltonian

$$\hat{\mathrm{H}}_Z = -\gamma\hbar\vec{B}_0 \cdot \hat{\vec{I}} \tag{3.12}$$

where $\hat{\vec{I}} = (\hat{I}_x, \hat{I}_y, \hat{I}_z)$. Taking the field $\vec{B}_0$ along the z-direction of the laboratory frame, i.e. $\vec{B}_0 = (0, 0, B_0)$, the Zeeman Hamiltonian operator can then be written as

$$\hat{\mathrm{H}}_Z = -\gamma\hbar B_0 \hat{I}_z \tag{3.13}$$

The eigenstates of this Hamiltonian are the states $|\mathrm{I}, \mathrm{M}\rangle$, with *I* being the spin quantum number of the nucleus and *M* the magnetic quantum number that takes one of the values *I*, *I*–1, …, –*I*. The energy of the spin system can be calculated by applying the Zeeman Hamiltonian to the spin wave function $|\mathrm{I}, \mathrm{M}\rangle$

$$\hat{\mathrm{H}}_Z \,|\, I,\, M\rangle = -\gamma\hbar B_0 \hat{I}_z \,|\, I,\, M\rangle = -\gamma\hbar B_0 M \,|\, I,\, M\rangle \tag{3.14}$$

The resulting (2*I* + 1) equally-spaced energy levels are separated by the Larmor frequency ω_0 times $\hbar$. Provided the Zeeman interaction is the only contribution in the spin Hamiltonian, the magnetic moment of the nucleus experiences a precession around the direction of the magnetic field with the well-known Larmor frequency ω_0, which is given by

$$\omega_0 = -\gamma B_0 \tag{3.15}$$

For an allowed transition between two states, m and m' ($m' = m \pm 1$), the energy difference is given

$$\Delta E = \pm \gamma \hbar B_0 \tag{3.16}$$

From Eq. (3.16) it is found that the energy difference ΔE is directly proportional to the magnitude of the magnetic field. The energy difference between the two states alters along with the variation of the external magnetic field strength. Once the energy of the photon generated by the radio-frequency irradiation matches the energy difference between the two spin states, absorption of energy by the sample occurs.

When a group of spins is exposed to a magnetic field, the number of spins in the lower energy level, N^+ and the number in the upper energy level, N^- follow the Boltzmann statistics, as given by

$$\frac{N^-}{N^+} = e^{-\Delta E / kT} \tag{3.17}$$

k is Boltzmann's constant, 1.3805x10^{-23} J/Kelvin, and T is the temperature in Kelvin.

At room temperature, $N^-/N^+ = 0.99998$, the population difference between the two states is very small. The ratio N^-/N^+ decreases with decreasing temperature.

The signal in NMR spectroscopy results from the difference between the energy absorbed by the spins which make a transition from the lower energy state to the higher energy state, and the energy emitted by the spins which simultaneously make a transition from the higher energy state to the lower energy state. The signal is thus proportional to the population difference between the states, as described by Eq. (3.17).

3.2.2 Interaction with the radio-frequency fields

In NMR experiments, the r.f. field is created by the probe coil passing an alternating current at the Larmor frequency, and employed to manipulate the effective Hamiltonian of the spin system. The amplitude of the oscillating r.f. field is substantially smaller than that of the static magnetic field, so $\hat{\mathrm{H}}_{rf}$ acts as a perturbation on the spin system, which does not change the energy levels but only induces transitions between them. If an oscillating r.f. magnetic field, $\vec{B}_1 = (B_1, 0, 0)$, is applied along the x-axis perpendicular to the static magnetic field in the laboratory frame, the interaction of a nuclear spin with this field can be expressed by the Hamiltonian

$$\hat{\mathrm{H}}_{rf} = -2\gamma\hbar\vec{B}_1 \cos(\omega t + \varphi)\hat{\vec{I}} = -2\gamma\hbar B_1 \cos(\omega t + \varphi)\hat{I}_x \tag{3.18}$$

where ω is the carrier frequency and φ is a phase. When the r.f. field oscillates close to the resonance frequency ω_0, which corresponds to the Zeeman energy splitting, the transition between the spin states will occur.

The introduction of the r.f. pulse complicates the motion of the spin in the magnetic field. On one hand, the spin precesses around the B_0 field with the Larmor frequency, while on the other hand, it nutates due to the action of the r.f. field. In order to facilitate the interpretations, it is useful to introduce the "rotating frame", which rotates with frequency ω around the z-axis of the applied static magnetic field. In this rotating frame, the r.f. Hamiltonian is time-independent. At the same time, transformation into the rotating frame introduces a fictitious magnetic field $\vec{B}_f$, giving

$$\vec{B}_f = -\omega / \gamma \tag{3.19}$$

which is opposite to the direction of the static magnetic field $\vec{B}_0$. The effective

Hamiltonian in the rotating frame becomes

$$\hat{\mathrm{H}}_{eff} = -\gamma\hbar(\vec{B}_0 - \vec{B}_f)\hat{I}_z + \gamma\hbar\vec{B}_1\hat{I}_x = (\omega_0 - \omega)\hbar\hat{I}_z - \omega_1\hbar\hat{I}_x \tag{3.20}$$

where $(\omega_0 - \omega)$ is the so-called resonance offset. When $\omega_0 = \omega$, the irradiation is said to be the on-resonance.

An on-resonance pulse of θ_φ ($\varphi = \pm x, \pm y$) with different phase φ can be obtained by adjusting the duration of the irradiation of the pulse, t_{pulse}, to satisfy the following condition

$$\theta = \gamma B_1 t_{pulse} = \omega_1 t_{pulse} \tag{3.21}$$

For instance, a $90°_x$ pulse applied along the x axis in the rotating frame rotates the magnetization vector by 90° from the +z direction into the –y axis in terms of a right-handed rotation.

3.2.3 The quadrupole interaction

For nuclei with spin $I = \frac{1}{2}$, the nuclear charge distribution is spherical, on which the electric field gradient (EFG) produced by surrounding charges (electrons and neighbouring nuclei) within the molecules does not have effects. However, the nuclei with spin $I \geq 1$ possess an electric quadrupole moment, which arises from a spheroidal distribution of charges. The energy of the spheroidal charges depends on their orientation in molecular field gradient. When the electric field gradient $\tilde{V}$ satisfies the Laplace equation, an interaction between a quadrupolar nuclear charge and the electric field gradient takes place.

Deuterium is a nucleus with nuclear spin $I = 1$, i.e. a quadrupolar nucleus. In the

presence of a strong magnetic field, the nuclear spin of deuterium undergoes a splitting of three quantized energy levels due to the Zeeman effect. The strong interaction between the nuclear quadrupole moment and the electric field gradient leads to a perturbation of the Zeeman splittings. The magnitude of this perturbation is so large that the other nuclear spin interactions, such as dipole-dipole interaction, J-coupling and chemical shift anisotropy, can be neglected. Therefore, in ^{2}H NMR experiments, besides the Zeeman interaction, the nuclear quadrupole coupling described by a single-spin tensor Hamiltonian dominates the spectra [113, 125].

The electric field gradient $\tilde{\mathrm{V}}$ at the nucleus is described by a second rank tensor with elements, $V_{xx} = \frac{\partial^2 V}{\partial x^2}$, $V_{xy} = \frac{\partial^2 V}{\partial x \partial y}$, etc., where V is the electric potential. The electric field gradient tensor is symmetric, i.e. $V_{xy} = V_{yx}$ and so on, and traceless, i.e. $V_{xx} + V_{yy} + V_{zz} = 0$ (the Laplace equation). The tensor components specify the orientation and the magnitude of the electric field gradient. The orientation of the tensor defined in a coordinate frame attached to the molecule can often be inferred from the symmetry of the site, on which the nucleus sits.

In the principal axis system (PAS) the tensor is diagonal with the elements V_{XX}, V_{YY} and V_{ZZ}. The z-axis of the PAS is parallel to the C–^{2}H bond direction. Since $\tilde{\mathrm{V}}$ is traceless, only two parameters are needed to describe the three diagonal components, which are given by [116]

$$eq = V_{ZZ} = \frac{\partial^2 V}{\partial z^2} \tag{3.22}$$

$$\eta = \frac{V_{XX} - V_{YY}}{V_{ZZ}} \qquad 0 < \eta < 1 \tag{3.23}$$

where eq is the field gradient and η is the asymmetry parameter.

For a single spin with $I \geq 1$ the quadrupolar Hamiltonian is given by

$$\hat{\mathrm{H}}_Q = \hat{\vec{\mathrm{I}}} \cdot \tilde{\mathrm{Q}} \cdot \hat{\vec{\mathrm{I}}} \tag{3.24}$$

where $\tilde{\mathrm{Q}}$ is the quadrupolar coupling tensor, which is related to the electric field gradient by [122]

$$\tilde{\mathrm{Q}} = \frac{eQ}{2I(2I-1)\hbar} \tilde{\mathrm{V}} \tag{3.25}$$

Here, Q is the scalar quadrupolar moment of the nucleus (for deuterium, Q = 2.875 × 10^{-31} m^2), e is the elementary charge. Since the raising and lowering spin operators provide appropriate selection rules, it is useful to express Eq. (3.24) in terms of $\hat{I}_+$, $\hat{I}_-$, and $\hat{I}_z$, with the following abbreviations [116]

$$\begin{aligned} V_0 &= V_{zz} \\ V_{\pm 1} &= V_{zy} \pm iV_{zx} \\ V_{\pm 2} &= \tfrac{1}{2}\left(V_{xx} - V_{yy}\right) \pm iV_{xy} \\ \hat{I}_\pm &= \hat{I}_x \pm i\hat{I}_y \end{aligned} \tag{3.26}$$

The double subscripts, such as *xx* and *xy*, indicate second order derivatives of the electrostatic potential V with respect to the x, y, z coordinate axes. Hence, in the Cartesian coordinates for an arbitrary choice of the axis direction, the quadrupolar Hamiltonian can be rewritten as [50, 116, 124]

$$\begin{aligned} \hat{\mathrm{H}}_Q = \frac{eQ}{4I(2I-1)} \Big[& V_0 \left(3\hat{I}_z^2 - \hat{\vec{\mathrm{I}}}^2 \right) + V_{+1} \left(\hat{I}_- \hat{I}_z + \hat{I}_z \hat{I}_- \right) \\ & + V_{-1} \left(\hat{I}_+ \hat{I}_z + \hat{I}_z \hat{I}_+ \right) + V_{+2} \left(\hat{I}_- \right)^2 + V_{-2} \left(\hat{I}_+ \right)^2 \Big] \end{aligned} \tag{3.27}$$

The transformation from one coordinate frame to another is more conveniently realized if the Hamiltonian is expressed as a scalar product of two irreducible tensors, the spherical tensor ($\tilde{\mathrm{T}}_{lm}$) and the electric field gradient tensor ($\tilde{\mathrm{V}}_{l-m}$), in the spherical coordinates [122]

$$\hat{\mathrm{H}}_Q = C_Q \sum_{l=0}^{2} \sum_{m=-l}^{l} (-1)^m \tilde{\mathrm{T}}_{lm} \cdot \tilde{\mathrm{V}}_{l-m} \tag{3.28}$$

with $C_Q = \dfrac{eQ}{2I(2I-1)\hbar}$.

Since $\tilde{\mathrm{V}}_{l-m}$ is a symmetric and traceless second rank tensor, the elements with $l = 1$ are zero, and if it is in its principle axis system, only the components with $m = 0, \pm 2$ are nonzero. On the other hand, $\tilde{\mathrm{T}}_{lm}$ has only the contribution for $l = 2$, because the scalar product with the electric field gradient is zero for quadrupolar interaction with $l = 0, 1$. Then, the Cartesian components are related to both tensor elements ($\tilde{\mathrm{V}}_{l-m}$ and $\tilde{\mathrm{T}}_{lm}$) according to the following equations [50, 116, 126]

$$V_{00}^{PAS} = \tfrac{1}{3} Tr(V) = \tfrac{1}{3}\left(V_{xx} + V_{yy} + V_{zz}\right) = V_{iso} \tag{3.29}$$

$$V_{20}^{PAS} = V_{zz} = \sqrt{\tfrac{3}{2}} eq \tag{3.30}$$

$$V_{2\pm1}^{PAS} = 0 \tag{3.31}$$

$$V_{2\pm2}^{PAS} = \tfrac{1}{\sqrt{6}}\left(V_{xx} - V_{yy} \pm 2iV_{xy}\right) = \tfrac{1}{2} eq\eta \tag{3.32}$$

$$T_{20}^{LAB} = \tfrac{1}{\sqrt{6}}\left[3\hat{I}_z^2 - \hat{\vec{\mathrm{I}}}^2\right] \tag{3.33}$$

$$T_{2\pm1}^{LAB} = \mp\tfrac{1}{2}\left[\hat{I}_z\hat{I}_\pm + \hat{I}_\pm\hat{I}_z\right] \tag{3.34}$$

$$T_{2\pm2}^{LAB} = \tfrac{1}{2}\hat{\vec{\mathrm{I}}}_\pm^2 \tag{3.35}$$

The tensor elements of $\tilde{\mathrm{T}}_{2m}$ are expressed in the LAB frame, which is defined by aligning the external magnetic field along the z-axis. For the sake of consistence, all elements in Eq. (3.28) have to be referred to the same coordinate system. Therefore with the Wigner rotation matrix $\mathrm{D}^{(2)}_{m'm}(\Omega)$, the $\tilde{\mathrm{V}}_{2-m}$ elements are transformed to the LAB frame [127]

$$V_{2m}^{LAB} = \sum_{m'=-2}^{2} V_{2m'}^{PAS} \mathrm{D}_{m'm}^{(2)}(\Omega) \tag{3.36}$$

Here, Ω represents the Euler angles involved in the transformation. Thus $\hat{\mathrm{H}}_Q$ can be written as

$$\hat{\mathrm{H}}_Q = C_Q \sum_{m=-2}^{2} (-1)^m T_{2m} \sum_{m'=-2}^{2} V_{2m'}^{PAS} \mathrm{D}_{m'm}^{(2)}(\Omega) \tag{3.37}$$

Since the interaction of the nuclear spin with the static magnetic field are much larger than the quadrupolar interaction, according to a first order approximation in the perturbation theory, only the components commuting with the Zeeman interaction are important ($[\hat{\mathrm{H}}_Z, \hat{\mathrm{H}}_Q] = 0$). This scalar contribution contains only terms with m = 0. Therefore the quadrupolar Hamiltonian can be further simplified. By inserting the Wigner matrix elements, the Hamiltonian is finally given by [114]

$$\hat{\mathrm{H}}_Q = \frac{e^2 qQ}{8I(2I-1)\hbar}\left[3\hat{I}_z^2 - I(I+1)\right]\left[3\cos^2\theta - 1 + \eta\sin^2\theta\cos 2\phi\right] \tag{3.38}$$

When the selection rules are applied to the quadrupolar Hamiltonian, the angular dependent resonance frequencies ω_Q, i.e. the frequency transition between two energy levels, are obtained as [126]

$$\omega_Q = \pm\frac{3}{8}\left(\frac{e^2 qQ}{\hbar}\right)\left(3\cos^2\theta - 1 + \eta\sin^2\theta\cos 2\phi\right) \tag{3.39}$$

Here, $e^2qQ/\hbar$ is the quadrupolar coupling constant, δ_{QCC}, and is related to the overall width of the polycrystalline spectrum. The polar angles θ and ϕ specify the relative orientation of the magnetic field B_0 and the electric field gradient in the PAS.

In ^{2}H NMR spectroscopy, the energy of a deuterium nucleus in a magnetic field is given by the magnetic energy E_M and the quadrupole energy E_Q. The total Hamiltonian can be written as [50, 126]

$$\hat{H} = \hat{H}_Z + \hat{H}_Q \tag{3.40}$$

As illustrated in Fig. 3.1, there are $(2I + 1) = 3$ energy levels, associated with $m = 1, 0, -1$ and two allowed transitions given by selection rule $\Delta_m = \pm 1$. The perturbation of the quadrupolar interaction re-establishes two transitions between the Zeeman energy levels. The frequencies of the resulting two transitions can be expressed as

$$\omega = \omega_0 \pm \omega_Q \tag{3.41}$$

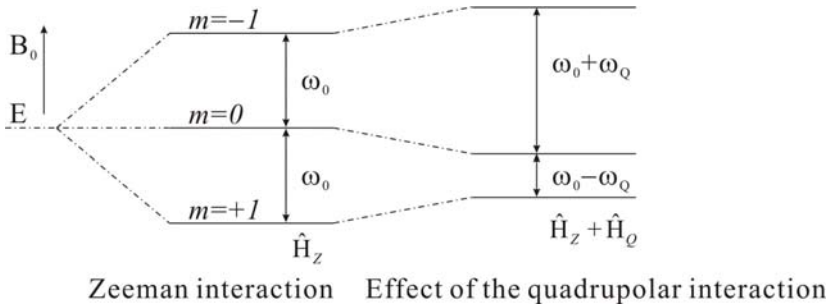

Figure 3.1 Energy level diagram for a spin $I = 1$.

For aliphatic C–D bonds, Eq. (3.39) can be further simplified, since the electric field gradient tensor is axially symmetric and parallel to the C–D bond axis, the asymmetry parameter is usually zero. Thus the NMR frequencies of the two transitions can be written as

$$\omega = \omega_0 \pm \frac{3}{8}\left(\frac{e^2 qQ}{\hbar}\right)\left(3\cos^2\theta - 1\right) \tag{3.42}$$

From Eq. (3.42), it can be found that the transition frequencies of the NMR lines depend on the angle θ between the C–D bond and the external magnetic field. If a single crystal or an oriented system is rotated in the magnetic field, each orientation of different resonance can be obtained by observing the doublet splitting as a function of angle. With this information the orientation of a specific group (i.e. the C–D bond) can be determined.

^{2}H NMR line shapes of static samples. ^{2}H NMR spectroscopy is employed to study polycrystalline materials and the observed powder line shape, the so-called "Pake pattern", is the superposition of all (static) orientations of the crystallites with respect to the external magnetic field [114]. The line shape can be calculated by taking into account of the probabilities of the various C–D bond orientations with respect to the external magnetic field. Following an excitation of a 90° pulse, the NMR signal of a polycrystalline sample in the time domain is given by

$$S(\theta,\phi,t) = N\int_0^{\pi} \sin\theta d\theta \int_0^{2\pi} e^{-i\omega_Q(\theta,\phi)t} d\phi \tag{3.43}$$

where N is a normalization constant and $\omega_Q(\theta,\phi)$ can be obtained from Eq. (3.39). The ^{2}H NMR spectrum in the frequency domain is given after a Fourier transformation (FT) of this signal

$$S(\theta,\phi,\omega) = \int_0^{\infty} S(\theta,\phi,t) e^{i\omega t} dt \tag{3.44}$$

For $\eta = 0$ (i.e. the cases with axial symmetry of the EFG tensor), the calculation of the powder spectrum is simple due to the vanishing angle ϕ in Eq. (3.42)). When each θ interval is transformed into the spectrum, the integral intensities of the corresponding intervals in θ and ω are equal. In the Pake pattern, the outer ends of the shoulders correspond to the case when the C–D bond is oriented parallel ($\theta = 0°$) to the static magnetic field, while the inner singularities arises from the orientation of the C–D bond perpendicular ($\theta = 90°$) to the external magnetic field (shown in Fig. 3.2). The whole spectrum represents the superposition of two axially symmetric distributions which only depend on the angle θ and can be distinguished only on the basis of algebraic signs. These two components intersect at 54.7° which is the so-called magic angle (see Fig. 3.2). The distance between the singularities is given by [37]

$$\Delta\omega_Q = \frac{3}{4}\frac{e^2qQ}{\hbar} = \frac{3}{4}\delta_{QCC} \tag{3.45}$$

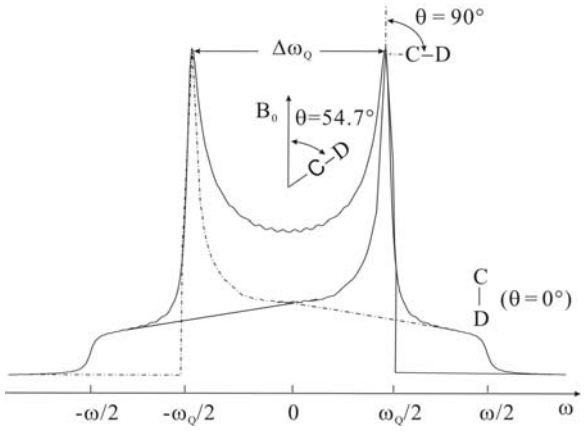

Figure 3.2 Dependency of the ^{2}H NMR powder spectrum on the relative orientation of a C-D bond with respect to the external magnetic field ($\eta = 0$).

When $\eta \neq 0$, the powder spectrum becomes more complicated. The ^{2}H NMR powder spectrum of static samples directly reflects the three main components of the quadrupolar interaction tensor ($\tilde{Q}^{PAS}$) in its principal axis system (see Fig. 3.3) [51, 128, 129], while for $\eta = 0$, Q_{XX} and Q_{YY} become equal.

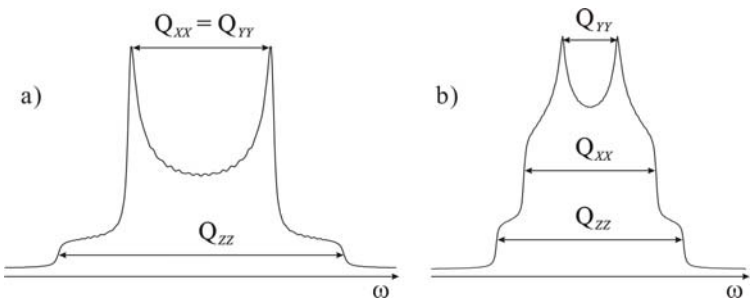

Figure 3.3 Pake pattern of a polycrystalline solid sample with (a) $\eta = 0$ and (b) $\eta \neq 0$ showing the dependency of the ^{2}H NMR frequency on the relative orientation of a C-D bond.

3.2.4 The chemical-shift interaction

The chemical shift, or shielding, interaction originates from the effect of B_0 on the electrons around a nucleus. When the electrons with the magnetic moments precess about the external magnetic field, additional small magnetic fields are induced, which may add to or subtract from the external magnetic field felt by the nucleus. Therefore, the effective magnetic field experienced by the nucleus is altered, so is its resonance frequency. The chemical shift interaction is an anisotropic interaction, which originates from the fact that the electronic distribution in the molecules can be thought of as an ellipsoid. The degree to which the electron density affects the resonance frequency of a nucleus depends on the orientation of the electron cloud (and hence the orientation of the molecule) with respect to B_0.

The chemical shift Hamiltonian can be treated as a perturbation with respect to $\hat{H}_0 = \omega_0 \hat{I}_z$. Based on $\hat{I}_z$ eigenfunctions, $E_m^{(1)} = \left\langle m \middle| \hat{H}_1 \middle| m \right\rangle$, the diagonal elements of the perturbing Hamiltonian reflect the energy shifts, thus only diagonal components in $\left| m \right\rangle$ of the local field operators need to be retained and the secular parts of the Hamiltonian commute with $\hat{I}_z$ operator. Therefore only terms containing $\hat{I}_z$, $\hat{\vec{\mathrm{I}}}_i \cdot \hat{\vec{\mathrm{I}}}_j$ and their products remain after a truncation of the local field Hamiltonian. For a single spin, in the LAB frame the secular part of chemical shift Hamiltonian has the form [114]

$$\hat{\mathrm{H}}_{cs} = -\gamma \mathrm{h} B_0 \sigma_{zz}^{LAB} \hat{I}_z \tag{3.46}$$

By using the Wigner rotation matrix, σ_{zz}^{LAB} is transformed into the principle axis system (PAS) tensor σ^{PAS}. σ^{PAS} tensor is diagonal and has three main components: σ_{xx}^{PAS}, σ_{yy}^{PAS} and σ_{zz}^{PAS} (see Fig. 3.4). The chemical shift Hamiltonian is expressed by [114]

$$\hat{\mathrm{H}}_{cs} = \left\{ \sigma_{iso} + \tfrac{1}{2}\delta_{cs}\left[3\cos^2\theta - 1 + \eta_{cs}\sin^2\theta\cos(2\phi) \right] \right\} \mathrm{h}\gamma B_0 \hat{I}_z \tag{3.47}$$

Here the angles θ and ϕ describe the orientation of the chemical shift tensor with respect to B_0. σ_{iso} is the (isotropic) chemical shift (typically in the order of 10^{-6} in ppm) and written as

$$\sigma_{iso} = \tfrac{1}{3}\left(\sigma_{xx}^{PAS} + \sigma_{yy}^{PAS} + \sigma_{zz}^{PAS} \right) \tag{3.48}$$

The traceless components can be derived from subtracting the isotropic chemical shift from each principal value of σ^{PAS}

$$\begin{aligned} \sigma_x &= \sigma_{xx}^{PAS} - \sigma_{iso} \\ \sigma_y &= \sigma_{yy}^{PAS} - \sigma_{iso} \\ \sigma_z &= \sigma_{zz}^{PAS} - \sigma_{iso} \end{aligned} \tag{3.49}$$

Thus the shielding asymmetry parameter, η_{cs}, the shielding anisotropy, $\Delta\sigma$, and the parameter of the chemical shift anisotropy (CSA), δ_{cs}, can be defined as

$$\begin{aligned} \eta_{cs} &= \frac{\sigma_x - \sigma_y}{\sigma_z} \\ \Delta\sigma &= \sigma_z - \tfrac{1}{2}\left(\sigma_x + \sigma_y \right) \\ \delta_{cs} &= \sigma_z \end{aligned} \tag{3.50}$$

When the $\tilde{\sigma}$ tensor is axially symmetric with respect to the principal z-axis, the asymmetry parameter vanishes ($\eta_{cs} = 0$) and $\sigma_x = \sigma_y$, and the shielding anisotropy can be further simplified.

In terms of η_{cs}, and δ_{cs}, the chemical shift resonance frequency can be written as

$$\omega_{cs}(\theta,\phi) = \tfrac{1}{2}\delta_{cs}\left[3\cos^2\theta - 1 + \eta_{cs}\sin^2\theta\cos(2\phi) \right] \tag{3.51}$$

For a polycrystalline sample, all possible orientations of the principle axis with respect to the external magnetic field are sampled resulting in a typical powder pattern. Figure 3.4a depicts the theoretical line shape of an axially symmetric chemical shift tensor ($\eta_{cs} = 0$). The more general case with $\eta_{cs} \neq 0$ is depicted in Fig. 3.4b.

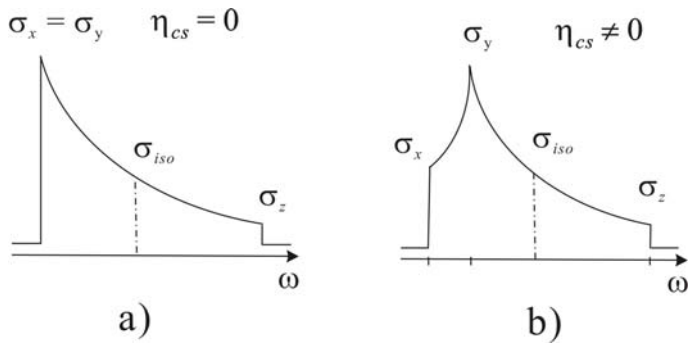

Figure 3.4 Schematic representation of theoretical powder line shapes for a) axially symmetric; b) general chemical shift tensors. The dash line denotes the isotropic chemical shift values σ_{iso}.

Molecular motion will narrow the chemical shift tensor, by partial averaging, and the resulting powder pattern will contain motional and orientation information of the molecules. In a solution, the rapid, essentially isotropic motion of the molecule or molecular segments averages the shielding tensor to its isotropic value σ_{iso}.

Since the chemical shift is a direct consequence of the electronic structure, the chemical shift tensor can give information on the structure of the molecules and serve to verify calculations of the electronic structure of molecules. The chemical shift tensor powder pattern contributes significantly to the line broadening of a solid state NMR spectrum, which often obscures the structural information available from the isotropic chemical shifts. This line broadening of the resonances in the solid state can be eliminated by high speed sample spinning at the magic angle (see later section). Thus, the magic angle spinning (MAS) reduces the anisotropic chemical shift to its isotropic average.

3.2.5 The direct dipole-dipole interaction

A single nucleus with spin I = 1/2 is placed in the external magnetic field, based on its orientation, either parallel ("spin-up") or antiparallel ("spin-down") with respect to the external field. If two dipolar coupled spins *i* and *j* are considered, one nuclear spin will experience a magnetic field produced by the other and vice versa when the two spins are within reasonable proximity of each other (< 10 Å). This magnetic field produced by spin *j* will either add to ("spin-up") or subtract from ("spin-down") the external field felt by the spin *i*, thus the effective magnetic field at the site *i* changes its resonance frequency. The magnitude of this dipolar-dipolar interaction depends on the distance between the two spins and the direction of the internuclear vector with respect to the external magnetic field (see Fig. 3.5).

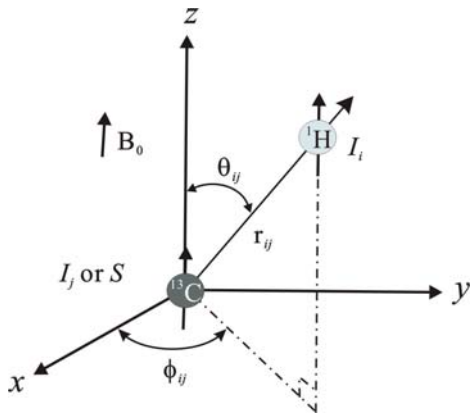

Figure 3.5 Schematic representation of a coupled spin pair in a magnetic field B_0.

There are two distinguishable cases: homonuclear dipolar coupling between the same types of nuclei and heteronuclear coupling between different types of nuclei. (By convention, nuclear spins are labelled as *I* for "abundant" spins, for example, that of ^{1}H or ^{19}F, and *S* for "rare" spins such as that of ^{13}C or ^{15}N nuclei.). The dipolar-dipolar Hamiltonian between the two homonuclear spins *i* and *j* can be expressed as

$$\hat{H}_{D,II} = \hat{\vec{I}}_i \cdot \tilde{D}_{II} \cdot \hat{\vec{I}}_j = \frac{\hbar \gamma_i \gamma_j}{r_{ij}^{-3}} \left(\hat{\vec{I}}_i \cdot \hat{\vec{I}}_j - \frac{3\left(\hat{\vec{I}}_i \cdot \hat{\vec{r}}_{ij}\right)\left(\hat{\vec{I}}_j \cdot \hat{\vec{r}}_{ij}\right)}{r_{ij}^2} \right) \tag{3.52}$$

or between heteronuclear *I* and *S* spins as

$$\hat{\mathrm{H}}_{D,IS} = \hat{\vec{\mathrm{I}}} \cdot \tilde{\mathrm{D}}_{IS} \cdot \hat{\vec{\mathrm{S}}} \tag{3.53}$$

Here $\tilde{\mathrm{D}}$ is the dipolar coupling tensor, and it is traceless and axially symmetric [122], r_{ij} is the distance between the spins. By using the raising and lowering operators $\hat{I}_+$ and $\hat{I}_-$ and transforming the Cartesian coordinates (*x*, *y*, *z*) to the corresponding spherical coordinates (*r*, θ, ϕ) (see Fig. 3.5), the dipolar Hamiltonian ($\hat{\mathrm{H}}_{D,II}$ and $\hat{\mathrm{H}}_{D,IS}$) can be written in terms of a convenient "dipolar alphabet" as [123]

$$\hat{\mathrm{H}}_D = \frac{\mathrm{h}\gamma_i\gamma_j}{r_{ij}^{-3}}\left(\hat{A} + \hat{B} + \hat{C} + \hat{D} + \hat{E}\right) \tag{3.54}$$

where

$$\begin{aligned}
\hat{A} &= \left(1 - 3\cos^2\theta_{ij}\right)\hat{I}_{iz}\hat{I}_{jz} \\
\hat{B} &= -\tfrac{1}{4}\left(1 - 3\cos^2\theta_{ij}\right)\left(\hat{I}_{i+}\hat{I}_{j-} + \hat{I}_{i-}\hat{I}_{j+}\right) \\
\hat{C} &= -\tfrac{3}{2}\sin\theta_{ij}\cos\theta_{ij}e^{-i\phi_{ij}}\left(\hat{I}_{iz}\hat{I}_{j+} + \hat{I}_{i+}\hat{I}_{jz}\right) \\
\hat{D} &= \hat{C}^* = -\tfrac{3}{2}\sin\theta_{ij}\cos\theta_{ij}e^{i\phi_{ij}}\left(\hat{I}_{iz}\hat{I}_{j-} + \hat{I}_{i-}\hat{I}_{jz}\right) \\
\hat{E} &= -\tfrac{3}{4}\sin^2\theta_{ij}e^{-i2\phi_{ij}}\left(\hat{I}_{i+}\hat{I}_{j+}\right) \\
\hat{F} &= \hat{E}^* = -\tfrac{3}{4}\sin^2\theta_{ij}e^{i2\phi_{ij}}\left(\hat{I}_{i-}\hat{I}_{j-}\right)
\end{aligned} \tag{3.55}$$

Since the terms $\hat{A}$ to $\hat{F}$ have a different effect on the eigenfunctions of the Zeeman Hamiltonian, this "dipolar alphabet" form is quite useful in describing the effect of the dipolar coupling.

In the case of homonuclear coupling, the terms $\hat{A}$ and $\hat{B}$ commute with the $\hat{I}_z$ operator of the Zeeman term, which form the secular part of the Hamiltonian. The terms $\hat{C}$, $\hat{D}$, $\hat{E}$ and $\hat{F}$ construct the non-secular part. Only the secular part, which leads to the shifting and splitting of the Zeeman energy levels, is taken into

account, the non-secular part is involved in the spin-lattice relaxation process of spins. Usually the secular part of the dipolar interaction is written as

$$\begin{aligned}\hat{\mathrm{H}}_D &= -d_{ij}\left(3\cos^2\theta_{ij}-1\right)\left[\hat{I}_{iz}\hat{I}_{jz}-\tfrac{1}{4}\left(\hat{I}_{i+}\hat{I}_{j-}+\hat{I}_{i-}\hat{I}_{j+}\right)\right] \\ &= -d_{ij}\left(3\cos^2\theta_{ij}-1\right)\left(3\hat{I}_{iz}\hat{I}_{jz}-\hat{I}_i\cdot\hat{I}_j\right)\end{aligned} \tag{3.56}$$

with the coupling constant

$$d_{ij}=\frac{\mu_0}{4\pi}\cdot\frac{\gamma_i\gamma_j\mathrm{h}}{r_{ij}^3} \tag{3.57}$$

The first spin term $\hat{I}_{iz}\hat{I}_{jz}$ in Eq. (3.56) represents the interaction of one spin with the z-component of the local field produced by the other spin, which causes line broadening. Considering an isolated dipolar couple, *i* and *j*, the resonance of spin *i* will be split into a doublet with a separation of $\frac{3}{2}d_{ij}(3\cos^2\theta\text{-}1)$ due to the two possible values of the static local field. Two absorption lines (fixed angle θ) occur at the frequencies

$$\omega=\omega_0\pm\frac{3}{4}d_{ij}\left(3\cos^2\theta-1\right) \tag{3.58}$$

In a polycrystalline sample, all spins are coupled together and each spin feels a superposition of many local magnetic fields from its coupling neighbors, then each local field gives a contribution to the resonance frequencies of the observed spin. Due to the distance and angle dependence, the size and direction of the local field varies from spin to spin, the dipolar causes a distribution of resonance frequencies and leads to very broad lines in solid, for example, up to 70 kHz for protons.

The second term $\hat{I}_{i+}\hat{I}_{j-}+\hat{I}_{i-}\hat{I}_{j+}$ in Eq. (3.56) is referred to as the "flip-flop" term, which induces an energy-conserving "flip-flop" transition, i.e. the energy required to flip spin *i* (down to up) matches the energy needed to flop spin *j* (up to down) (see Fig. 3.6). For a rigid lattice system, this term is described as a spin diffusion process which

causes efficient transfer of magnetization through the sample, and it is the reason why all ^{1}H nuclei in a uniform single phase solid sample usually have the same spin-lattice relaxation time. When two spins have very different chemical shifts, so that there is no overlap between their resonance frequencies, there can be no energy-conserving transition. The homonuclear dipolar Hamiltonian reverts to the form of the following heteronuclear dipolar Hamiltonian.

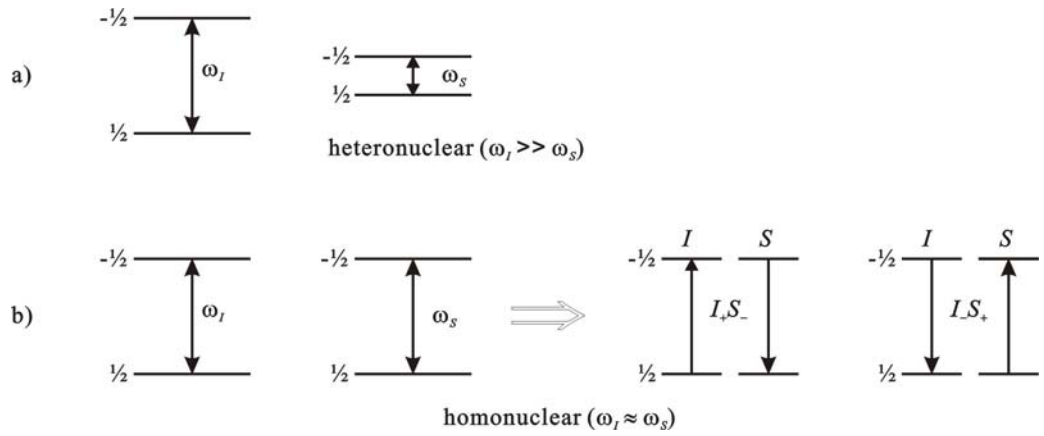

Figure 3.6 a) At different transition frequencies of two spins ω_I and ω_S, no energy-conserving transition can occur; b) when $\omega_I \approx \omega_S$, the spins can exchange the magnetization via an energy-conserving "flip-flop" interaction.

In the case of heteronuclear interaction, only the term $\hat{A}$ commutes with the $\hat{I}_z$ operator of the Zeeman Hamiltonian. Thus the secular part of the heteronuclear dipolar Hamiltonian is given by

$$\hat{\mathrm{H}}_{D,IS} = -\left(\frac{\mu_0}{4\pi}\right)\frac{\mathrm{h}\gamma_I\gamma_S}{r_{IS}^3}\left(3\cos^2\theta_{IS} - 1\right)\hat{I}_z\hat{S}_z \qquad (3.59)$$

The dipolar coupling depends on the orientation, as described by the $(3\cos^2\theta\text{-}1)$ term in the dipolar Hamiltonian. For an isolated C–H pairs in a powder, similar to C–D pairs (see Fig. 3.2), each angle θ between the internuclear vector and the external

magnetic field corresponds to a dipolar coupling containing the term ($3\cos^2\theta$-1). The lines occur at

$$\omega = \omega_0 \pm \frac{1}{2} d_{IS} \left(3\cos^2\theta - 1\right) \tag{3.60}$$

In the presence of the local field from the other spin, each spin gives rise to a distribution of lines with the same qualitative shape. This gives a characteristic powder pattern [130], the Pake doublet, with a separation of d_{IS} as shown in Fig. 3.7. The angle θ_{magic}, corresponding to the point where the two curves cross, is called the "magic angle" and is equal to 54.7°, responsible for the condition ($3\cos^2\theta$-1) = 0.

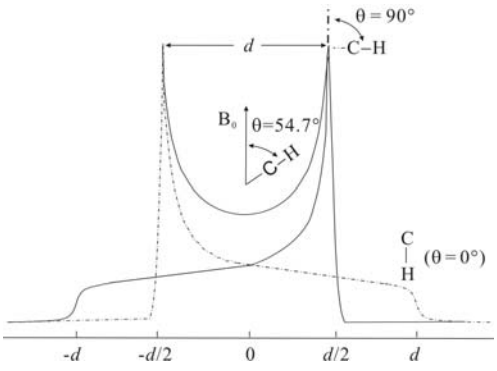

Figure 3.7 Dipolar Pake pattern ("Pake doublet") for isolated C–H pairs distributed at all angles in a powder sample.

The dipolar tensor is an irreducible second-rank tensor and the isotropic value of the dipolar coupling tensor is zero. Since the term d_{ij} depends on r_{ij}, as seen in Eq. (3.57), it provides ample of structural information. For example, the measurement of the distance can be obtained via the distance-dependent strength of the coupling of the spin pair or the diffusive transfer of magnetization (spin diffusion). The latter allows the determination of the domain sizes in heterogeneous samples. The dipolar-dipolar interaction can also give structural information on spin connectivity, spin distributions and polarization transfer.

3.3 Dynamic ^{2}H NMR spectroscopy

3.3.1 Pulse sequences

In this work three types of pulse sequences are applied to create different NMR signals:

i) **The quadrupole echo sequence** (see Fig. 3.8a) is implemented for the detection of the ^{2}H NMR line shapes and in T_2 relaxation experiments [131]. In the normal single pulse detection most of the decay is observed, but the very important initial part is lost during receiver dead time, which is a time required by the receiver to recover from the r.f. pulse. This can cause severe distortion of the NMR line shapes. In order to circumvent this dead time problem, the quadrupole echo sequence, the analogue of the Hahn echo sequence for I = 1 system, is applied [45, 131, 132]. The sequence contains 90°$_x$ and 90°$_y$ pulses separated by an adjustable pulse interval τ_e in the range of μs. 90°$_x$ and 90°$_y$ have a phase-shift of 90°. The first 90$_x^o$ pulse is applied to the

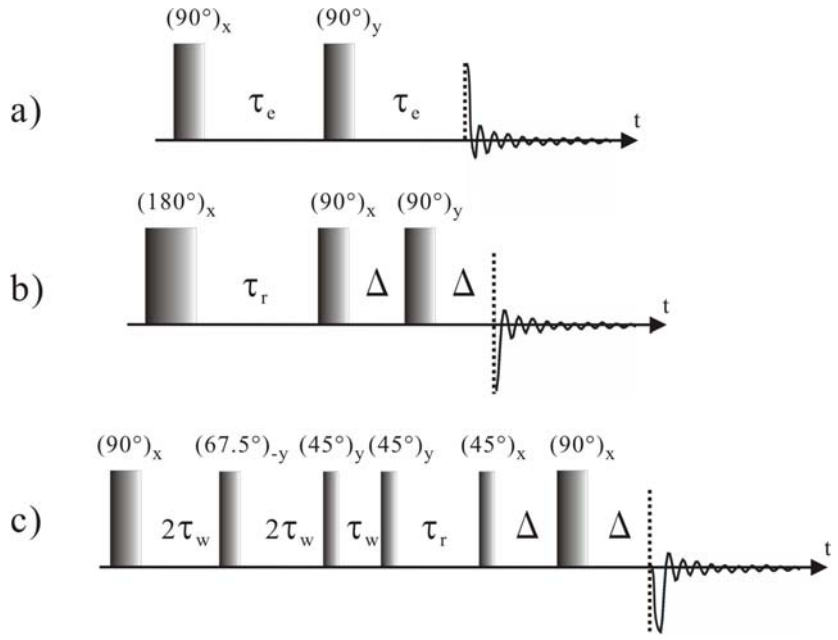

Figure 3.8 Pulse sequence for ^{2}H NMR experiments, a) quadrupole echo sequence; b) inversion recovery sequence; c) broadband Jeener-Broekaert (BBJB) sequence.

spin system, rotates the magnetization down into the XY plane. The transverse magnetization begins to dephase. Putting in a second $90_y°$ pulse to refocus the magnetization, the decay of the echo signal, after another pulse interval τ_e which is slightly larger than the spectrometer dead time and less than T_2, is detected. Therefore, in ^{2}H NMR spectroscopy, the digitization of the FID (free induction decay) begins at the top of the quadrupole echo maximum [131]. The amplitude of the spin echo decreases with the increase of pulse intervals τ_e as a consequence of the loss of phase coherence. By varying the pulse intervals τ_e, T_2 relaxation times are determined.

In the presence of an applied magnetic field, the motion of the microscopic magnetization can be explained in terms of phenomenological differential equations, the Bloch equations [116]

$$\begin{aligned}
\frac{dM_x}{dt} &= \gamma\left(\vec{\mathrm{M}}\times\vec{\mathrm{H}}\right)_x - \frac{M_x}{\mathrm{T}_2} \\
\frac{dM_y}{dt} &= \gamma\left(\vec{\mathrm{M}}\times\vec{\mathrm{H}}\right)_y - \frac{M_y}{\mathrm{T}_2} \\
\frac{dM_z}{dt} &= \gamma\left(\vec{\mathrm{M}}\times\vec{\mathrm{H}}\right)_z + \frac{M_0 - M_z}{\mathrm{T}_1}
\end{aligned} \tag{3.61}$$

where M_x and M_y are the transverse components of the magnetization, M_z is the longitudinal component of the magnetization and M_0 is the thermal equilibrium magnetization.

After solving the Bloch equations, the spin-spin relaxation times can be calculated by using the maximum intensity of each FID recorded at time $t = 2\tau_e$, according to [133, 134]

$$M_z(2\tau_e) = M_0 e^{-(2\tau_e/T_2)} \tag{3.62}$$

ii) **The inversion recovery sequence** is given in Fig. 3.8b, which is used to measure

the spin-lattice relaxation times of the Zeeman order and corresponding partially relaxed spectra [135]. A composite pulse [136], instead of the 180° pulse, is applied to completely invert the magnetization of the spin system. After a variable pulse interval τ_r, the signal is detected by a quadrupole echo sequence with a constant pulse interval Δ = 20 μs. Due to the inversion of the magnetization M_z, the equilibrium state is perturbed. When $M(0)_z = -M_0$, the magnitude of the magnetization M_z at any time can be described from the solution of the Bloch equation as [134]

$$M_z(\tau_r) = M_0\left[1 - 2e^{(-\tau_r/T_{1Z})}\right] \tag{3.63}$$

According to Eq. (3.63), the spin-lattice relaxation times T_{1Z} can be determined with different values of pulse intervals τ_r [135]. For the inversion recovery experiments, in order to let the system have sufficient time to recover the equilibrium state, the recycle delays are set to be at least 5 times of T_{1Z}.

iii) **The broadband Jeener-Broekaert (BBJB) sequence** (see the Fig. 3.8c) is employed to derive the spin-lattice relaxation times of the quadrupole order, T_{1Q}, and corresponding partially relaxed spectra [137]. Here, ($90°_x$-$2\tau_w$-$67.5°_{-y}$-$2\tau_w$-$45°_y$-τ_w-$45°_y$) represents the broadband composite excitation sequence, whose phase cycle maximizes quadrupolar order while fully suppressing Zeeman order [138]. Following an adjustable pulse interval τ_r, a refocusing 90° pulse, in conjunction with the 45° mixing pulse, is used to generate an echo, resulting in partially relaxed spectra with minimal baseline distortion and no first-order phase corrections. The experimental T_{1Q} data were calculated from the intensities of the perpendicular singularities, and were obtained by a two-parameter fit using [19]

$$M(\tau_r) = M(0)e^{-\left(\tau_r/T_{1Q}\right)} \tag{3.64}$$

In this equation, $M(\tau_r)$ is the difference between the peak intensities of the quadrupolar doublet components in anti-phase at time interval τ_r, and M(0) is the initial difference at $\tau_r = 0$.

3.3.2 ^{2}H NMR spectra in the fast exchange limit

Line shape parameters of static molecules in solids give some useful information, but an extremely important aspect of ^{2}H NMR is its use in the study of molecular dynamics. As described above, the quadrupole coupling depends on the orientation of the C–D bond with respect to the external magnetic field, so any molecular motion which brings about a change in that orientation also changes the resonance frequency of the nucleus involved. The spectral features of the observed NMR lineshapes are associated with the rate of motion, which increases with the temperature rising.

Different ^{2}H NMR experiments are sensitive to different motional correlation times τ_c (see Fig. 3.9). In most organic materials, deuterons have conveniently small quadrupole coupling constant, typically δ_{QCC} ~ 140-220 kHz, the most noticeable modifications of powder line shapes occur in the intermediate regime, when $\delta_{QCC}\,\tau_c \approx 1$, and thus involve correlation times from milliseconds to tens of nanoseconds. In the slow motion regime with rates usually < 10^3 s^{-1} the line shape is the same as that for the static molecule, and in the fast motion limit, that is, at rates above ~ 10^8 s^{-1}, the narrowed line shape becomes independent of rate. Slower motion can be studied via selective inversion [139] or two-dimensional exchange experiments [140], and faster motion can be investigated by the analysis of the Zeeman and quadrupolar spin-lattice relaxation [129, 141, 142].

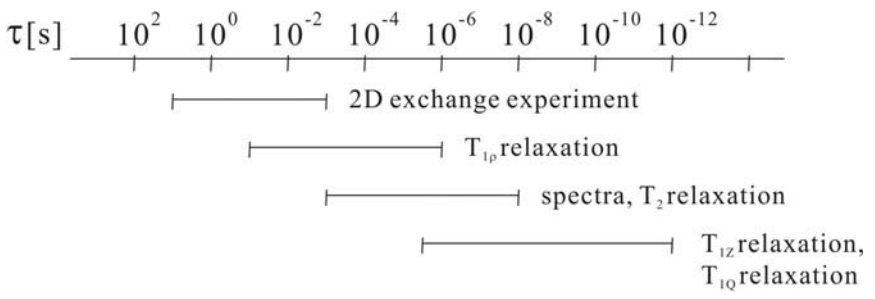

Figure 3.9 Sensitive time-scale of different types of dynamic NMR experiments.

The line shape in the fast motion limit is derived from an effective quadrupolar interaction tensor $\tilde{\mathrm{Q}}^{PAS}$, which is an average of $\tilde{\mathrm{Q}}^{PAS}$ of the deuteron at the sites visited during the motion, and is independent of the pathway. Depending on the rate of reorientation and the orientations of the C–D bond relative to the rotation axis, different line shape averaging is observed. Analytical expressions to calculate the line shapes in the fast motion limit are relatively easy to obtain [45, 129, 132, 143] and it is possible to illustrate motional effects explicitly. For the derivation of analytical expressions, the orientation of the tensor $\tilde{\mathrm{Q}}^{PAS}$ defined in Eq. (3.24) must first be transformed from its principle axis system to the IAS coordinate system, which is defined by the motional symmetry axis [114, 144]

$$\tilde{Q}(\alpha,\beta,\gamma) \;=\; R\tilde{Q}^{PAS}R^{-1} \tag{3.65}$$

with

$$\tilde{\mathrm{Q}}^{PAS} = \frac{3}{4}\cdot\frac{e^2qQ}{h}\begin{bmatrix} 1+\eta & 0 & 0 \\ 0 & 1+\eta & 0 \\ 0 & 0 & -2 \end{bmatrix}$$

where, R is the Euler angle rotation matrix describing the coordinate transformation. The average tensor components are then calculated by using the equilibrium population of the relevant molecular orientations $P_{eq}(\alpha_k, \beta_k, \gamma_k)$ which is necessary for the particular motion under consideration.

$$\bar{Q}_{ij} = \sum\nolimits_k P_{eq}(\alpha_k\beta_k\gamma_k)Q_{ij}^{IAS}(\alpha_k\beta_k\gamma_k) \tag{3.66}$$

The fast motional ^{2}H NMR line shapes are then determined by the residual principal tensor components $\bar{Q}_{ii}^{IAS}$. These quantities, which can be taken directly from the spectral singularities again, are obtained via diagonalization of the averaged tensor matrix, according to [129]

$$\left|\sum\nolimits_j \bar{Q}_{ij} - \delta_{ij}\bar{Q}_{ij}^{PAS}\right| = 0 \tag{3.67}$$

The following Figs. 3.10 and 3.11 illustrate some of the calculated ^{2}H NMR line shapes in the fast exchange regime. If a C–D bond experiences jumps between two positions where the bisector of the jump angle is 54.7° (the magic angle), one component of the quadrupolar interaction tensor which is perpendicular to the jump axis is unaffected by the motion and remains at the static value of $-\frac{1}{2}\omega_Q$ (see Figs. 3.2 and 3.10). Another component of the motionally averaged quadrupolar interaction tensor occurs at zero frequency. The third component occurs at $\frac{1}{2}\omega_Q$, as the tensor must remain traceless.

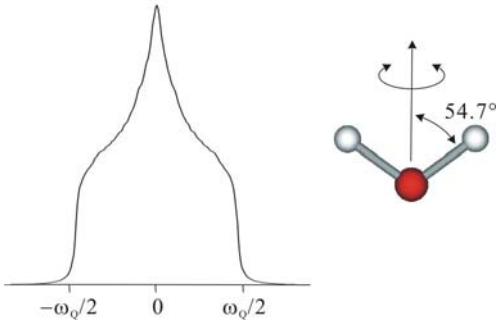

Figure 3.10 ^{2}H NMR spectra for a two-site jump of a C–D bond (fast exchange case).

If the C–D bond is a part of the methyl group, the rotation of the group causes the static line shapes to reduce by a factor of $\frac{1}{2}(3\cos^2\theta - 1)$, with the angle θ between C–D bond and the rotation axis usually being 109.5° (see Fig. 3.11). The splitting is then reduced to $\frac{1}{3}\omega_Q$.

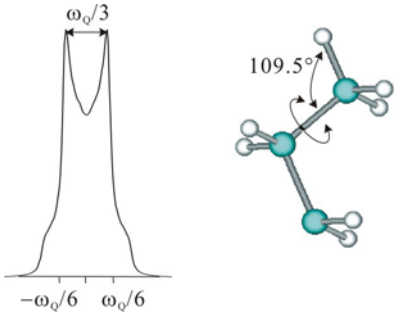

Figure 3.11 ^{2}H NMR spectra of the methyl group rotation (fast exchange case).

3.3.3 Intermediate rate ^{2}H NMR line shapes and T_2 relaxation

Intermediate rate line shapes vary with temperature in a very complex manner, depending on the specific rate of motion and the experimental details, and the interpretation of these line shapes has to resort to numerical calculations.

The theoretical description of the quadrupole echo experiment can be done in the framework of evolution of the density matrix. It is found that the numerical calculation of the quadrupole echo experiment for species *i* in the rotating frame is tightly related to an effective complex magnetization $G_i(t)$, defined as [132]

$$G_i(t) = y_i(t) + ib_i(t) \tag{3.68}$$

Here $y_i(t)$ is the expectation value of the magnetization, $b_i(t)$ corresponds to an NMR unobservable coherence. After a 90° pulse the detected signal is proportional to $\mathrm{Re}\{G_i(t)\}$. This complex magnetization obeys a Bloch-type equation

$$\frac{d}{dt}G_i(t) = -\left(i\omega_{Q,i} + \frac{1}{T_{2,i}}\right)G_i(t) \tag{3.69}$$

The relaxation term contains the effects of inhomogeneous interactions, which stems from interactions like dipolar interactions or magnetic field inhomogeneity. After the second 90° pulse, $G_i(t)$ is converted into its complex conjugate

$$G_i(t) \xrightarrow{90°_y} G_i^*(t) \tag{3.70}$$

If chemical exchange is considered with an arbitrary number of sites, Eq. (3.69) is extended to account for the kinetic rate constants, as follows [145]

$$\frac{d}{dt}G_i(t) = -\left(i\omega_{Q,i} + \sum_{j\neq i}k_{ji} + \frac{1}{T_{2,i}}\right)G_i(t) + \sum_{j\neq i}k_{ij}G_j(t) \tag{3.71}$$

Here the elements $\omega_{Q,i}$ describe the frequencies of the exchanging sites. The specific jump rates are given by k_{ij}, which indicate the jump from site *j* to *i* [146].

The correlation times τ_c for a jump process follow the detailed balance and are related to the jump rates k_{ij} by

$$\frac{1}{\tau_c} = \frac{k_{ij}}{p_i} \tag{3.72}$$

where, p_i is the equilibrium population of the site i.

The magnetization can be described by defining a vector $\vec{G}(t)$, which has the components $G_i(t)$ given in Eq. (3.68), as follows [132]

$$\frac{d}{dt}\vec{G}(t) = -\tilde{\mathrm{R}} \cdot \vec{G}(t) = (i\Omega + \mathrm{K}) \cdot \vec{G}(t) \tag{3.73}$$

Here, the diagonal matrix **Ω** describes the frequencies of the exchange sites, **K** is the kinetic matrix. The matrix elements of both **Ω** and **K** are given by

$$\Omega = \begin{bmatrix} -\omega_{Q,1} & & & \\ & -\omega_{Q,2} & & \\ & & \ddots & \\ & & & -\omega_{Q,N} \end{bmatrix} \tag{3.74}$$

$$\mathrm{K} = \begin{bmatrix} -\sum_{i\neq 1} k_{i1} - \frac{1}{T_{2,1}} & k_{12} & \cdots & k_{1N} \\ k_{21} & -\sum_{i\neq 2} k_{i2} - \frac{1}{T_{2,2}} & \cdots & k_{2N} \\ \vdots & \vdots & \ddots & \vdots \\ k_{N1} & k_{N2} & \cdots & -\sum_{i\neq N} k_{iN} - \frac{1}{T_{2,N}} \end{bmatrix} \tag{3.75}$$

R is also a matrix and has the elements

$$\begin{aligned} R_{ii} &= i\omega_{Q,i} + \sum_{j\neq i} k_{ji} + \frac{1}{T_{2,i}} \\ R_{ij} &= -k_{ij},\ i \neq j \end{aligned} \tag{3.76}$$

The first order differential equation, Eq. (3.73), can be solved as follows

$$\vec{G}(t) = e^{-\tilde{R}\cdot t}\vec{G}(0) \tag{3.77}$$

$\vec{G}(0)$ is directly proportional to the relative population of a site *i* in the equilibrium state. In the quadrupole echo experiment, the whole magnetization after the first $90°_x$ pulse lies along the y-coordinate axis. During the time interval τ_e between the two pulses the complex magnetization evolves according to Eq. (3.73), then before the second $90°_y$ pulse

$$\vec{G}(\tau_e^{-}) = e^{-\tilde{R}\cdot\tau_e}\vec{G}(0) \tag{3.78}$$

Just after this pulse, the further evolution of the magnetization can be described with Eq. (3.70) by

$$\vec{G}(\tau_e^{+}) = \vec{G}^{*}(\tau_e^{-}) = \left(e^{-\tilde{R}\cdot\tau_e}\right)^{*}\vec{G}(0) \tag{3.79}$$

The echo signal is detected at time point of $2\tau_e$, and the complex magnetization $G_i(2\tau_e)$ is given by the integration of $G_i(\tau_e)$ in the time interval from τ_e to $2\tau_e$

$$\vec{G}(2\tau_e) = e^{-\tilde{R}\cdot\tau_e}\vec{G}(\tau_e^{+}) = e^{-\tilde{R}\cdot\tau_e}\left(e^{-\tilde{R}\cdot\tau_e}\right)^{*}\vec{G}(0) \tag{3.80}$$

If finite pulse effects are neglected and only infinitesimally sharp δ–pulses are assumed, the intensity of the quadrupole echo signal $S(t,2\tau_e)$ is expressed as

$$S(t,2\tau_e) = \vec{1}\cdot\vec{G}(2\tau_e + t) = \vec{1}\cdot e^{-\tilde{R}\cdot t}\vec{G}(2\tau_e) = e^{-\tilde{R}\cdot t}e^{-\tilde{R}\cdot\tau_e}(e^{-\tilde{R}\cdot\tau_e})^{*}\vec{G}(0) \tag{3.81}$$

where $\vec{1} = (1,1,\cdots,1)$. The magnetization evolves during the decay intervals τ_e and the time *t*. The absorption spectrum is obtained from the Fourier transformation of $S(t,2\tau_e)$

$$S(\omega) = \int_0^{\infty} S(t,2\tau_e)e^{i\omega t}dt \tag{3.82}$$

With the help of a eigenvector matrix **χ**, the matrix $\tilde{R}$ can be re-expressed as a diagonal matrix **Λ** which has the eigenvalues λ_i, namely [133]

$$e^{\tilde{R}\tau_e} = \chi e^{\Lambda\tau_e}\chi^{-1}$$
$$e^{-\tilde{R}\tau_e} = \chi e^{-\Lambda\tau_e}\chi^{-1} \tag{3.83}$$

where $\chi^{-1}\tilde{R}\chi = \Lambda$. After substituting Eq. (3.83) back into Eq. (3.81), the signal of the echo amplitude is obtained

$$S(t,2\tau_e) = \vec{1}\cdot\chi e^{\Lambda t}\chi^{-1}\vec{G}(2\tau_e) = \sum_{ijk}\chi_{ik}e^{\lambda_k t}(\chi^{-1})_{kj}G_j(2\tau_e) \tag{3.84}$$

According to Eq. (3.82), the absorption spectrum becomes

$$S(\omega) = \sum_{ijk}\frac{\chi_{ik}\lambda_k t(\chi^{-1})_{kj}}{\omega^2+\lambda_k^2}G_j(2\tau_e) \tag{3.85}$$

Analysis of the line shape in the fast motion limit gives possible models for the motion and some geometric information. The intermediate rate line shape simulations can confirm a model or distinguish between different motions which give an identical fast motion limit. They can also be used to derive the activation energy E_a for the motion. The best-fits of the experimental spectra provide the correlation times as a function of temperature. According to the Arrhenius law

$$\tau_c = \tau_0 e^{(E_a/RT)} \tag{3.86}$$

E_a can be obtained from the slope of the corresponding Arrhenius plot. Sometimes two distinct motions may produce dynamic averaging in the same temperature region and simulations may make it possible to determine which process is faster or whether the two are simultaneous. All these applications rely on subtle differences in the intermediate rate line shapes.

3.3.4 Spin-lattice relaxation times (T_{1Z} and T_{1Q})

For the line shape analysis, there exist some weaknesses, one of which is the need for model-dependent simulations. When particular model parameters have been adjusted

to reproduce the spectra, it might be possible that another, quite different model may fit the data equally well. For instance, the line shapes with temperature-dependent and site-specific populations might in some circumstances be misinterpreted by a motion with equal populations and a temperature-dependent distribution of rates [147-149]. In order to avoid wrong conclusions, it is required that any model fits not only the line shape and its pulse spacing dependence (T_2 anisotropy), but also the anisotropy in spin lattice relaxation time T_{1Z} [142, 147].

In what concerns fast motion, when motional correlation times are on the order of the inverse of the Larmor frequency (10^8 – 10^{12} s^{-1}), the kinetic features and parameters are analyzed with the spin-lattice relaxation times (T_{1Z}, T_{1Q}). In the Redfield approximation which assumes the motional correlation times (τ_c) are smaller than the spin-lattice relaxation times (T_{1Z}) [150, 151], the spin lattice relaxation times of the Zeeman order T_{1Z} and quadrupole order T_{1Q} are given by [141, 142, 152]

$$\frac{1}{T_{1Z}} = \frac{3\pi^2}{2}(e^2 q_{zz} Q/h)_0^2 \left[J_1^Q(\omega_0) + 4J_2^Q(2\omega_0) \right] \tag{3.87}$$

and

$$\frac{1}{T_{1Q}} = \frac{9\pi^2}{2}\left(e^2 q_{zz} Q/h\right)_0^2 J_1^Q(\omega_0) \tag{3.88}$$

here $J_1^Q(\omega_0)$ is the spectral density function corresponding to single quantum spin flips, and $J_2^Q(2\omega_0)$ to two-quantum spin flips. Both functions are orientation dependent in solids, and since the powder pattern is an inhomogeneous superposition of spectra from randomly oriented crystallites, the T_{1Z} and T_{1Q} vary across the line shapes.

The spectral density functions J_m^Q can be calculated via Fourier transformation of the auto-correlation function $C_m^Q(t)$

$$J_m^Q(\omega) = \int_0^\infty e^{-i\omega t} C_m^Q(t)\, dt \tag{3.89}$$

The auto-correlation function has the form [142]

$$C_m^Q(t) = \left\langle V_{2m}^{LAB}(0) V_{2m}^{LAB*}(t) \right\rangle - \left| \left\langle V_{2m}^{LAB}(0) \right\rangle \right|^2 \tag{3.90}$$

The quantities $V_{2m}^{LAB}(t)$ are irreducible tensor components of the electric field gradient in laboratory fixed axes, and are time dependent as a result of molecular motion. It is worth mentioning that in Eqs. (3.87) and (3.88) the static quadrupole coupling constant $\left(e^2 q_{zz} Q/h\right)_0$ is used. However, the corresponding experimental line shape reflects a motionally averaged value, $\left(e^2 q_{zz} Q/h\right)_{eff}$, which depends on the symmetry and type of the motion (see chapter 3.3.2). The correlation functions $C_m^Q(t)$ and the average tensor components $\left\langle V_m^{LAB}(t) \right\rangle$ can be calculated by using the formalism of Torchia and Szabo [141].

The spectral density function J_m^Q for an n-site jump is given by [100, 153]

$$\begin{aligned} J_m^Q(\omega) = 2 \sum_{a,a'=-2}^{2} d_{ma}^{(2)}(\theta') d_{ma'}^{(2)}(\theta') \cdot \sum_{n,l,j=1}^{N} X_l^{(0)} X_l^{(n)} X_j^{(0)} X_j^{(n)} \\ \cdot d_{0a}^{(2)}(\theta_l'') d_{0a'}^{(2)}(\theta_j'') \cdot \cos(a\phi_l - a'\phi_j) \frac{\lambda_n}{\lambda_n^2 + \omega^2} \end{aligned} \tag{3.91}$$

with $\phi_i = \phi_i'' - \phi'$, $X^{(n)}$ and λ_n are the corresponding eigenvector and eigenvalues of the symmetric exchange matrix **K**. The angles θ'' and ϕ'' are the Euler angles between the principal axis system (PAS) and the intermediate axis system (IAS). The angles θ' and ϕ' represent the orientation of the IAS and LAB system. $d_{ma}^{(2)}(\theta)$ are the elements of the reduced Wigner rotation matrix [122].

In the inversion recovery pulse sequence, a pulse delay τ_r exists between the 180° pulse and the quadrupole echo sequence. The absorption signal $S_{IR}\left(t, 2\tau_e, \tau_r\right)$ can be

obtained by multiplying the quadrupole echo signal $S(t,2\tau_e)$ (Eq. (3.84)) with the factor $1-2e^{-(\tau_r/T_{1Z})}$, yielding [129]

$$S_{IR}\left(t,2\tau_e,\tau_r\right)=\left[1-2e^{-(\tau_r/T_{1Z})}\right]S(t,2\tau_e) \tag{3.92}$$

Equation (3.91) describes the general case for the calculation of the spectral density functions relevant to spin-lattice relaxation time. For a series of simple motional processes the analysis of the spin-lattice relaxation times can be implemented by using available analytical expressions [154]. In the presence of both spin-lattice and spin-spin relaxation contributions, based on Eqs. (3.87) and (3.91) the angular dependent T_{1Z} values can be calculated; line broadening effects from spin-spin relaxation are accessible by solving Eq. (3.84) [155]. Equation (3.92) is the combination of both contributions.

For solids, quadrupole order over a full width powder pattern can be created by means of a broadband composite excitation sequence, including an echo pulse to move the resulting signal beyond the receiver dead time (BBJB) [137, 138, 156]. Similarly, in the broadband Jeener-Broekaert (BBJB) pulse sequence, the absorption signal $S_{JB}\left(t,\tau_r\right)$ can be calculated by

$$S_{JB}\left(t,\tau_r\right)=e^{-(\tau_r/T_{1Q})}S_{anti}(t) \tag{3.93}$$

Here τ_r is a pulse delay between the excitation pulse sequence and the detect pulse; $S_{anti}\left(t,\tau_r\right)$ is anti-phase quadrupole echo signal.

3.3.5 Motional models and numerical simulation

Based on the above-detailed theoretical approaches and assumptions, a general FORTRAN program [7, 157, 158] combining various types of molecular motions for the systems under investigation was developed to derive the theoretical NMR spectra

and relaxation effects for $I = 1$ spin systems. The reproduction of experimental spectra and relaxation effects can confirm the mechanism of the molecular reorientation processes and relevant kinetic parameters are derived. Several ^{2}H NMR studies of reorientation modes of molecules in molecular solids, inclusion compounds and liquid crystalline mesophases have been reported [158-160]. In what follows is a brief introduction to the models that will be used in this thesis work. Mainly taking the 2-site exchange model as an example, a series of representative plots about the impacts of various molecular or simulation parameters, such as motional correlation times, equilibrium populations of the various jump sites, opening angle, on the theoretical ^{2}H NMR line shapes and on relaxation data is addressed.

3-site jump model. Here it represents the jump between three sites defined by a particular population probability p_i (i = 1, 2, 3). Each site refers to a particular orientation of the molecule around the motional axis. This orientation is characterized by the angle θ between the motional symmetry axis and the C–D bond (the three C-D bond directions depict a cone with opening angle 2θ), and by the azimuthal jump angle Δϕ between the sites (see Fig. 3.12). When θ = 90°, i.e. the C–D lies in a plane, the molecules are ordered in this plane, and can experience discrete jumps by Δϕ = ±120° about the symmetry axis.

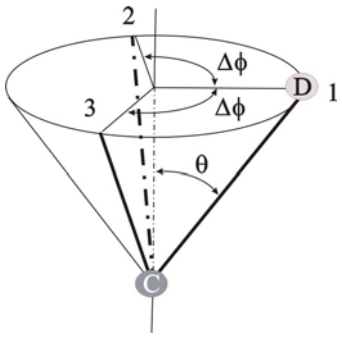

Figure 3.12 Schematic representation of a jump process between three sites 1, 2, and 3.

Figure 3.13 shows the effect of the relative population p_1 on the ^{2}H NMR spectra calculated for the quadrupolar echo sequence with a constant delay τ_e = 20 μs. These

theoretical spectra were obtained with the assumption of the 3-site jump motion around a motional symmetry axis which is perpendicular to the C–D bond direction, and the populations follow $p_1 + p_2 + p_3 = 1$ and $p_2 = p_3$. The ^{2}H NMR spectra are affected significantly by the variation of the equilibrium populations.

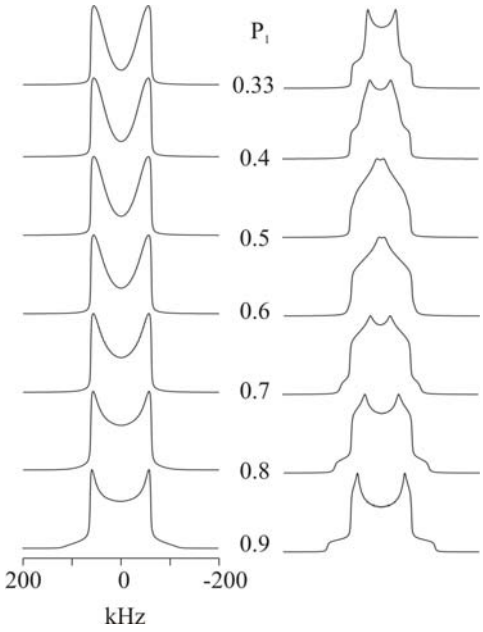

Figure 3.13 Theoretical ^{2}H NMR line shapes (quadrupole echo, τ_e = 20 μs) for a non-degenerate 3-site jump process with different populations p_1 (as annotated), and at correlation times of 1×10^{-6} s (left) and 1×10^{-7} s (right) and $\theta = 90°$.

2-site exchange model. This model describes the restricted chain rotation or 2–site gauche-gauche exchange. Model calculations are given in Figs 3.14 to 3.17, which show the influence of the opening angle θ between the C–D bond and the jump axis and the jump angle Δϕ on the line shapes and relaxation anisotropy. With the assumption of the C–D bond is perpendicular to motional symmetry axis, the effects of the jump angle Δϕ on the ^{2}H NMR spectra at two different correlation times can be illustrated by Fig. 3.14.

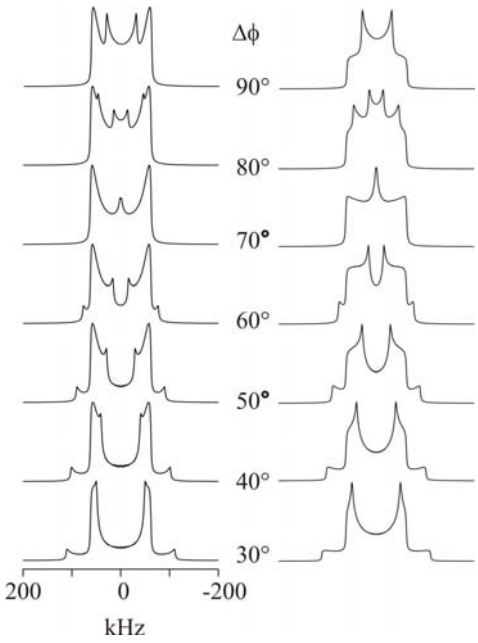

Figure 3.14 Theoretical ^{2}H NMR line shapes (quadrupole echo, τ_e = 20 μs) for a degenerate 2-site jump process with different jump angle $\Delta\phi$ (as annotated), and at correlation times of 3 × 10^{-6} s (left) and 3 × 10^{-7} s (right) and θ = 90°.

In Fig. 3.15 three series of partially relaxed ^{2}H NMR spectra from the quadrupole echo sequence are given which were obtained on the basis of a degenerated 2-site jump motion with three different opening angles θ. The observed changes in the partially relaxed ^{2}H NMR spectra, as a function of the pulse spacing τ_e, are a direct measure of the angular dependence of T_2 [119, 128], which strongly depends on the particular model assumptions. The influence of the different opening angles between the C-D bond direction and the motional symmetry axis is demonstrated clearly from the presented spectra.

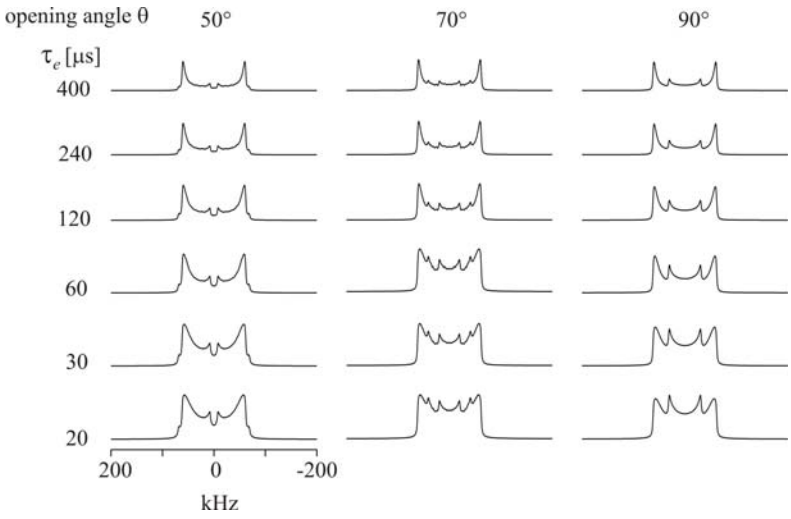

Figure 3.15 Theoretical ^{2}H NMR line shapes (quadrupole echo, partially relaxed spectra) for a degenerated 2-site jump process at different angles $\theta = 50°$, 70° and 90° between the C-D bond direction and the motional symmetry axis. The motional correlation time is 2×10^{-6} s and the jump angle $\Delta\phi$ is 90°.

Figure 3.16 illustrates the partially relaxed ^{2}H NMR spectra from the modified inversion recovery sequence, assuming the jump motion in the fast exchange limit and the C-D bond perpendicular to the motional symmetry axis. The three series of spectra demonstrate the influence of the jump angle $\Delta\phi$ on the spin-lattice relaxation. The characteristic changes of these spectra as a function of the relaxation period τ_r after the inversion pulse demonstrate that the relaxation rate is not identical across the ^{2}H NMR spectrum, which is a direct consequence of the angular dependence of T_1 anisotropy [100, 119, 161]. The spectra are plotted with the same absolute intensity in order to show the relaxation effects in detail.

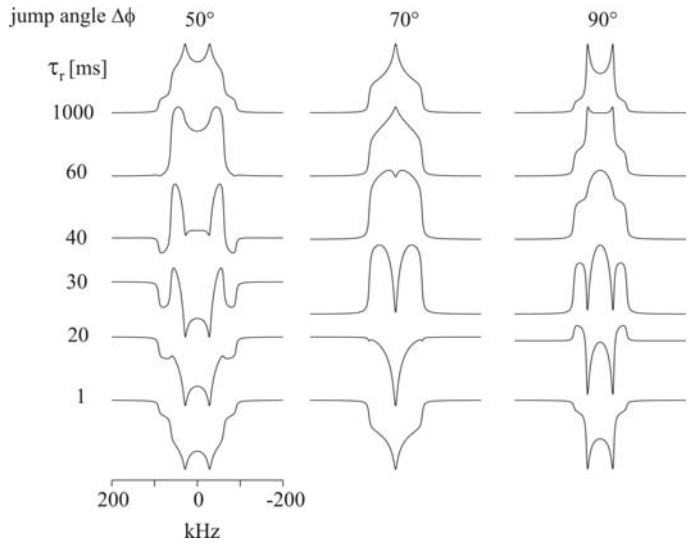

Figure 3.16 Theoretical ^{2}H NMR line shapes (inversion recovery sequence, Δ = 20 μs) for a degenerate 2-site jump process with different jump angles $\Delta\phi$ = 50°, 60° and 70° at correlation time of 1×10^{-10} s and θ = 90°.

Partially relaxed ^{2}H NMR spectra from broadband Jeener Broekaert sequence are depicted in Fig. 3.17. As indicated, the anisotropy profile of the relaxation time, T_{1Q}, has a strong dependence on the motional rate [4, 138, 142].

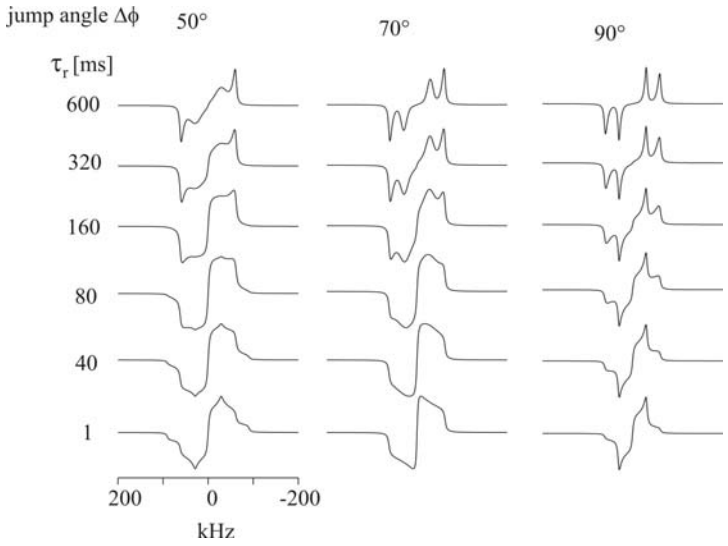

Figure 3.17 Theoretical ^{2}H NMR line shapes (broadband Jeener Broekaert sequence, Δ = 20 μs) for a degenerate 2-site jump process with different jump angles $\Delta\phi$ = 50°, 60° and 70° at correlation time of 1×10^{-10} s and θ = 90°.

19-site wobbling model. Molecule wobbling process can be taken into account as 19–site small angle jump as proposed by Vold et al. [162]. Based on an extension to the 3–site jump model, 19–site wobbling process can be described by a pole when θ = 0 and two overlapping cones with different opening angles θ and 2θ, respectively. The distribution of the jump sites takes the form: the unique site 1 at the pole, the inner cone includes 6 equally spaced sites, the other twelve sites (site 8–19) locate in the ring with opening angle 2θ (see Fig. 3.18). The chemical exchange only takes place between neighboring sites. The populations of the wobbling sites are variable.

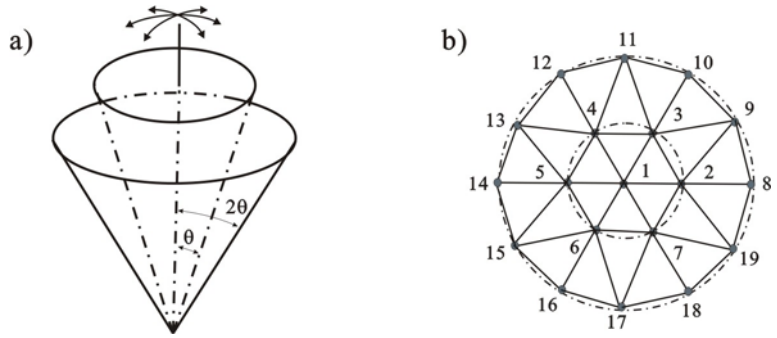

Figure 3.18 a) The cone model motion, b) Site designations of the 19-site wobbling model.

3.4 High resolution ^{13}C CP/MAS and ^{1}H MAS NMR spectroscopy

In this section, a general description of high resolution ^{13}C and ^{1}H (both are I=1/2 spins) NMR spectroscopy will be given. First, the employed pulse sequences will be briefly described, followed by an introduction of the magic angle spinning which is commonly used for spin-1/2 systems. Bearing in mind that the basic internal interactions of the strongly coupled spin-1/2 system mainly lie in the chemical shift interaction and the direct dipolar-dipolar interaction, these internal interactions under magic angle spinning will be partially averaged. Then, the cross polarization technique will be introduced, and the relaxation mechanism most often encountered in spins-1/2 systems will be outlined finally.

3.4.1 Pulse sequence

Five types of pulse sequences are employed for spectrum acquisition and relaxation measurements. The ^{1}H spectra are obtained by a single pulse, as shown in Fig. 3.19a. The pulse sequence of the normal CP experiment is given in Fig. 3.19b. First, the proton magnetization is brought to the x-axis by a 90° pulse and held there by the spin locking pulse. The proton spins are locked for a time period τ_{CP}, know as the "contact time". During this time period a strong on-resonance pulse is applied to the ^{13}C spins, which is also oriented along the x-axis. If the Hartmann-Hahn condition is met and the two spin locking fields are matched, the magnetization is exchanged between the ^{1}H and ^{13}C. After the carbon magnetization has built up during the contact time, the ^{13}C spins are detected while ^{1}H spins are decoupled. The carbon signal can be enhanced by a factor $\gamma_{^{1}H} / \gamma_{^{13}C} \approx 4$.

^{1}H $T_{1\rho}$ relaxation times are determined by inserting a variable interval τ following the ^{1}H spin-locking process between the 90° pulse of ^{1}H and the CP contact time in the normal CP pulse sequence (see Fig. 3.19c). After the initial, rapid buildup of carbon polarization, the carbon signal tracks the polarization in the proton reservoir and thus follows its decrease via the ^{1}H $T_{1\rho}$ process [163]. In contrast, for the measurement of ^{13}C $T_{1\rho}$, the insertion of a variable interval τ with ^{13}C spin-locking process is after CP contact (see Fig. 3.19d), in this case the ^{13}C signal registers the decay via the ^{13}C $T_{1\rho}$ process [164]. ^{1}H and ^{13}C $T_{1\rho}$ relaxation times are calculated from the following equations, respectively

$$M(\tau) = M_0 e^{-\left(\tau / T_{1\rho(H)}\right)} \tag{3.94}$$

$$M(\tau) = M_0 e^{-\left(\tau / T_{1\rho(C)}\right)} \tag{3.95}$$

^{13}C T_1 relaxation times are obtained with cross-polarization (CP) excitation as proposed by Torchia et al. (see Fig. 3.19e) [165]. During the variable interval τ, the

^{13}C magnetization evolves without either spin-locking or CP contact. The calculation procedure is described by

$$M(\tau) = M_0 e^{-\left(\tau / T_{1(C)}\right)} \tag{3.96}$$

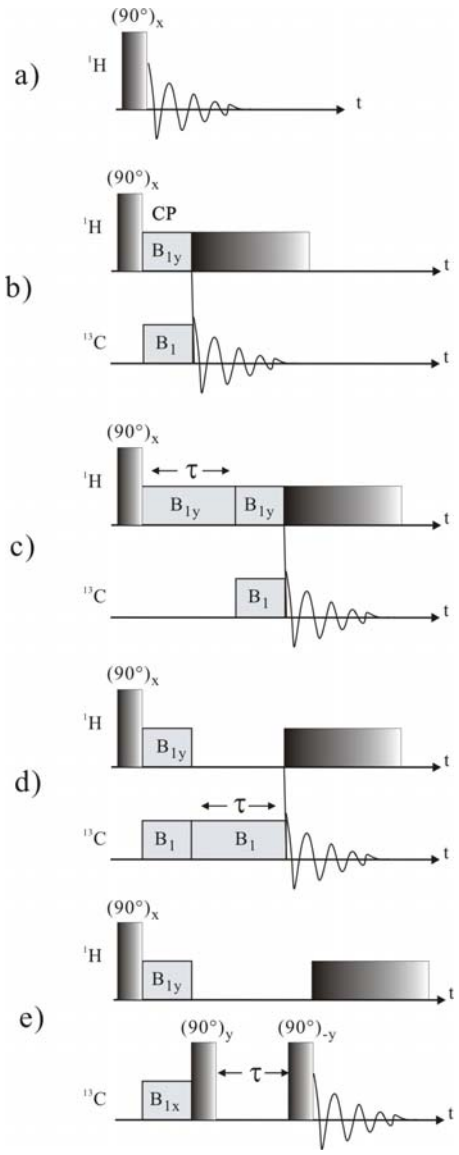

Figure 3.19 Pulse sequences used in different ^{1}H and ^{13}C MAS NMR experiments, a) single pulse for ^{1}H spectra, b) cross polarization pulse sequence for ^{13}C spectra, c)-e) pulse sequences for the measurements of ^{1}H $T_{1\rho}$, ^{13}C $T_{1\rho}$ and ^{13}C T_1, respectively.

3.4.2 Magic angle sample spinning

Spin interactions can be manipulated by rotating a sample about an axis inclined by an angle θ toward the magnetic field B_0. If this rotation is at the "magic angle", all second rank interactions can be averaged out. When a sample is spinning at the spinning rate ω_r, all spin interaction are time-dependent and sidebands with the separation ω_r are created. If the spinning rate is much greater than the anisotropic spin interaction, the sidebands are well separated from the central line and become vanishingly small with increasing ω_r [166-168].

Magic angle spinning can either be used on its own, or be combined with other line-narrowing techniques. For instance, it can be in conjunction with multiple pulse sequence to obtain high resolution NMR spectra, especially for hydrogen and fluorine nuclei in solids, or be combined with cross-polarization and high power heteronuclear decoupling methods to get the high resolution spectra for ^{13}C, ^{29}Si and other low abundant nuclei. In spin-1/2 solids, the line broadening mainly arises from direct dipole-dipole interaction and electron shielding interaction. In what follows the effect of MAS on each of them will be discussed.

3.4.3 Chemical shift and magic angle spinning

Fast spinning a polycrystalline powder sample around an arbitrary axis, the molecules rapidly experience all possible orientations, and hence, even a strongly asymmetric electron distribution will appear spherical when viewed on the NMR timescale. The chemical shift Hamiltonian can be divided into an isotropic term and an anisotropic term. For the axially symmetric ellipsoid case, in which $\sigma_{xx} = \sigma_{yy}$, the chemical shift Hamiltonian can be written as

$$\hat{H}_{cs} = \hbar\omega_0 \hat{I}_z \sigma_{iso} + \tfrac{1}{2}\left(\sigma_z - \sigma_{iso}\right)\left(3\cos^2\theta - 1\right)\hbar\omega_0 \hat{I}_z \tag{3.97}$$

When an array of nuclei in a solid sample is rotated with angular velocity ω_r about an axis inclined at angle θ_m to B_0 and at angle β to the principal axes of $\tilde{\sigma}$ tensor, the chemical shift Hamiltonian becomes time dependent and is expressed as

$$\hat{H}_{cs} = \mathrm{h}\omega_0 \hat{I}_z \sigma_{iso} + \tfrac{1}{2}\left(\sigma_z - \sigma_{iso}\right)\left[\left(3\cos^2\theta_m - 1\right)\left(3\cos^2\beta - 1\right) + \xi(t)\right]\mathrm{h}\omega_0 \hat{I}_z \tag{3.98}$$

with

$$\xi(t) = C_1\cos(\omega_r t) + C_2\cos(2\omega_r t) + S_1\sin(\omega_r t) + S_2\sin(2\omega_r t)$$

Here C_1, C_2, S_1 and S_2 are the functions of the Euler angles involved in the coordinate transformation. In the right hand side of Eq. (3.98), the first term (isotropic part) is invariant under motion; the first term in the square bracket reflects the averaged anisotropy of the chemical shift tensor which depends on the angle between the spinner axis and the external magnetic field B_0. When the angle $\theta_m = 54.7°$, the value of the $(3\cos^2\theta_m\text{-}1)$ term in the CAS Hamiltonian is zero, the shift anisotropy is removed from the NMR spectrum. If the angle θ_m deviates from the magic angle, a scaled anisotropy is observed. The second term in the square bracket gives rise to sidebands. When the spinning rate is not fast enough to exceed the width of the static line shape, the powder pattern breaks up into relatively narrow lines at the isotropic chemical shift (center band) and sidebands at multiples of ω_r from the center band.

3.4.4 Dipole-dipole interaction and magic angle spinning

If a solid sample is rotated uniformly with angular velocity ω_r, every internuclear vector r_{ij} tilted relative to the rotation axis describes a conical figure about the rotation axis, retracing the same path during each complete circuit (see Fig. 3.20a). The relationship between r_{ij} and B_0 in a reference frame, where z is along the rotation axis, is displayed in Fig. 3.20b. The direction of r_{ij} is fixed in this rotor based frame with a

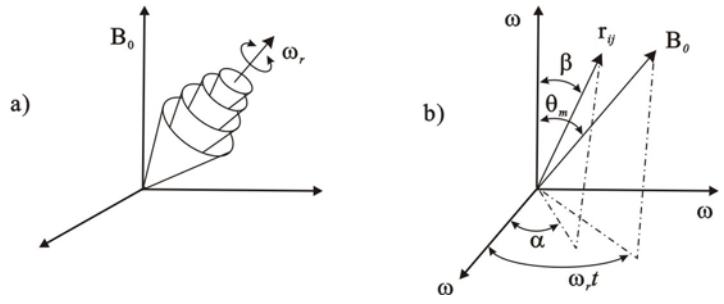

Figure 3.20 Schematic representation of magic angle spinning. a) the unique internuclear vector r_{ij} moves along a cone whose axis is always inclined at θ_m relative to B_0. b) r_{ij} and B_0 viewed in the rotor frame ω_x–ω_y–ω_z.

polar angle β and an azimuthal angle α. B_0 appears to precess about the z axis of the rotor frame, maintaining a fixed angle θ_m while sweeping out an azimuthal angle ($\omega_r t$). Hence the instantaneous angle θ_{ij} between B_0 and r_{ij} becomes time-dependent and the factor ($3\cos^2\theta_{ij}$-1) in Eq. (3.56) runs through a range of values that may be positive or negative. Its average value may be made zero by a judicious choice of θ_m. $\cos\theta_{ij}$ can be expressed in terms of the other angles in the system by using the spherical law of cosine, as

$$\cos\theta_{ij}(t) = \cos\theta_m \cos\beta + \sin\theta_m \sin\beta \cos(\alpha - \omega_r t) \tag{3.99}$$

θ_{ij} becomes time dependent, so does the homonuclear dipolar Hamiltonian.

$$\begin{aligned}\hat{H}_D = \sum_{i<j} \frac{\mu_0}{4\pi} \cdot \frac{\gamma_i \gamma_j \mathrm{h}}{2r_{ij}^3} \left(\hat{I}_i \hat{I}_j - 3\hat{I}_{iz}\hat{I}_{jz}\right) \Big[\tfrac{1}{2}\left(3\cos^2\theta_m - 1\right)\left(3\cos^2\beta - 1\right) \\ + \tfrac{3}{2}\sin 2\theta_m \sin 2\beta \cos\left(\alpha - \omega_r t\right) + \tfrac{3}{2}\sin^2\theta_m \sin^2\beta \cos 2\left(\alpha - \omega_r t\right) \Big]\end{aligned} \tag{3.100}$$

Here the first term in the square bracket is constant, which gives a reduced dipolar interaction and the narrowed spectrum, while the second and the third term are periodic in ω_r and $2\omega_r$ with zero mean value and give rise to rotational sidebands at multiples of ω_r. (For heteronuclear dipolar interaction, a similar expression to Eq. (3.100) can be obtained.)

Equation (3.100) indicates that when θ_m = 54.7°, the factor $(3\cos^2\theta_m-1) = 0$, the rotation about an axis at the magic angle 54.7° should reduce the dipolar broadening to zero; when θ_m = 90°, i.e. rotation about an axis perpendicular to B_0, $|(3\cos^2\theta_m-1)| = 1/2$, so the powder pattern is scaled down by a factor of 2; when θ_m = 0°, the factor $(3\cos^2\theta_m-1) = 1$, the rotation about B_0 does not affect the dipolar interaction.

Theoretically, provided the magic angle spinning rate ω_r is larger than the linewidth resulting from the dipolar interaction, the dipolar broadening may be eliminated. In practice, it is usually not possible to spin faster than the dipolar linewidth. Especially for the case of dominant homonuclear dipolar interactions, and for abundant-spin situations such as ^{1}H and ^{19}F (at ca. tens of kHz rate), magic angle spinning with high frequencies (> 30 kHz) in combination with other line narrowing techniques, such as multiple pulse operation, has to be used to achieve line narrowing. In the situation of dominant heteronuclear dipolar interactions, such as ^{13}C and ^{29}Si NMR spectra, high power heteronuclear decoupling is performed in the experiment.

3.4.5 Cross polarization

The nuclei with low natural abundance, such as ^{13}C and ^{29}Si, have low spin polarization, hence in NMR experiment their sensitivity will be less. In addition, shorter transverse relaxation times and residual anisotropic broadening (homo- and hetero-nuclear dipolar-dipolar coupling) not completely averaged by rotation reduce not only the resolution but also S/N ratio in NMR spectra. The S/N ratio roughly scales with the inverse of the linewidth, as the integral intensity of the whole line is constant.

In order to enhance the signals from rare nuclei, such as ^{13}C and ^{15}N, a technique

called cross polarization (CP) [122, 169, 170] is used, which involves the transfer of polarization from abundant nuclei (usually ^{1}H nuclei), by matching the B_1 r.f. field of the ^{1}H to that of the ^{13}C. The process of CP occurs through the transfer tendency of the magnetization from highly polarized nuclei to nuclei with lower polarizations when they are brought into contact, which is similar to heat flow from a hot object to a cold object when the two objects are in thermal contact. For homonuclear spins, the magnetization can be exchanged through mutual energy-conserving spin flips (see Fig. 3.6b). For heteronuclear pairs, such as ^{13}C and ^{1}H, these spin flips are not energy-conserving at high fields (see Fig. 3.6a). Therefore, the exchange of magnetization must be driven externally by the application of r.f. fields.

Among the technique for building a dipolar contact between two different spin systems *I* and *S*, the Hartmann-Hahn approach is particularly effective. This approach requires the simultaneous application of two continuous r.f. fields, one at the resonance frequency of the spin *I* and the other at the resonance frequency of the *S* spin. The effect of any r.f. field is to rotate the magnetization about the axis of the applied field. The rotation rate depends on the frequency and amplitude of the r.f. field. A r.f. field that oscillates at the spin *I* frequency, for instance 300 MHz, would not have essential effect on *S* spins with a frequency of 75 MHz and vice versa. By applying two r.f. fields, one tuned to the spin *I* the other to the spin *S*, both the *I* and *S* spins can be rotated independently around a particular axis at rates determined by the amplitudes of the two applied fields. When the nutation frequencies of the *I* and *S* spins are equal, i.e. the Hartman-Hahn condition is satisfied, given by [171]

$$\gamma_I B_{1(I)} = \gamma_S B_{1(S)} \tag{3.101}$$

an energy-conversing dipolar contact between the two spin systems is created. The maximum enhancement for a CP contact period is γ_I / γ_S. It is through this dipolar contact that the polarization is transferred between the *I* and *S* spins.

3.4.6 Spin-lattice relaxation times ($T_{1\rho(H)}$, $T_{1\rho(C)}$ and $T_{1(C)}$)

For an ensemble of isolated two-spin systems of the *IS* (heteronuclear, such as ^{13}C-^{1}H) type, the relaxation mechanisms can often be attributed to fluctuating dipolar interaction in samples, thus the general expressions for the spin lattice relaxation times can be written as [172]

$$\frac{1}{T_{1\rho\, d(IS)}} = \frac{d_{IS}^2}{40}\Big[4J_0(\omega_{1,S}) + J_4(\omega_I - \omega_S) + 3J_5(\omega_S) + 6J_6(\omega_I) + 6J_7(\omega_I + \omega_S)\Big] \tag{3.102}$$

$$\frac{1}{T_{1\, d(IS)}} = \frac{d_{IS}^2}{20}\Big[J_4(\omega_I - \omega_S) + 3J_5(\omega_S) + 6J_7(\omega_I + \omega_S)\Big] \tag{3.103}$$

where $T_{1\rho\ d(IS)}$ and $T_{1\ d(IS)}$ are the spin-lattice relaxation times in the rotating and laboratory frames, respectively. These functions have a minimum near $\omega\tau_c = 1$ (see Fig. 3.21a), indicating that motions with frequencies close to the Larmor frequency are the most effective in causing relaxation, where τ_c is a characteristic of the decay know as the correlation time for the particular motion involved. The spectral density functions, $J_m^D(\omega)$, appearing in Eqs. (3.102) and (3.103), are Fourier transforms of time correlation functions describing the molecular motion, defined as [152]

$$J_m^D(\omega) = \int_0^\infty C_m^D(\tau) e^{-i\omega t} d\tau \tag{3.104}$$

If a single-exponential correlation function is assumed for C_m^D, as [172]

$$C_m^D(\tau) = e^{-|\tau|/\tau_c} \tag{3.105}$$

by substituting Eq. (3.105) into (3.104), and expressing the integration explicitly, it yields

$$J_m^D(\omega) = \frac{2\tau_c}{1 + \omega^2\tau_c^2} \tag{3.106}$$

The full form of $J(\omega)$ (Eq. (3.106)) predicts a minimum in T_1 as a function of τ_c (see

Fig. 3.21a). The T_1 minimum occurs when the sudden drop in $J(\omega)$ as a function of ω (see Fig. 3.21b) corresponds to the resonance frequency, i.e. when $\tau_c = \omega_0^{-1}$. The sudden drop occurs when $\omega^2\tau_c^2 = 1$, known as the extreme narrowing condition. The T_1 minimum divides the motion into two regimes. In the right side of the minimum, the T_1 value decreases as the correlation time τ_c decreases and the motion is in the slow motional regime; when τ_c decreases sufficiently so that it is of the order of ω_0^{-1}, a new regime is entered, i.e. the extreme narrow regime, and the spin-lattice relaxation time T_1 increases with the decrease of τ_c.

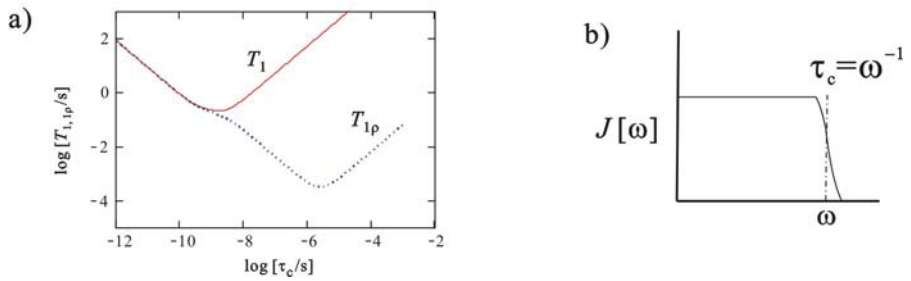

Figure 3.21 a) The dependence of ^{13}C T_1 and $T_{1\rho}$ on the correlation time τ_c, b) the relationship between the spectral density and the frequency.

Equations. (3.102) and (3.103) can be rewritten, respectively, as

$$\frac{1}{T_{1\rho\, d(IS)}} = \frac{d_{IS}^2}{20}\cdot\tau_c\cdot\left[\frac{4}{1+\omega_1^2\tau_c^2}+\frac{1}{1+(\omega_I-\omega_S)^2\tau_c^2}+\frac{3}{1+\omega_S^2\tau_c^2}+\frac{6}{1+\omega_I^2\tau_c^2}+\frac{6}{1+(\omega_I+\omega_S)^2\tau_c^2}\right] \tag{3.107}$$

$$\frac{1}{T_{1\, d(IS)}} = \frac{d_{IS}^2}{10}\cdot\tau_c\cdot\left[\frac{1}{1+(\omega_I-\omega_S)^2\tau_c^2}+\frac{3}{1+\omega_S^2\tau_c^2}+\frac{6}{1+(\omega_I+\omega_S)^2\tau_c^2}\right] \tag{3.108}$$

For homonuclear two-spin dipolar interactions (such as ^1H-^1H), the corresponding equations to those quantities are

$$\frac{1}{T_{1\rho\, d(II)}} = \frac{3d_{II}^2}{40}\left[5J_1(\omega_0) + 2J_2(2\omega_0) + 3J_3(2\omega_{1,I})\right] \tag{3.109}$$

$$\frac{1}{T_{1\rho\, d(II)}} = \frac{3d_{II}^2}{20}\cdot\tau_c\cdot\left[\frac{5}{1+\omega_0{}^2\tau_c^2} + \frac{2}{1+4\omega_0^2\tau_c^2} + \frac{3}{1+4\omega_{1,I}^2\tau_c^2}\right] \tag{3.110}$$

For most molecules there are many spin-pairs to consider, and the above equations must be modified by summing over all relevant interactions with respect to the spin under consideration.

If the fluctuation of the local field is caused by the chemical shift interaction, the general expressions of chemical shift relaxation can be derived in a similar way as those relevant to the dipolar-dipolar relaxation mechanism [124].

^{13}C relaxation times can provide significant information in chemistry. Interpretation of ^{13}C relaxation data in terms of molecular dynamics (e.g. internal and overall molecular motions) provides a unique and powerful probe into the detailed structure of organic molecular systems, and provides plenty of motional data, which are used to test models for the micro-dynamic behaviour of molecular systems.

The ^{13}C nucleus is particularly well suited for studies on spin relaxation. Carbon atoms are usually found at the backbone of molecules, interpretation of ^{13}C relaxation behaviour is generally not complicated by intermolecular relaxation processes, unlike the situation for ^{1}H and ^{19}F nuclei. ^{13}C spectra are primarily observed under proton-decoupled conditions, where each carbon in the molecule is represented by a single spectral line whose spin-lattice (T_1) and spin-spin (T_2) relaxation times can be governed by single exponential time constants. The rather large chemical shift range of the ^{13}C nucleus makes it possible to resolve virtually all individual carbons, even in complex molecules. Thus, multiple sites are often available at which to probe a

molecule's overall and internal motions. Since ^{13}C is a rare spin (low natural abundance), consideration of ^{13}C–^{13}C dipolar interactions or of the spin diffusion phenomenon is usually not necessary. This greatly simplifies the interpretation of ^{13}C relaxation rates.

Chapter 4 Experimental Section

4.1 Sample preparation

All chemicals for the chemical synthesis were obtained from Aldrich Chemicals, and were used without further purification.

4.1.1 Selectively deuterated guest molecules and urea molecules

Five kinds of selectively deuterated guest molecules: 1,10-dibromodecane-1,1,10,10-d_4, 1,11-dibromoundecane-1,1,11,11-d_4, two deuterated dibromohexanes 1,6-dibromohexane-1,1,6,6-d_4 (α-position) and 1,6-dibromohexane-2,2,5,5-d_4 (β-position), and 1-bromodecane-1,1-d_2, were used in the experiments, which were prepared with the following procedures:

(i) 1,10-dibromodecane-1,1,10,10-d_4 Decanedioic acid diethyl ester ($H_5C_2OOCC_8H_{16}COOC_2H_5$) was reduced with $LiAlD_4$ using standard procedures. By reaction with sodium bromide in aqueous solution of sulphuric acid the obtained decanediol-1,1,10,10-d_4 was transformed into its bromide. The product 1,10-dibromodecane-1,1,10,10-d_4 was purified by distillation [173].

(ii) 1,11-dibromoundecane-1,1,11,11-d_4 The preparation procedure is similar to that of 1,10-dibromoundecane-1,1,10,10-d_4 except that undecanedioic acid diethyl ester ($H_5C_2OOCC_9H_{18}COOC_2H_5$) was used as starting material.

(iii) 1,6-dibromohexane-1,1,6,6,-d_4 Hexanedioic acid dimethylester ($H_3COOCC_4H_8COOCH_3$) was reduced with $LiAlD_4$ using standard procedures. The resulting hexanediol-1,1,6,6-d_4 was transformed into its bromide by reaction with

sodium bromide in aqueous solution of sulphuric acid. The product 1,6-dibromo-hexane-1,1,6,6-d_4 was purified by distillation [173].

(vi) 1,6-dibromohexane-2,2,5,5-d_4 H/D exchange in the α-position of hexanedioic acid dimethylester was done by using sodium in methanol-d_1 [174]. The resulting selectively deuterated diester was reduced by lithium aluminium hydride to give 1,6-hexanediol-2,2,5,5-d_4. The final product, 1,6-dibromohexane-2,2,5,5-d_4, was obtained by reaction with sodium bromide in aqueous solution of sulphuric acid, followed by purification via distillation [173].

(v) 1-bromodecane-1,1-d_2 Ethyl decanoate ($CH_3(CH_2)_8COOC_2H_5$) was reduced with $LiAlD_4$ using standard procedures. By reaction with sodium bromide the obtained decanol-1,1-d_2 was transformed in aqueous solution of sulphuric acid to its bromide by the exchange reaction. The product 1-bromodecane-1,1-d_2 was purified by distillation.

(iv) Urea-d_4 Urea-d_4 was prepared by slowly cooling a warm solution of urea in methanol-d_1 (the molar ratio of urea to methanol-d_1 = 1:4), followed by filtration of the solution and drying of the product. This procedure was repeated once to ensure an almost complete exchange of the urea protons by deuterons.

4.1.2 Preparation of urea inclusion compounds

The urea inclusion compounds were prepared by slowly cooling warm solutions of the guest molecules 1,10-dibromodecane, 1,11-dibromoundecane, 1,6-dibromohexane, 1-bromodecane, n-decane, n-pentadecane, n-hexadecane, 1-fluorodecane, decanoic acid, dodecanedioic acid, sebacic acid with urea or urea-d_4 in methanol or methanol-d_1, respectively. The white needles or plates were filtered, washed with 2,2,4-trimethylpentane, and dried.

4.2 Methods

4.2.1 DSC (differential scanning calorimeter) measurement

Calorimetric studies were performed with a differential scanning calorimeter Netzsch DSC 204 (Selb/Germany) under nitrogen flow at heating rates of 10°C/min.

4.2.2 High resolution solid state ^{1}H MAS and ^{13}C CP MAS NMR measurement

^{13}C CP/MAS and ^{1}H MAS NMR experiments were performed on Bruker CXP 300 (Rheinstetten/Germany) and Varian InfinityPlus 400 (Palo Alto/USA) spectrometers operating at static magnetic fields of 7.04 and 9.39 T, respectively. The resonance frequencies were 75.47 (^{13}C), 300.13 MHz (^{1}H) for the CXP 300 spectrometer, and 100.52 (^{13}C), 399.75 MHz (^{1}H) for the InfinityPlus 400 spectrometer. A double tuned Bruker 4 mm MAS probe was used for the ^{13}C CP/MAS, T_1 (^{13}C), $T_{1\rho}$ (^{13}C), and $T_{1\rho}$ (^{1}H) experiments. $\pi/2$ pulse lengths were 4 μs. Contact times varied between 300 μs and 8 ms, as indicated in the text, and recycle delays of 6 s were used between successive scans. A sample rotation frequency of 5 kHz was used, and the number of scans was between 512 and 1024. ^{13}C T_1 data were obtained with cross-polarization (CP) excitation as proposed by Torchia et al [165]. Standard spin-lock pulse sequences were used for the determination of ^{13}C and ^{1}H $T_{1\rho}$ relaxation times [163, 164].

^{1}H MAS spectra were measured with a Bruker CXP 2.5 mm double resonance MAS probe (at 300.13 MHz) with a $\pi/2$ pulse length of 4 μs and a Varian 4 mm triple resonance MAS probe (at 399.75 MHz) with a $\pi/2$ pulse length of 3.5 μs. Typically, 32 or 64 scans were accumulated with recycle delays of 2 s or 4 s. ^{13}C chemical shifts were referenced to the external standard adamantane. This value was then expressed relative to TMS (δ = 0 ppm). Likewise, ^{1}H chemical shift values are given relative to TMS (δ = 0 ppm).

4.2.3 ^{2}H NMR measurement

All ^{2}H NMR experiments were performed at 46.07 MHz on a Bruker CXP 300 spectrometer interfaced to a Tecmag spectrometer control system. The quadrupolar echo sequence $(\pi/2)_x$-τ_e-$(\pi/2)_y$-τ_e with $\pi/2$ pulses of 2.0 μs and a pulse spacing of τ_e = 20 μs was used to obtain the experimental ^{2}H NMR spectra. Spin-spin relaxation times (T_2) were determined with the same pulse sequence by the variation of τ_e.

A modified inversion recovery sequence, π-τ_r-$(\pi/2)_x$-Δ-$(\pi/2)_y$-Δ, combined with the quadrupolar echo sequence for signal detection and variable relaxation intervals τ_r, was employed for the determination of T_{1Z} (relaxation time for Zeeman order). Here, instead of the inversion π pulse, a composite pulse, given by $[\pi/2]_\phi[\pi/2]_{\phi\pm\pi/2}[\pi/2]_\phi$, with appropriate phase cycling (ϕ = 0, $\pi/2$, π and $3\pi/2$) [136] was used. Recycle delays were set to be at least five times the spin-lattice relaxation time T_{1Z}. Relaxation times for quadrupolar order, T_{1Q}, were measured applying the broadband Jeener-Broekaert sequence (BBJB) ($90°_x$-$2\tau_w$-$67.5°_{-y}$-$2\tau_w$-$45°_y$-τ_w-$45°_y$-τ_r-$45°_y$-Δ-$90°_y$) [137]. Here, ($90°_x$-$2\tau_w$-$67.5°_{-y}$-$2\tau_w$-$45°_y$-τ_w-$45°_y$) represents the excitation sequence, whose phase cycle maximizes quadrupolar order while fully suppressing Zeeman order [138]. A refocusing pulse was used to generate an echo, resulting in partially relaxed spectra with minimal baseline distortion and no first-order phase corrections.

During the ^{2}H NMR studies, the number of scans varied between 512 and 1300 depending on the signal/noise ratio. The sample temperature was controlled by a Bruker BVT 2000 unit. The samples were initially held at each new temperature for at least fifteen minutes to allow full equilibration. In general, the accuracy of temperature was found to be within ± 1 K.

4.3 ^{2}H NMR simulation

Data processing of the experimental (from the CXP 300 NMR spectrometer) and theoretical ^{2}H NMR signals were done on a SUN workstation by using NMR1 and Sybyl/Triad software packages (Tripos, St. Louis, MO). The data from ^{1}H MAS and ^{13}C CP/MAS NMR measurements were handled by utilizing the MestRec software [175].

The programs employed during the simulations of the corresponding line shape and relaxation experiments are very general, and consider various types of molecular motions of the systems under investigation [7, 44]. The theoretical line shapes and relaxation times were obtained by numerical diagonalization of the corresponding relaxation matrices by using standard software packages [44, 129].

For the line shape simulations, a slow-motional approach was used [128, 129]. This approach assumes δ-pulses, and explicitly accounts for the interval τ_e in the quadrupolar echo experiment, responsible for spin-spin relaxation. The theoretical description of the spin-lattice relaxation data (T_{1Z}, T_{1Q}) is based on the Redfield approach [150]. Here, partially relaxed spectra were obtained after multiplication of motionally averaged ^{2}H NMR spectra (fast exchange limit) with theoretical damping factors that account for orientation-dependent spin-lattice relaxation during the interval τ_r of the inversion recovery [128] and BBJB experiments [137].

Chapter 5 Results and Discussion

5.1 1,10-dibromodecane and 1,11-dibromoundecane/urea inclusion compounds

Variable temperature ^{2}H NMR spectroscopy was carried out between 100 K and room temperature on two urea inclusion compounds with non-deuterated urea. The guest compounds 1,10-dibromodecane and 1,11-dibromoundecane were selectively deuterated at both end groups (see Fig. 5.1). In addition, ^{1}H and ^{13}C solid-state NMR studies were performed for the inclusion systems of the non-deuterated guest species in urea or urea-d_4. Differential scanning calorimetry shows that the phase transition for 1,10-dibromodecane/urea occurs at 141 K (agreement with the data reported previously [23]) and for 1,11-dibromoundecane/urea at 167 K, which mainly reflects a structural change of the urea host lattice from orthorhombic to hexagonal symmetry [23, 85]. The phase transition temperatures of 133 K for 1-bromodecane/urea [176] and 111 K for decane/urea [85] imply a correlation between the number of bromine end groups and the solid-solid phase transition temperatures, most probably due to an increase of intermolecular interactions between guest and host as well as guest and guest species.

Figure 5.1 Chemical structure of 1,10-dibromodecane and 1,11-dibromoundecane selectively deuterated at the both ends.

5.1.1 ^{13}C CP/MAS and ^{1}H MAS NMR studies

Figure 5.2 displays ^{13}C CP/MAS NMR spectra of 1,10-dibromodecane and 1,11-dibromoundecane in urea or urea-d_4 which were recorded at room temperature. ^{13}C chemical shifts of the guest species in urea and in solution are listed in Table 5.1.

A pronounced downfield shift of the ^{13}C NMR signals is observed for the dibromoalkanes in urea. For n-alkanes [25] and branched n-alkanes [177] in urea, similar ^{13}C chemical shift alterations were understood in terms of changes in conformational state. Based on these observations and the results from ^{2}H NMR, Raman, IR and X-ray investigations [4-9, 25, 77, 177], it was concluded that n-alkanes in urea adopt a nearly all-trans conformational state while in solution a fast equilibrium is established between gauche and trans conformers. Similarly, the data for the UICs with 1,10-dibromodecane and 1,11-dibromoundecane can be interpreted. That is, 1,10-dibromodecane and 1,11-dibromoundecane in urea – unlike the situation in solution – exists in an almost all-trans conformation, in agreement with former studies [9].

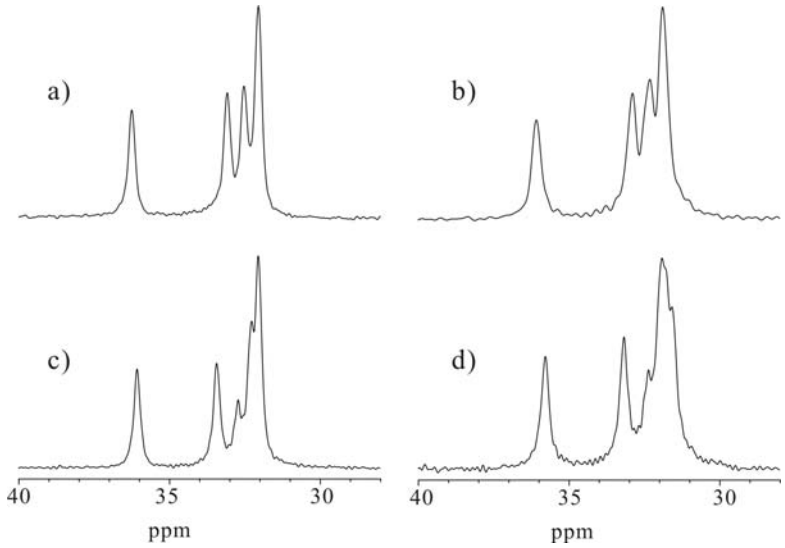

Figure 5.2 ^{13}C CP/MAS NMR spectra of (a) 1,10-dibromodecane/urea, (b) 1,10-dibromodecane/urea-d_4, (c) 1,11-dibromoundecane/urea, (d) 1,11-dibromoundecane/urea-d_4.

The interaction between the urea host lattice and the guest species becomes obvious by comparing the ^{13}C NMR line widths in the UICs from urea and urea-d_4 (see Table 5.1). For the guest species in urea-d_4, larger line widths are observed than for the samples made from non-deuterated urea. ^{13}C NMR spectra of guest species in urea

and urea-d_4 are recorded only under the proton decoupling. When the ^{13}C spectrum of guest species in urea-d_4 is recorded ^{13}C-^{2}H dipolar couplings between the guest species and the host matrix exist as a result of the replacement of the protons by the deuterons, which leads to the increase of the ^{13}C NMR line widths for the guest species in urea-d_4. For the urea carbonyl group a smaller ^{13}C NMR line width upon urea deuteration is found, which reflects interference effects [178, 179] between the ^{1}H decoupling r.f. field and urea reorientational motions, i.e., 180° flips around the C=O double bond and around the C-N bond [39, 180]. This is further supported by the observation that an increase of the ^{1}H decoupler power gives rise to a broadening for the carbonyl ^{13}C NMR signal, as also established recently for other UICs [176].

The ^{13}C NMR signal intensity was recorded as a function of contact time for cross-polarization. It was found that the contact time with a maximum ^{13}C NMR signal varies considerably with the deuteration of the urea matrix. Thus for both guest molecules values of 2 and 8 ms were found in urea and urea-d_4, respectively. The longer contact time needed for the deuterated urea clathrates, in good agreement with the observation for other urea inclusion compounds [176], can be attributed to the loss of urea protons which obviously also contribute to the magnetization transfer to the guest carbons during cross-polarization.

^{1}H MAS NMR spectra for 1,10-dibromodecane and 1,11-dibromoundecane in urea and urea-d_4 were recorded at a spinning speed of 15 kHz, as shown in Figure 5.3. Both guest species in urea show a low resolution in the ^{1}H NMR spectra, which arises from strong spin diffusion of the protons. This strong ^{1}H spin diffusion is also the reason why all protons in the chain have approximate the same $T_{1\rho(H)}$ values (see Table 5.2 and 5.3). The lower resolution for 1,11-dibromoundecane in urea can be attributed to the increase of the chain length. Deuteration of the urea host lattice is accompanied by additional resolution enhancement for the ^{1}H NMR spectra of the guest species. This observation can be traced back to a suppression of ^{1}H spin

Table 5.1 NMR parameters from ^{13}C and ^{1}H NMR studies on 1,10-dibromodecane and 1,11-dibromoundecane in solution and UICs.

(a) $BrC_{10}H_{20}Br$

	δ_{13C} [ppm]			$\Delta\nu_{1/2\,(13C)}$[c]		δ_{1H} [ppm]		
	solution[a]	urea[b]	urea-d	urea	urea-d_4		solution	urea[e]
C-1	33.9	36.2	36.1	20.4	28.5	H (C-1)	3.4	3.5
C-2	32.8	33.1	32.9	22.7	36.5	H (C-2)	1.9	2.1
C-3,	28.7-28.	32.0	31.9	22.5	33.8	H (C-3)	1.5	1.5
C-5	29.3	32.5	32.3	31.8	39.6	H	1.3	1.5
C=O		164	163.7	91.6	51.9			

(b) $BrC_{11}H_{22}Br$

	δ_{13C} [ppm]			$\Delta\nu_{1/2\,(13C)}$[c]		δ_{1H} [ppm]		
	solution[a]	urea[b]	urea-d	urea	urea-d_4		solution	urea[e]
C-1	33.9	36.1	35.8	19.0	25.5	H (C-1)	3.4	3.5
C-2	32.8	33.4	33.2	20.6	27.1	H (C-2)	1.8	2.1
C-3,	28.7-28.2	32.1	31.6	28.1	21.1	H (C-3)	1.4	1.5
C-5	29.4	32.3	31.9	21.2	41.0	H	1.3	1.5
C-6	29.4	32.7	32.4	27.9	29.2			
C=O		164	163	93.8	45.8			

[a] ^{13}C chemical shifts of 1,10-dibromodecane, 1,11-dibromoundecane in $CDCl_3$ [181].

[b] ^{13}C chemical shifts of 1,10-dibromodecane and 1,11-dibromoundecane in their UICs derived in this work from ^{13}C CP/MAS studies.

[c] ^{13}C NMR line width

[d] ^{1}H chemical shifts of 1,10-dibromodecane and 1,11-dibromoundecane in $CDCl_3$ [181].

[e] ^{1}H chemical shifts of 1,10-dibromodecane and 1,11-dibromoundecane in their UICs derived in this work from ^{1}H MAS experiments.

diffusion since the guest molecules are isolated from each other upon enclathration

(reduced intermolecular dipolar interactions between guests), and the large ^{1}H spin reservoir from the non-deuterated urea molecules is missing. Comparison of the derived ^{1}H chemical shift values again reveals slightly downfield shifts upon enclathration for both samples with 1,10-dibromodecane and 1,11-dibromoundecane which again, are attributed to changes in conformational order.

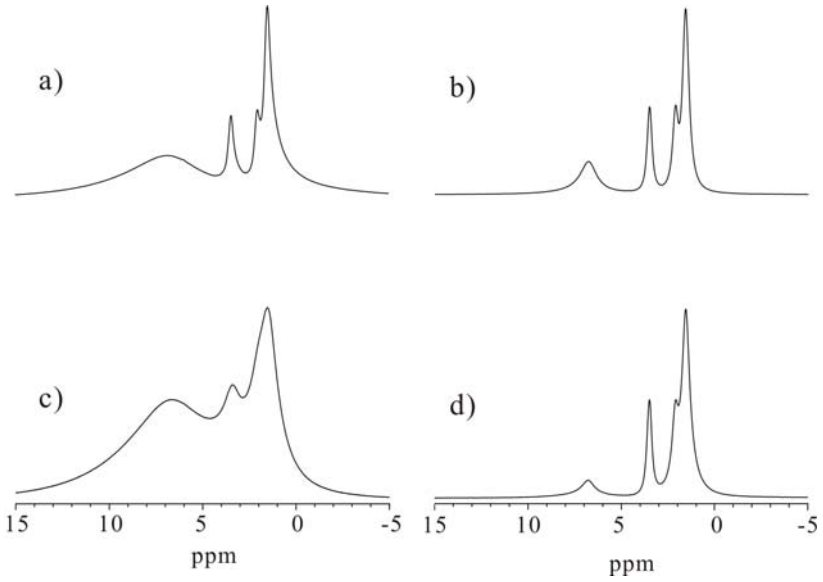

Figure 5.3 ^{1}H MAS NMR spectra of (a) 1,10-dibromodecane/urea, (b) 1,10-dibromodecane/urea-d_4 (c) 1,11-dibromoundecane/urea, (d) 1,11-dibromoundecane/urea-d_4 at a spin rate of 15 kHz.

^{13}C $T_{1\rho}$, ^{13}C T_1 and ^{1}H $T_{1\rho}$ measurements can provide information about the dynamics of the guest components. The derived data are summarized in Tables 5.2 and 5.3. For 1,10-dibromodecane/urea it is found that urea deuteration results in distinctly larger ^{13}C $T_{1\rho}$ and ^{1}H $T_{1\rho}$ values which reflect reduced effective hetero- and homonuclear dipolar interactions between guest and host components. From the variable temperature ^{13}C $T_{1\rho}$ data it can be concluded that the underlying motions are on the low temperature side of the $T_{1\rho}$ relaxation curve. As will be discussed below, transitional motion might explain the ^{13}C $T_{1\rho}$ data, which is sensitive to variations of

the distance, position and interaction between the guest and the host. This motion has been reported previously in IQNS experiments on 1,10-dibromodecane/urea-d_4 [27] and is also observed indirectly in ^{2}H NMR studies (see below). The ^{13}C T_1 values are much longer than the ^{13}C $T_{1\rho}$ values and almost unaffected by urea deuteration. Obviously, there is no efficient process present which affects ^{13}C T_1 relaxation.

Table 5.2 $T_{1\rho(C)}$ and $T_{1\rho(H)}$ data for the $BrC_{10}H_{20}Br$ in urea and urea-d_4.

$BrC_{10}H_{20}Br$-urea	$T_{1\rho(13C)}$ [ms]				$T_{1\rho(1H)}$	$T_{1(13C)}$
(CT[a]: 2ms)	294K	300K	310K	320K	[ms][b]	[s][b]
C-1	320	310	228	167	4.3	7.7
C-2	276	266	226	171	4.3	8.3
C-3,4	282	270	210	178	4.3	8.4
C-5	304	290	224	177	4.3	6.5
$BrC_{10}H_{20}Br$-urea-d_4	$T_{1\rho(13C)}$ [ms]				$T_{1\rho(1H)}$	$T_{1(13C)}$
(CT: 8ms)	294K	300K	310K	320K	[ms]	[s]
C-1	458	337	302	241	29	8.9
C-2	465	437	364	322	30	8.0
C-3,4	452	406	336	322	30	8.5
C-5	598	482	378	308	28	8.4

[a] contact time

[b] value at 294 K

1,11-dibromoundecane/urea behaves similar to 1,10-dibromodecane/urea. The differences are i) the ^{13}C $T_{1\rho}$, ^{13}C T_1 values of 1,11-dibromoundecane/urea are greater than the counterparts of 1,10-dibromodecane/urea, ii) the ^{13}C $T_{1\rho}$ values of 1,11-dibromoundecane/urea exhibit a minimum at 310 K (the ^{13}C $T_{1\rho}$ data of 1,11-dibromoundecane/urea-d_4 are not given because it turned out that they are too long to get accurate values), and iii) ^{13}C T_1 values become slightly larger by urea deuteration. Similarly, for 1,11-dibromoundecane/urea transitional guest motion

might dominate ^{13}C $T_{1\rho}$ relaxation and no efficient relaxation process contributes to ^{13}C T_1 relaxation.

Table 5.3 $T_{1\rho(13C)}$ and $T_{1\rho(1H)}$ data for the $BrC_{11}H_{22}Br$ in urea and urea-d_4.

$BrC_{11}H_{22}Br$-urea (CT[a]: 2ms)	$T_{1\rho(13C)}$ [ms][b]				$T_{1\rho(1H)}$ [ms][c]		$T_{1(13C)}$ [s][c]	
	294K	300K	310K	320K	urea	urea-d_4	urea	urea-d_4
C-1	478	450	378	432	3.5	50	7.2	9.5
C-2	450	441	438	469	3.3	51	8.5	13
C-3,4	479	413	338	387	3.6	45	6.4	11
C-5	478	412	454	610	3.5	49	8.1	11
C-6	500	407	484	606	3.7	44	8.1	8.4

[a] contact time, (CT[a]: 8ms for $BrC_{11}H_{22}Br$ in urea-d_4)

[b] values for $BrC_{11}H_{22}Br$ in urea

[c] value at 294 K

5.1.2 ^{2}H NMR line shapes and spin-spin relaxation data

^{2}H NMR line shapes derived from the samples 1,10-dibromodecane-d_4/urea and 1,11-dibromoundecane-d_4/urea are shown in Figures 5.4 and 5.5, respectively. ^{2}H NMR spectra of both samples were recorded between 100 K and room temperature. The spectrum at 100 K in Figure 5.4 is a typical powder pattern for static deuterons. The experimental splitting between the perpendicular singularities of the spectrum is 124 kHz, which remains constant up to 120 K. The spectrum recorded at room temperature in Figure 5.4 is also a powder pattern with a frequency separation of 46 kHz between the perpendicular singularities. Between these two extreme temperatures, characteristic ^{2}H NMR line shape changes are registered. However, no pronounced discontinuity is observed at the phase transition.

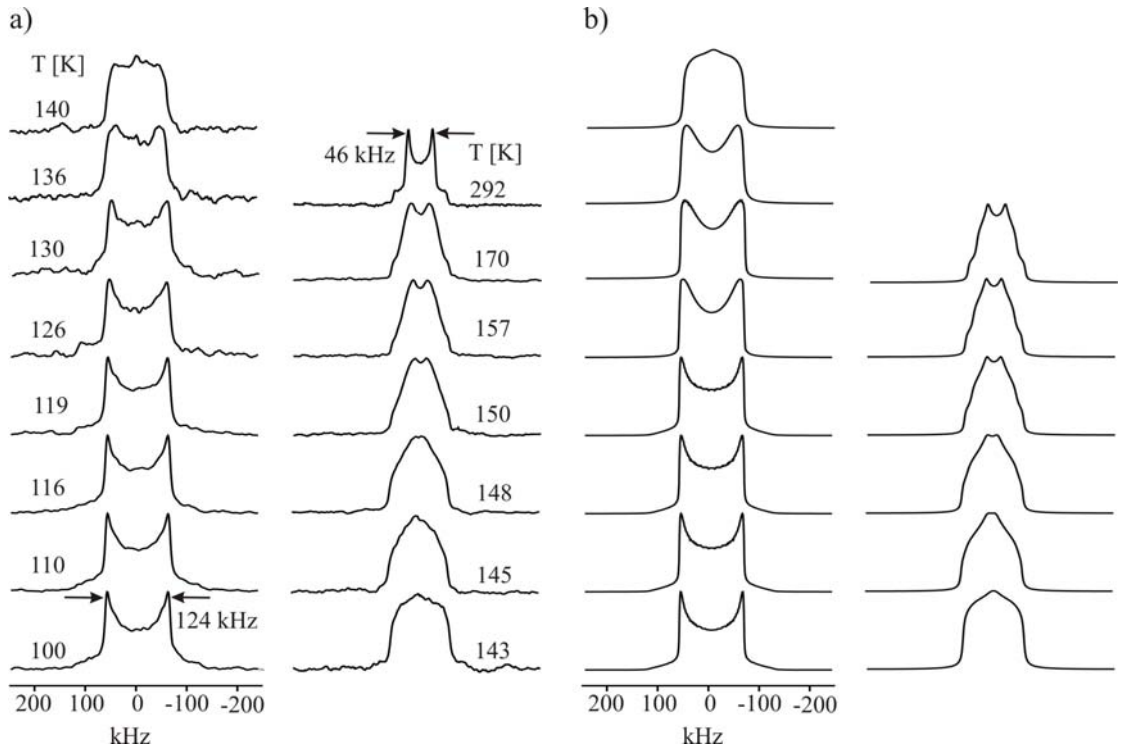

Figure 5.4 ^{2}H NMR line shapes as a function of temperature for 1,10-dibromodecane/urea (a: experiment, b: simulation).

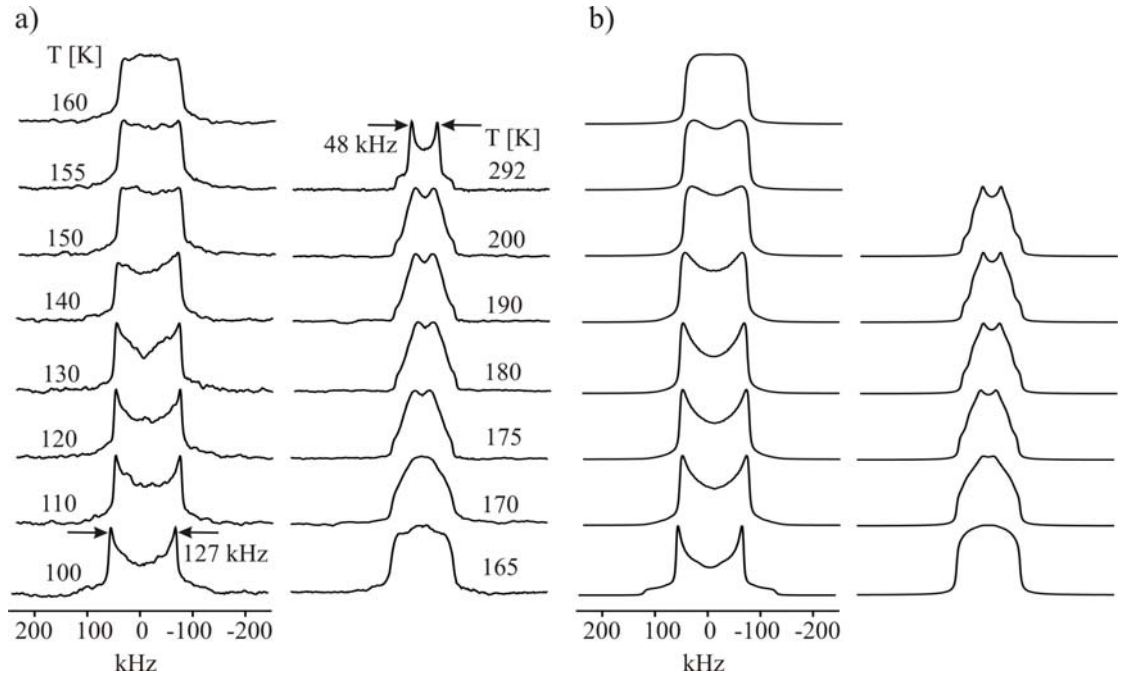

Figure 5.5 ^{2}H NMR line shapes as a function of temperature for 1,11-dibromoundecane/urea (a: experiment, b: simulation).

^{2}H NMR line shapes are illustrated in Figure 5.5 for the sample 1,11-dibromo-undecane-d_4/urea. It is found that the overall spectral changes are similar to those of 1,10-dibromodecane-d_4/urea at elevated temperature. However, there is a temperature shift of about 26 K between the ^{2}H NMR spectra of similar overall appearance. Moreover, the spectra for 1,11-dibromoundecane-d_4/urea have a somewhat larger experimental splitting than the counterparts of 1,10-dibromo- decane-d_4/urea, i.e., 127 kHz for temperatures from 100 K to 120 K and 48 kHz at room temperature.

To account for the dynamic properties of the guest molecules, various types of motional models were examined. Numerous theoretical simulations have shown that the observed changes in the ^{2}H NMR line shapes for 1,10-dibromodecane-d_4/urea and 1,11-dibromoundecane-d_4/urea at best can be understood by assuming a superposition of two dynamic processes: an overall molecular wobbling motion and a non-degenerate jump model, for which a simple 3-site process was found to be appropriate. For such a process, the geometry of the jump process is characterized by the angle θ between the rotation axis and the C-D bond direction, and by the azimuthal angles $\pm\Delta\psi$ away from site 1, which is located at the potential minimum (see Figure 5.6). An all trans conformation in the systems is assumed, the angle θ is thus taken as 90° and $\Delta\psi = 120°$. The fractional populations denoted p_2, p_3 for both sites are identical and in

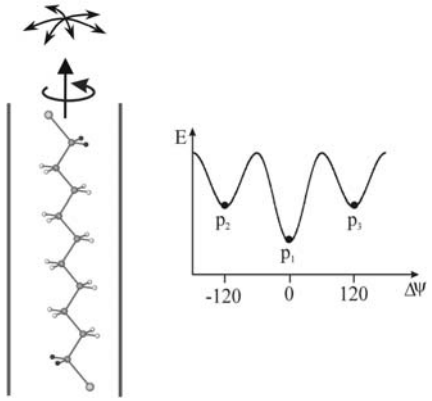

Figure 5.6 Possible motions of guest molecules in urea and potential energy curve of a 3-site jump motion.

general are different from the population denoted by p_1 of the unique site 1 which has a minimum energy, i.e., $p_2 = p_3 \neq p_1$, and the summation of the populations of all the three sites is unity ($p_1 + p_2 + p_3 = 1$). It should be mentioned that on the basis of the urea channel symmetry a 6-site jump model is more appropriate. However, since 3- and 6-site models cannot be distinguished, we describe the results in the framework of the 3-site jump model.

Experimental ^{2}H NMR spectra covering the low- and high-temperature range along with their best simulations are depicted in Figure 5.4 for 1,10-dibromodecane-d_4/urea and Figure 5.5 for 1,11-dibromoundecane-d_4/urea. The spectra recorded at 100 K can be fitted well with the assumption of static C-D bonds with a static quadrupole coupling constant of 170 kHz and an asymmetry parameter $\eta = 0$. The observed characteristics in the ^{2}H NMR line shapes for 1,10-dibromodecane-d_4/urea and 1,11-dibromoundecane-d_4/urea are both reproduced well by the simulations based on the 3-site jump model described above. Moreover, the quadrupole coupling constant was reduced at elevated temperatures in order to get a good reproduction of the experimental spectra. This can be interpreted by the presence of an additional fast motional contribution, besides the rotation about the long channel axis. The molecule is assumed to undergo a fast small-angle wobbling process perpendicular to the channel long axis, along an arc defined by the half angle θ_0. The quadrupole coupling constant in the ^{2}H NMR spectra is therefore replaced by the scaled value, i.e. motionally effective quadrupole coupling constant, averaged by the high-frequency overall wobbling process.

The experimental spin-spin relaxation data for 1,10-dibromodecane-d_4/urea and 1,11-dibromoundecane-d_4/urea are given in Figure 5.7. The experimental T_2 values of 1,10-dibromodecane-d_4/urea at first decrease with increasing temperature, then gradually rise. The minimum value of 47 μs is registered at 129 K, which marks the temperature at which the rate constant of some molecular motions matches the size of

the quadrupolar interaction. In contrast, the experimental T_2 data for 1,11-dibromo-undecane-d_4/urea exhibit a monotonous increase with temperature increase.

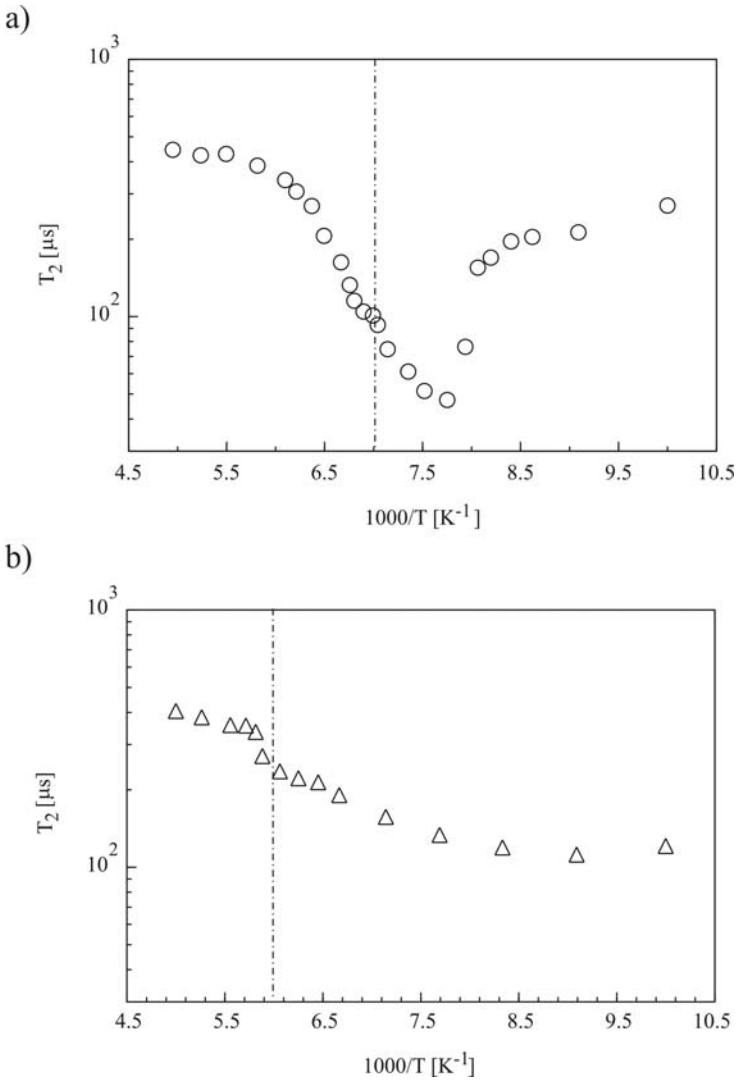

Figure 5.7 Experimental ^2H spin-spin relaxation times as a function of temperature for (a) 1,10-dibromodecane and (b) 1,11-dibromoundecane in urea (dashed line denotes solid-solid phase transition).

The aforementioned motional model (superposition of the 3-site jump and the overall chain wobbling) is also able to describe the dependence of lineshapes from quadrupole echo experiments on the pulse spacing which reflects the angular

dependence of T_2. The partially relaxed ^2H NMR spectra (quadrupole echo experiment) within the low temperature range have been analyzed with the same parameters as used in the simulation of the variable temperature ^2H NMR line shapes, including the quadrupole coupling constant, populations and correlation times. Representative examples are given in figures 5.8 and 5.9. The experimental partially relaxed spectra are well reproduced by their theoretical counterparts, which supports the suitability of the assumed model.

Please note that during the simulations of the ^2H NMR line shapes and partially relaxed spectra from quadrupole echo experiment, the line broadening is varied (see in Table 5.4 and 5.5), i.e., the residual $1/T_2^0$ value is reduced with the increasing temperature.

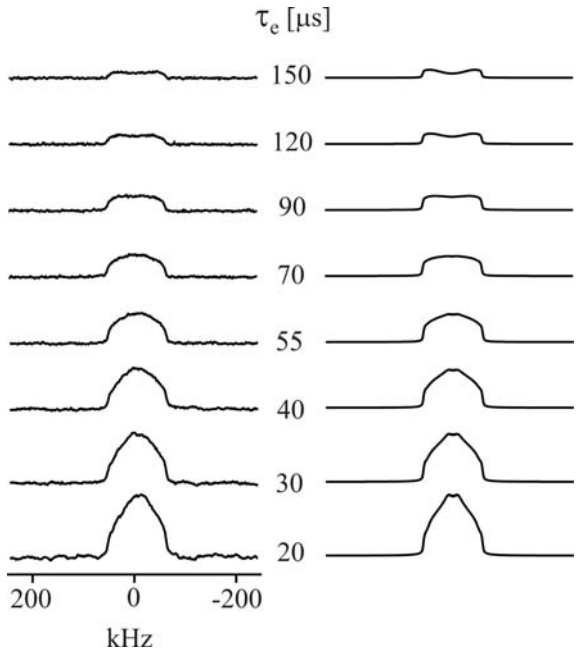

Figure 5.8 Experimental (left) and theoretical (right) partially relaxed ^2H NMR spectra from quadrupole echo experiment with $\tau_c = 1.5 \times 10^{-7}$s at 148 K for 1,10-dibromodecane in urea.

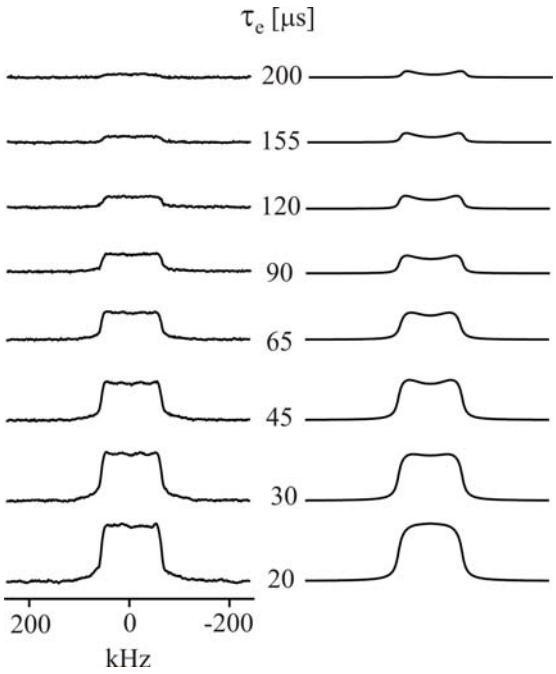

Figure 5.9 Experimental (left) and theoretical (right) partially relaxed ^{2}H NMR spectra from quadrupole echo experiment with $\tau_c = 3.5 \times 10^{-7}$ s at 160 K for 1,11-dibromoundecane in urea.

The derived correlation times of overall molecular jump motions in low temperature range from the simulations of the ^{2}H NMR line shape and partially relaxed quadrupole echo spectra are listed in Tables 5.4 and 5.5.

5.1.3 Spin-lattice relaxation data

Above the phase transition temperature, the molecular motions are too fast to affect the ^{2}H NMR line shapes and spin-spin relaxation data. Here, the analysis of spin-lattice relaxation data provides further information about the rate constants and kinetic parameters. In fact, both the spin-lattice relaxation times and the partially relaxed spectra from the inversion recovery experiments, which reflect the T_{1Z} anisotropy, have been analyzed.

In Figure 5.10 the spin-lattice relaxation data are shown for samples 1,10-dibromo-decane-d_4/urea and 1,11-dibromoundecane-d_4/urea. Again, these data refer to the

overall values of the powder sample which have been derived from the amplitudes of the corresponding free induction decay as function of the pulse interval τ_r in the inversion recovery experiment. The experimental T_{1Z} relaxation curves for 1,10-dibromodecane-d_4/urea and 1,11-dibromoundecane-d_4/urea exhibit a similar shape. A minimum value of 20 ms is registered at 170 K for 1,10-dibromo- decane-d_4/urea and 18 ms at 175 K for 1,11-dibromoundecane-d_4/urea. Two different slopes above and below T_{1Z} minima at the T_{1Z} curves are quite obvious for both samples, which implies different molecular processes that contribute to spin-lattice relaxation in these regimes.

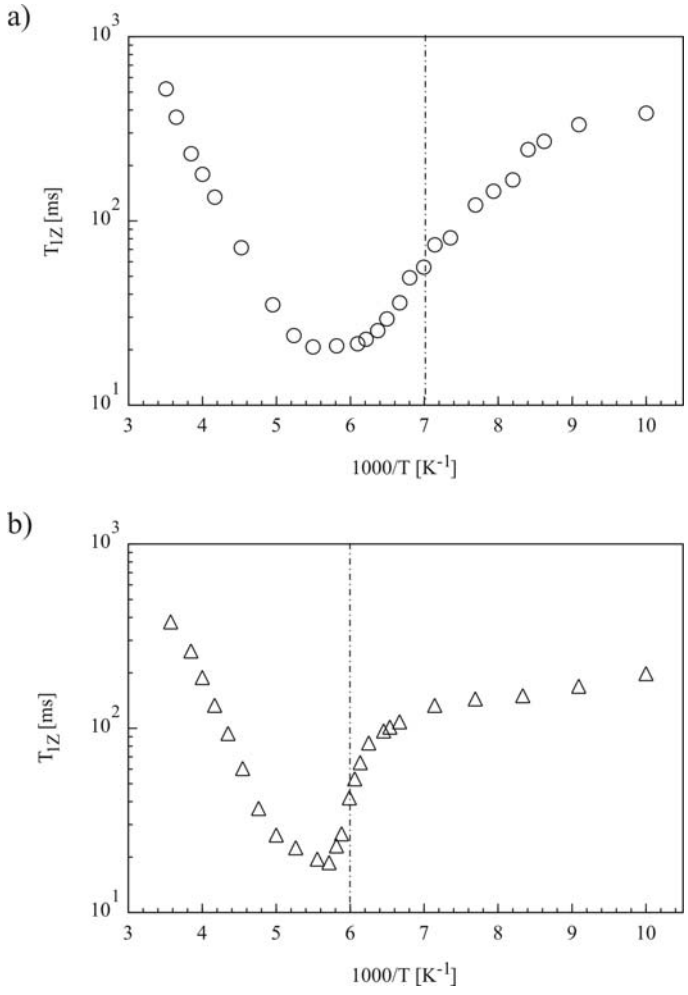

Figure 5.10 Experimental ^2H spin-lattice relaxation times as a function of temperature for (a) 1,10-dibromodecane and (b) 1,11-dibromoundecane in urea (dashed line denotes solid-solid phase transition).

In order to reproduce the experimental T_{1Z} data in the low temperature phase, the same parameters as in the aforementioned ^2H NMR line shapes and T_2 relaxation data analysis were used. That is, we used a non-degenerate 3-site jump process with the rate constants, quadrupole coupling constants and populations, as given in Tables 5.4 and 5.5. However, it turned out that all theoretical T_{1Z} values were higher than the experimental ones. This discrepancy was ascribed to the fact that an additional motion of the guest molecules, the overall wobbling process, was not explicitly considered to contribute to spin-lattice relaxation. Rather, it was only included in the reduced quadrupole coupling constant, mentioned in the previous paragraph.

We therefore assumed that T_{1Z} has two independent contributions

$$\frac{1}{T_{1Z,\,\mathrm{exp}}} = \frac{1}{T_{1Z,\,rot}} + \frac{1}{T_{1Z,\,\mathrm{wobb}}} \tag{5.1}$$

The first one is calculated with the 3-site jump as described above, and the second one is the difference between the experimental values and the theoretical values, based only on the 3-site jump process. In order to get correlation times for the wobbling contribution ($T_{1Z,\ \mathrm{wobb}}$), we used a degenerate 19-site wobbling model [162] and a static quadrupole coupling constant of 170 kHz. The opening angle was obtained by adjusting the theoretical spectrum (by using a degenerate 19-site model) to the experimental one, i.e., until the widths of both spectra were identical. These opening angles (see Tables 5.4 and 5.5) were thus used together with the static quadrupole coupling constant of 170 kHz to derive the corresponding correlation times with a suitable T_1 analysis program (19-site jump model) which are given in Tables 5.4 and 5.5.

In the high temperature phase, the analysis was different, since it turned out that both the absolute T_{1Z} values and the anisotropy, as reflected by the partially relaxed spectra in the inversion recovery experiments, can be reproduced very well with only the

3-site jump model. That is, in the high temperature phase the contribution of the overall wobbling process to T_{1Z} relaxation was too small and T_{1Z} relaxation was dominated by the overall rotational process. Representative theoretical and experimental partially relaxed spectra, given in Figures 5.11 and 5.12, demonstrate the quality of these model assumptions.

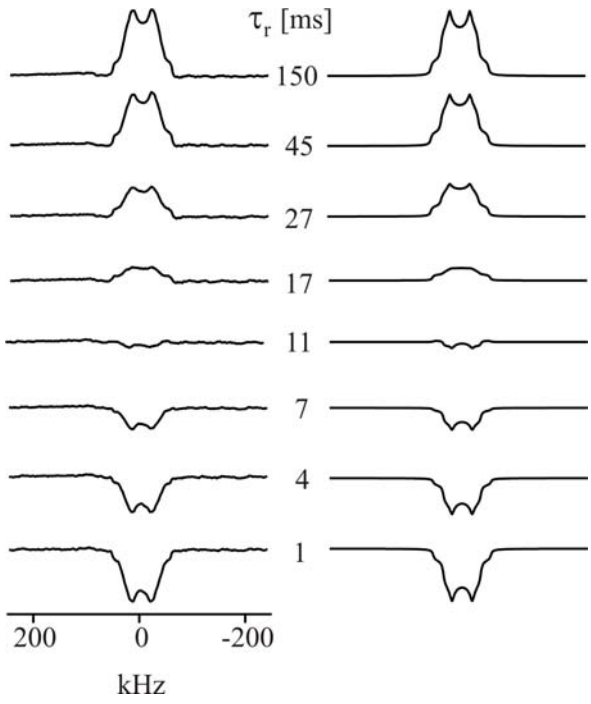

Figure 5.11 Experimental (left) and theoretical (right) partially relaxed ^{2}H NMR spectra with $\tau_c = 2.7 \times 10^{-10}$ s at 180 K for 1,10-dibromodecane in urea (inversion recovery sequence).

The correlation times derived from the T_{1Z} analysis are given in Tables 5.4 and 5.5. The rate constants k_{ij} are related to the correlation time by $\frac{1}{\tau_c} = \frac{k_{ij}}{p_i}$. Here, k_{ij} represents the pseudo first-order rate constant for the transition from site j to i with the population p_i. The derived rate constants are listed in Tables 5.4 and 5.5 as well, and are plotted in Fig. 5.13 as a function of the reciprocal temperature. From the Arrhenius representations in Fig. 5.13, activation energies $E_{a,\,12}$ of the 3-site jump

around the long axis of the urea channel, in the temperature range from 190 K to room temperature, are determined to be 13.1 kJ/mol for 1,10-dibromodecane-d_4/urea and 13.8 kJ/mol for 1,11-dibromoundecane-d_4/urea. The temperature range around the T_{1Z} minima is not included since we were not able to reproduce the experimental T_{1Z} values satisfactorily, i.e. the theoretical values were always lower than their experimental counterparts. Attempts were made to overcome this problem with other models, change of population and distributions of correlation times [182], but none of them provided satisfactorily results.

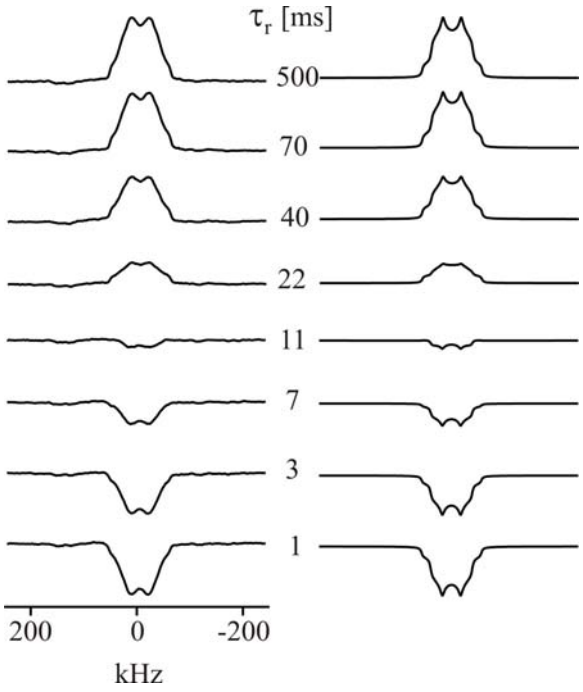

Figure 5.12 Experimental (left) and theoretical (right) partially relaxed ^{2}H NMR spectra with $\tau_c = 2.3 \times 10^{-10}$ s at 190 K for 1,11-dibromoundecane in urea (inversion recovery sequence).

As shown above, the T_{1Z} data analysis also provided rate constants in the low temperature range for 1,10-dibromodecane-d_4/urea and 1,11-dibromoundecane-d_4/urea by the assumption of a combined wobbling motion and 3-site jump motion (as mentioned above for the 3-site jump motion in the low temperature range the same values as for

the T_2 analysis were used). Activation energies $E_{a,\,12}$ of 4.6 kJ/mol for 1,10-dibromodecane-d_4/urea and 2.9 kJ/mol for 1,11-dibromoundecane-d_4/urea were derived for the 3-site jump motion in the low temperature range. From Figure 5.13 the activation energies, for the wobble motion, are found to be 6.7 kJ/mol for 1,10-dibromodecane-d_4/urea, and 3.1 kJ/mol for 1,11-dibromoundecane-d_4/urea (see Table 5.6).

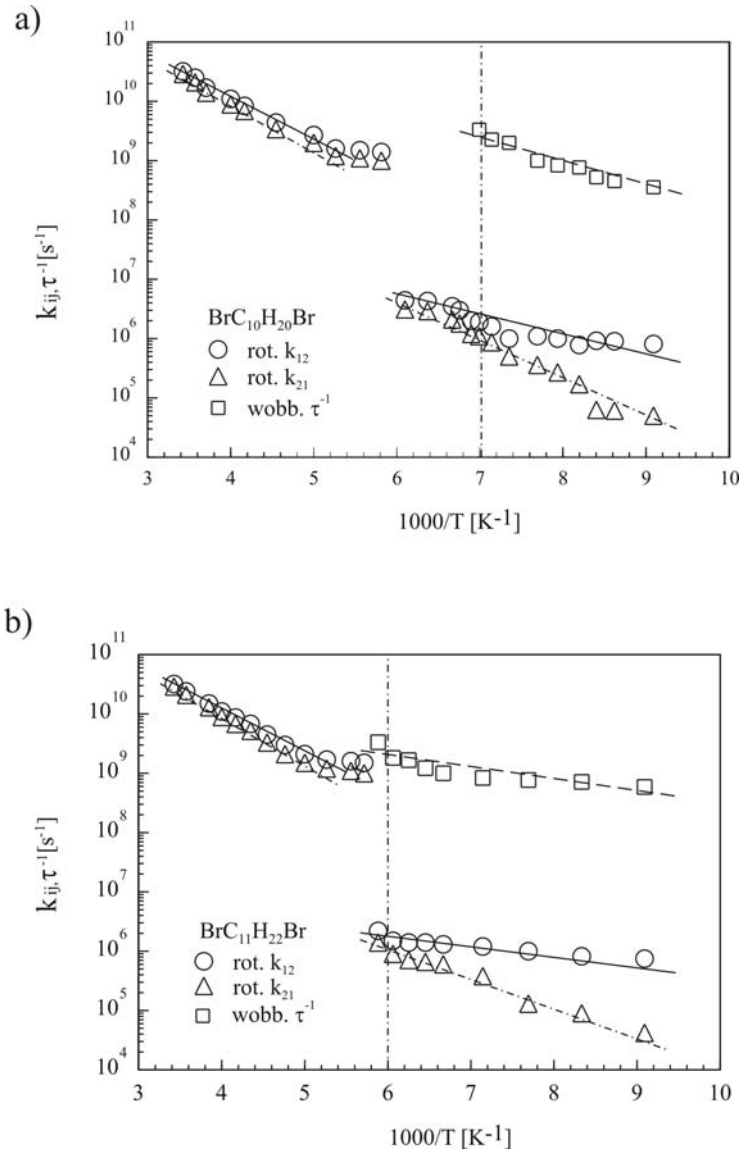

Figure 5.13 Arrhenius plots for the overall motions of (a) 1,10-dibromodecane and (b) 1,11-dibromoundecane in urea (perpendicular dashed line denotes solid-solid phase transition).

Table 5.4 Simulation parameters for 1,10-dibromodecane-1,1,10,10-d_4/urea.

temp. T [K]	Quadrupole[2] coup.const. e^2qQ/h^* [kHz]	correlation time rot. τ_c [s]	rate constant[1] k_{12} [s^{-1}]	k_{21} [s^{-1}]	correlation time wobb. τ_c [s]	opening angle wobb.[3] θ_0	population major site p_1	line width $1/T_2^0$ [s^{-1}]
292	145	$1.1\cdot10^{-11}$	$3.2\cdot10^{10}$	$2.9\cdot10^{10}$		24	0.36	1500
280	145	$1.5\cdot10^{-11}$	$2.5\cdot10^{10}$	$2.1\cdot10^{10}$		24	0.37	1500
270	150	$2.2\cdot10^{-11}$	$1.7\cdot10^{10}$	$1.4\cdot10^{10}$		21	0.38	1500
250	150	$3.5\cdot10^{-11}$	$1.1\cdot10^{10}$	$8.9\cdot10^{9}$		21	0.38	1500
240	150	$4.5\cdot10^{-11}$	$8.4\cdot10^{9}$	$6.9\cdot10^{9}$		21	0.38	1500
220	150	$9\cdot10^{-11}$	$4.4\cdot10^{9}$	$3.4\cdot10^{9}$		21	0.39	1500
200	150	$1.5\cdot10^{-10}$	$2.7\cdot10^{9}$	$2\cdot10^{9}$		21	0.4	1500
190	150	$2.5\cdot10^{-10}$	$1.6\cdot10^{9}$	$1.2\cdot10^{9}$		21	0.4	1500
180	150	$2.7\cdot10^{-10}$	$1.5\cdot10^{9}$	$1.1\cdot10^{9}$		21	0.41	1500
172	150	$2.9\cdot10^{-10}$	$1.4\cdot10^{9}$	$1\cdot10^{9}$		21	0.41	2000
164	150	$9.5\cdot10^{-8}$	$4.4\cdot10^{6}$	$3.1\cdot10^{6}$		21	0.42	2000
157	150	$1\cdot10^{-7}$	$4.3\cdot10^{6}$	$2.9\cdot10^{6}$		21	0.43	2000
150	150	$1.3\cdot10^{-7}$	$3.5\cdot10^{6}$	$2.1\cdot10^{6}$		21	0.45	2000
148	150	$1.5\cdot10^{-7}$	$3\cdot10^{6}$	$1.8\cdot10^{6}$		21	0.45	2500
145	155	$2.3\cdot10^{-7}$	$2\cdot10^{6}$	$1.2\cdot10^{6}$		19	0.45	3000
143	160	$2.5\cdot10^{-7}$	$1.9\cdot10^{6}$	$1.1\cdot10^{6}$	$3\cdot10^{-10}$	16	0.47	3500
140	165	$3\cdot10^{-7}$	$1.6\cdot10^{6}$	$8.7\cdot10^{5}$	$4.4\cdot10^{-10}$	12	0.48	4000
136	165	$5\cdot10^{-7}$	$1\cdot10^{6}$	$5\cdot10^{5}$	$5\cdot10^{-10}$	12	0.5	5000
130	165	$5.5\cdot10^{-7}$	$1.1\cdot10^{6}$	$3.6\cdot10^{5}$	$1\cdot10^{-9}$	12	0.6	5500
126	165	$6.5\cdot10^{-7}$	$1\cdot10^{6}$	$2.7\cdot10^{5}$	$1.2\cdot10^{-9}$	12	0.65	5500
122	165	$9\cdot10^{-7}$	$7.8\cdot10^{5}$	$1.7\cdot10^{5}$	$1.3\cdot10^{-9}$	12	0.7	5500
119	165	$9.6\cdot10^{-7}$	$9.2\cdot10^{5}$	$6.3\cdot10^{4}$	$1.9\cdot10^{-9}$	12	0.88	5500
116	165	$9.8\cdot10^{-7}$	$9\cdot10^{5}$	$6.1\cdot10^{4}$	$2.2\cdot10^{-9}$	12	0.88	5500
110	165	$1.1\cdot10^{-6}$	$8.1\cdot10^{5}$	$5\cdot10^{4}$	$2.8\cdot10^{-9}$	12	0.89	5500
100	170	$\leq 1.5\cdot10^{-6}$					≤ 0.9	8000

[1] k_{ij}: rate constant for transition j → i, $\frac{1}{\tau_c} = \frac{k_{12}}{p_1} = \frac{k_{21}}{p_2}$

[2] quadrupole coupling constant, * values for line shape simulations (motionally averaged values due to wobbling motion)

[3] opening angle for 19-site wobble motion

Table 5.5 Simulation parameters for 1,11-dibromoundecane-1,1,11,11-d_4/urea.

Temp. T [K]	Quadrupole[2] coup.cons. e^2qQ/h^* [kHz]	correlation time rot. τ_c [s]	rate constant[1] k_{12} [s^{-1}]	rate constant[1] k_{21} [s^{-1}]	correlation time wobb. τ_c [s]	opening angle wobb.[3] θ_0	population major site p_1	line width $1/T_2^0$ [s^{-1}]
292	145	$1.1\cdot10^{-11}$	$3.2\cdot10^{10}$	$2.9\cdot10^{10}$		24	0.35	1500
280	145	$1.5\cdot10^{-11}$	$2.4\cdot10^{10}$	$2.1\cdot10^{10}$		24	0.36	1500
260	145	$2.5\cdot10^{-11}$	$1.5\cdot10^{10}$	$1.3\cdot10^{10}$		24	0.37	1500
250	145	$3.5\cdot10^{-11}$	$1.1\cdot10^{10}$	$8.9\cdot10^{9}$		24	0.38	1500
240	150	$4.5\cdot10^{-11}$	$8.7\cdot10^{9}$	$6.8\cdot10^{9}$		21	0.39	1500
230	150	$5.8\cdot10^{-11}$	$6.8\cdot10^{9}$	$5.2\cdot10^{9}$		21	0.4	1500
220	150	$9\cdot10^{-11}$	$4.5\cdot10^{9}$	$3.3\cdot10^{9}$		21	0.41	1500
210	150	$1.4\cdot10^{-10}$	$3\cdot10^{9}$	$2.1\cdot10^{9}$		21	0.42	1500
200	150	$2\cdot10^{-10}$	$2.1\cdot10^{9}$	$1.5\cdot10^{9}$		21	0.42	1500
190	150	$2.4\cdot10^{-10}$	$1.7\cdot10^{9}$	$1.2\cdot10^{9}$		21	0.42	1500
180	150	$2.6\cdot10^{-10}$	$1.6\cdot10^{9}$	$1.1\cdot10^{9}$		21	0.43	1500
175	155	$2.8\cdot10^{-10}$	$1.5\cdot10^{9}$	$1\cdot10^{9}$		19	0.43	1500
170	160	$2\cdot10^{-7}$	$2.2\cdot10^{6}$	$1.4\cdot10^{6}$	$3\cdot10^{-10}$	16	0.43	1500
165	160	$3\cdot10^{-7}$	$1.5\cdot10^{6}$	$9\cdot10^{5}$	$5.5\cdot10^{-10}$	16	0.46	1500
160	160	$3.5\cdot10^{-7}$	$1.4\cdot10^{6}$	$7.1\cdot10^{5}$	$6\cdot10^{-10}$	16	0.5	1500
155	165	$3.7\cdot10^{-7}$	$1.4\cdot10^{6}$	$6.6\cdot10^{5}$	$8.2\cdot10^{-10}$	12	0.51	1500
150	165	$4\cdot10^{-7}$	$1.3\cdot10^{6}$	$6\cdot10^{5}$	$1\cdot10^{-9}$	12	0.52	2000
140	165	$5\cdot10^{-7}$	$1.2\cdot10^{6}$	$3.8\cdot10^{5}$	$1.2\cdot10^{-9}$	12	0.62	3000
130	165	$8\cdot10^{-7}$	$1\cdot10^{6}$	$1.3\cdot10^{5}$	$1.3\cdot10^{-9}$	12	0.8	4000
120	165	$1\cdot10^{-6}$	$8.2\cdot10^{5}$	$9\cdot10^{4}$	$1.4\cdot10^{-9}$	12	0.82	4000
110	165	$1.2\cdot10^{-6}$	$7.5\cdot10^{5}$	$4.2\cdot10^{4}$	$1.7\cdot10^{-9}$	12	0.9	4000
100	170	$\leq 2.5\cdot10^{-6}$					≤ 0.9	5000

[1] k_{ij}: rate constant for transition $j \rightarrow i$, $\frac{1}{\tau_c} = \frac{k_{12}}{p_1} = \frac{k_{21}}{p_2}$

[2] quadrupole coupling constant, * values for line shape simulations (motionally averaged values due to wobbling motion)

[3] opening angle for 19-site wobble motion

During the aforementioned simulations, the relative populations of the sites p_1 to p_3 had to be changed, as shown in Figure 5.14. It is interesting to note that upon crossing the phase transition for both samples a drastic increase of p_1 is registered. However, the changes are continuous. There is no sudden jump in p_1 at the corresponding phase transition.

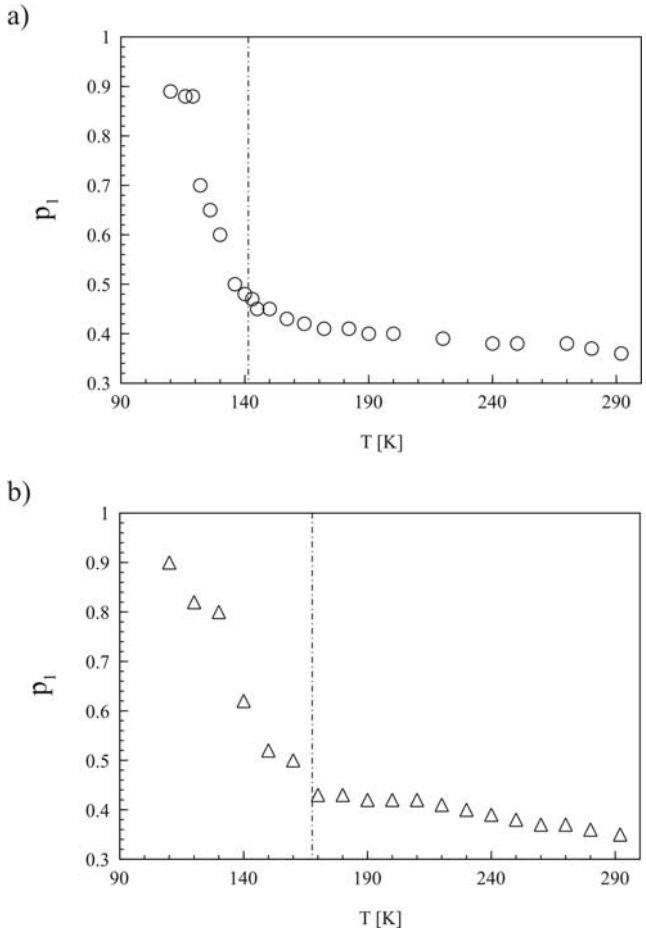

Figure 5.14 Population of unique site 1 as a function of temperature for (a) 1,10-dibromodecane and (b) 1,11-dibromoundecane in urea (dashed line denotes solid-solid phase transition).

5.1.4 Discussion

The present ^{13}C, ^{1}H and ^{2}H NMR study provides an insight into the molecular properties of the guest molecules in the present inclusion compounds. The

enclathration of the guest molecules in urea gives rise to a change in the guest conformational order which is illustrated by the observed alternation of ^{13}C and ^{1}H chemical shifts for the guest molecules. The strong dipolar interaction between the guest and the host compounds is confirmed by the experiments on the guest molecules in deuterated and non-deuterated urea, which, for instance, is expressed by an enhanced ^{1}H spin diffusion (shorter ^{1}H $T_{1\rho}$ values) for the non-deuterated sample.

From the results presented above, it is found that the distortion of the urea channels at the phase transition temperature causes changes of the dynamic properties of the guest molecules, which is reflected by a distinct alteration of the relative populations of the jump sites. In the high temperature phase, the urea channels display a hexagonal symmetry and a slightly larger cross-sectional area. As a consequence, the relative populations of all sites are nearly equal. At the solid-solid phase transition, the symmetry of the urea channels decreases, which results in a continuous increase of the population for the unique site, reaching a maximum value of about 0.9 at the lowest temperature.

For the two samples investigated, the difference between the phase transition temperatures of about 26 K results in a similar shift for the absolute rate constants. The activation energies, however, are very similar. Low-Frequency Raman Spectra [183] of crystals for pure α,ω-disubstituted *n*-alkanes $Br(CH)_nBr$ with n in the range of 7-23 showed pronounced 'odd-even' effect in longitudinal acoustical mode (LAM-1) frequency. A probable reason is that in the α,ω-disubstituted *n*-alkanes free chains are freely packed in the layer crystal, and the difference between the packing structures of chains of odd and even molecules can be detected, especially for short dibromides ($n < 12$). On the contrary, the guest molecules in urea are isolated and lie in a constrained environment. The diameter of the urea channels is about 5.6 Å, the guest molecules trapped in long channels can only take extended linear conformations but have enough space to rotate. The actual chain length, i.e. odd-even effects, therefore plays a minor role for the properties of the present guest molecules in urea

inclusion compounds.

For the high temperature phase, the small difference for the activation energies of the overall rotation for 1,10-dibromodecane-d_4 and 1,11-dibromoundecane-d_4 guests can be related to the different chain lengths. Steric repulsion dominates the interactions between host and guest atoms. Longer chains have proportionally more atoms in contact with the host and thus a stronger steric repulsion. This property has already been observed in alkanoic acids UICs and alkane UICs for the high temperature phase [4]. With an approximately linear fit of E_a on increasing chain length, the alkanoic acids exhibit a slope of 1.8 and alkanes 0.4 kJ/mole per CH_2 sequence [4]. From the activation energies $E_{a,\,12}$ for 1,10-dibromodecane-d_4/urea and 1,11-dibromoundecane-d_4/urea in the high temperature phase, the slope for α,ω-dibromoalkane guest molecules is 0.7 kJ/mole per CH_2 sequence, which falls between the UICs with the aforementioned guests. This is an anticipated result and can be explained by stronger van der Waals forces both between the guests and guests, and guests and host molecules. For octanoic acid [4] and 1,6-dibromohexane [8, 44], typically, very high activation energies for the motion of guest molecules are observed which arises from the fact that here more restricted guest motions occur [8, 44].

Table 5.6 Activation energies for different temperature regions of 1,10-dibromo-decane and 1,11-dibromoundecane in urea.

1.1.1 Activation energy ($kJ \cdot mol^{-1}$)		rotation		wobbling
		room temp. – 190 K	LT phase below T_{1Z} minimum	
$BrC_{10}H_{20}Br$	$E_{a,\,12}$	13.1 ± 0.4	4.6 ± 0.6	6.7 ± 1.2
	$E_{a,\,21}$	14.0 ± 0.5	11.7 ± 0.8	
$BrC_{11}H_{22}Br$	$E_{a,\,12}$	13.8 ± 0.4	2.9 ± 0.3	3.1 ± 0.6
	$E_{a,\,21}$	15.0± 0.5	8.5 ± 0.3	

The deuterium NMR spectra presented in Figure 5.4 and 5.5 show that the 3-site jump model combined with the overall chain wobbling motion provides a reasonable description of the guest molecular motion over the temperature range of interest, but agreement between experimental and simulated spectra is not completely perfect, most notably at the low-temperature range. Perdeuterated 1,10-dibromodecane-d_{20}/urea has been studied by Aliev et al. [53]. Theoretical ^{2}H NMR spectra, described by rotational diffusion in a six-fold cosine potential, were contrasted with their experimental counterparts in the range from 97 to 128 K, although no quantitative analysis was made. In addition, activation energy of 13.5 kJ/mole was derived from the experimental T_{1Z} values as a function of temperature for the high temperature phase, but again no quantitative line shape analysis was made.

However, as demonstrated in this work, the anisotropy of the relaxation time (T_{1Z}, T_2) is very useful for the discrimination between different motional models. For instance, although it might be possible to reproduce the experimental fast exchange ^{2}H NMR line shapes by different data sets the T_{1Z} and T_2 anisotropy – as directly reflected by the line shape alterations of the partially relaxed spectra – in general strongly varies with the underlying motional model.

Simulations were also done in the present work by employing other motional models. As mentioned earlier, taking into accounting of the C_6 symmetry of the urea channel, a non-degenerate 6-site jump model could also be used which, however, cannot be distinguished from the 3-site model. Based on a previous study [53], rotational diffusion in a two plus six fold cosine potential was also tested. Here, the trigonometric potential is given by a process with n plus m fold unequivalent wells: $U(\phi)=\frac{U_{01}}{2}\left[1-\cos(n\phi)\right]+\frac{U_{02}}{2}\left[1-\cos(m\phi)\right]$ with n = 2, m = 6 and ϕ is the Euler angle, U_{01} and U_{02} are the potential well heights chosen as 5 kJ/mol. The probability distribution is determined by this potential $U(\phi)$ and the population as $P(\phi)=N^{-1}e^{-U(\phi)/kT}$ (k is the Boltzman constant). The dimension of the rate matrix

was taken as N = 36, corresponding to a grid spacing of δ =10° on a circle. However, the theoretical line shapes from these motional models were practically identical to the spectra obtained from the simpler 3-site jump model, the latter of which was therefore used for the description of the overall rotational process.

Despite a small fraction of gauche conformations assumed in the systems under investigation [9], in contrast to the overall molecular wobbling motion, the contribution of the gauche-trans isomerization motion to the reduction of the spectral splitting is very small which therefore has been neglected.

IQNS experiments was also employed to examine the dynamic properties of the guest molecules in 1,10-dibromodecane/urea-d_4 [27]. In this case, translational and rotational diffusion in a onefold cosine potential on a picosecond time scale for the high temperature phase and an oscillatory motion in the low temperature phase were explicitly considered. It was reported that for the UIC with nonadecane these motions exist in the high temperature phase, while they are absent in the low temperature phase [6]. Translational motion of the guest species within the urea channels cannot be directly detected in the ^{2}H NMR experiments. It is assumed that such motion indirectly gives rise to the changes of ^{13}C $T_{1\rho}$ values of the guest species in urea and urea-d_4 and of the residual $1/T_2^0$ values of the experimental ^{2}H NMR line shapes. Thus the residual $1/T_2^0$ value should contain contributions from homonuclear (^{2}H-^{2}H) and heteronuclear (^{2}H-^{1}H) dipolar interactions. The latter part could be further subdivided into intra- and intermolecular contributions. The reduction in residual $1/T_2^0$ at the phase transition is attributed to the loss of the intermolecular contribution between the guest molecules and the rigid urea matrix. That is, in the high temperature phase the fast jump, overall molecular wobbling and translational motions result in an averaging of the intermolecular dipole interactions. Thus, in the low temperature phase for 1,10-dibromodecane-d_4/urea the values of $1/T_2^0$ = 5.5 kHz and 4 kHz for 1,11-dibromoundecane-d_4/urea have been used in the simulations of line shapes and partially relaxed spectra from quadrupole echo experiments while for

the high-temperature phase the values of 1.5 kHz for 1,10-dibromodecane-d_4/urea and for 1,11-dibromoundecane-d_4/urea were found to be sufficient. Similar observations have also been reported for deuterated six-membered rings in cyclophosphazene inclusion compounds [158] and hexadecane/UICs [7].

5.1.5 Conclusions

Solid-state NMR spectroscopy is utilized to study the molecular behavior of 1,10-dibromodecane and 1,11-dibromoundecane in urea inclusion compounds. The guest dynamics and conformational order are explored by ^{13}C CP/MAS and ^{1}H MAS NMR experiments (line shapes, spin-lattice relaxation). All-trans conformation of the guest chains and the interactions between the guests and hosts are confirmed. Dynamic ^{2}H NMR experiments are carried out on two guest molecules selectively deuterated at both end groups. The quantitative analysis of the experimental data, obtained from variable temperature line shape, spin-spin relaxation and spin-lattice measurements, shows that both guest molecules undergo similar motions within the investigated temperature range between 100 K and room temperature. The combination of a non-degenerate three-site or six-site jump model and additional small-angle overall chain wobbling is able to characterize the motions of the guest molecules. It is found that the populations of the jump sites exhibit a pronounced temperature dependence, although discontinuities at the solid-solid phase transition were not registered. The same holds for the guest dynamics which are not directly affected by the change in urea lattice structure. Rather a discontinuity in the guest dynamics is observed at about 30 degrees for 1,10-dibromodecane and 10 degrees for 1,11-dibromoundecane in urea above the solid-solid phase transition.

5.2 1,6-dibromohexane/urea inclusion compounds

Urea inclusion compounds with 1,6-dibromohexane were investigated by variable temperature ^{2}H NMR spectroscopy. In addition, ^{1}H and ^{13}C solid-state NMR studies

were performed for the same system. ^{2}H NMR studies were conducted on two inclusion compounds with non-deuterated urea, and 1,6-dibromohexane deuterated either at carbons C-1/C-6 (α-positions) or at carbons C-2/C-5 (β-positions) (see Fig. 5.15). For the ^{13}C and ^{1}H NMR studies, samples with 1,6-dibromohexane and urea or urea-d_4 were prepared. For comparison, some data will be present for 1,10-dibromodecane/urea again [176]. Samples were checked by differential scanning calorimetry. In agreement with earlier reports [8, 55] for 1,6-dibromohexane/urea no solid-solid state phase transitions could be observed between 130 K and the disintegration point of the inclusion compound at 337 K. The thermal behaviour of 1,6-dibromohexane/urea is different from that encountered for UICs with n-alkanes or long-chain dibromoalkanes, such as 1,10-dibromohexane, where characteristic solid-solid transitions, accompanied by a change of the host lattice structure, are registered [9, 176].

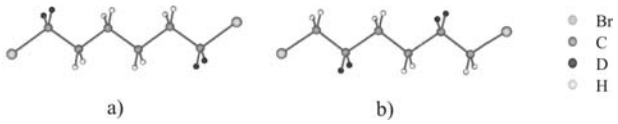

Figure 5.15 Molecular structures for 1,6-dibromohexane-1,1,6,6-d_4/urea (left) and 1,6-dibromohexane-2,2,5,5-d_4/urea (right).

It should be noted that studies about 1,6-dibromohexane/urea were published recently which addressed the structural properties of this system and the dynamic features of the guest species [8, 54, 55]. Variable temperature X-ray diffraction studies showed that the isomorphous monoclinic structure (space group $P2_1/n$) at 100 K gradually transforms towards hexagonal symmetry when approaching room temperature [55]. Moreover, the guest components were found to exist exclusively in two non-degenerate gauche conformational states (with one predominant site), and are assumed to undergo mutual exchange between these two states. It is important to note that the exchange is not an internal process. Rather, it affects the whole molecule, and restricted reorientational motion of the molecule thus takes place. In addition,

motional correlation times were reported for the gauche-gauche interconversion process on the basis of variable temperature ^{2}H NMR line shapes on UICs with selectively deuterated 1,6-dibromohexane guests [8], although the observed spectral effects were rather subtle. The existence of a predominant gauche conformational state was also confirmed independently by a Raman investigation [54].

5.2.1 ^{13}C CP/MAS and ^{1}H MAS NMR studies

Figure 5.16 depicts ^{13}C CP/MAS spectra of 1,6-dibromohexane/urea and 1,10-dibromodecane/urea which were recorded at room temperature. Peak assignments along with the corresponding data for the guest species from solution NMR studies are summarized in Table 5.7. It can be seen that the ^{13}C NMR signals of the dibromoalkanes experience a pronounced downfield shift upon enclathration in urea. In fact, unusual large shifts up to about 5 ppm for 1,6-dibromohexane can be observed. Similar ^{13}C chemical shift alterations were reported earlier, for instance, for n-alkanes [25] and branched n-alkanes [177] in urea, and were attributed to changes of the conformational state. On the basis of these observations and the results from ^{2}H NMR, Raman, IR and X-ray investigations [4-9, 25, 54, 55, 177], it was concluded that n-alkanes in urea adopt a nearly all-trans conformational state while in solution a fast equilibrium between gauche and trans conformers exists. The present data for the UIC with the long-chain analogue 1,10-dibromodecane can be understood in quite the same way. That is, 1,10-dibromodecane in urea – unlike the situation in solution – again exists in an almost all-trans conformation which also has been established from Raman experiments [9]. However, in the case of 1,6-dibromohexane even larger downfield shifts are registered which cannot be explained in the same way. As mentioned earlier, these guests exclusively exist in two states [8, 54, 55] which are characterized by a gauche conformation at the chain ends. That is, for 1,6-dibromohexane/urea the observed ^{13}C downfield shifts must reflect a change from coexisting gauche and trans conformers in solution towards two coexisting gauche conformers. This implies that in general the chemical shift alterations in urea

inclusion compounds are not solely based on conformational effects. Rather they also reflect other alterations of the electronic environment around the guest carbon nuclei due to interactions with the urea host lattice.

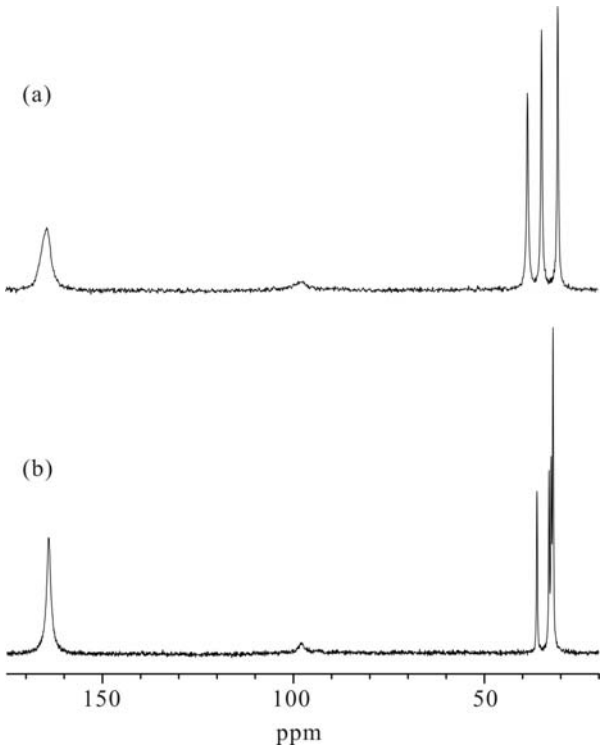

Figure 5.16 ^{13}C CP/MAS NMR spectra of (a) 1,6-dibromohexane, and (b) 1,10-dibromo-decane in urea.

The interaction between the urea host lattice and the guest species also becomes evident from the comparison of the ^{13}C NMR line widths in the UICs from urea and urea-d_4 (see Table 5.7). Thus, for the latter samples larger line widths of the guest species are found than for the sample made from non-deuterated urea, which is attributed to remaining ^{13}C-^{2}H dipolar couplings between the guest species and the host matrix. The ^{13}C NMR line width of the urea carbonyl group is found to become smaller upon urea deuteration, which reflects interference effects [178, 179] between the ^{1}H decoupling r.f. field and the urea reorientational motions, i.e., 180° flips around the C=O and the C-N bonds [39, 180]. Insufficient ^{1}H decoupler power can be ruled out. In fact, an increase of the ^{1}H decoupler power is accompanied by a broadening

for the carbonyl ^{13}C NMR signal which is in line with the aforementioned interference effect. Similar observations were made for other UICs [176].

Table 5.7 NMR parameters from ^{13}C and ^{1}H NMR studies on 1,6-dibromohexane and 1,10-dibromodecane in solution and UICs.

(a) $BrC_6H_{12}Br$

	δ_{13C} [ppm]			$\Delta\nu_{1/2\ (13C)}$[c]			δ_{1H} [ppm]	
	solution[a]	urea[b]	urea-d_4	urea	urea-d_4		solution[d]	urea[e]
C-1	33.5	38.4	38.1	37.3	65.7	H (C-1)	3.4	3.8
C-2	32.5	34.7	34.4	32.0	49.3	H (C-2)	1.8	2.2
C-3	27.3	30.5	30.2	29.4	47.5	H (C-3)	1.5	1.8
C=O		164	164	220	137			

(b) $BrC_{10}H_{20}Br$

	δ_{13C} [ppm]			$\Delta\nu_{1/2\ (13C)}$[c]			δ_{1H} [ppm]	
	solution[a]	urea[b]	urea-d_4	urea	urea-d_4		solution[d]	urea[e]
C-1	33.9	36.2	36.1	20.4	28.5	H (C-1)	3.4	3.5
C-2	32.8	33.1	32.9	22.7	36.5	H (C-2)	1.9	2.1
C-3,4	28.7– 28.2	32.0	31.9	22.5	33.8	H (C-3)	1.5	1.5
C-5	29.3	32.5	32.3	31.8	39.6	H (C-4,5)	1.3	1.5
C=O		164	164	91.6	51.9			

[a] ^{13}C chemical shifts of 1,6-dibromohexane, 1,10-dibromodecane in $CDCl_3$. Assignments from refs. 184, 185.

[b] ^{13}C chemical shifts of 1,6-dibromohexane and 1,10-dibromodecane in their UICs derived in this work from ^{13}C CP/MAS studies.

[c] ^{13}C NMR line width.

[d] ^{1}H chemical shifts of 1,6-dibromohexane and 1,10-dibromodecane in $CDCl_3$ [181].

[e] ^{1}H chemical shifts of 1,6-dibromohexane and 1,10-dibromodecane in their UICs derived in this work from ^{1}H MAS experiments.

It is worth mentioning that the optimum contact time for cross-polarization is found to vary considerably with guest species and deuteration of the urea matrix. Thus, for 1,6-dibromohexane/urea, a maximum ^{13}C CP signal was observed at a contact times of 0.3 ms and 0.9 ms for urea and urea-d_4, respectively, while for 1,10-dibromodecane these values are 2 and 8 ms. Two major reasons might be responsible for these findings: (i) differences for the motions of guest species which interfere with the cross-polarization process, and/or (ii) differences for the average distances between guest and host molecules. The longer contact times needed for the deuterated urea clathrates can be attributed to the loss of urea protons which are an important source for magnetization transfer during cross-polarization. This assumption is also confirmed by the ^{1}H MAS NMR data discussed below. Similar trends for the ^{13}C signal intensity during cross-polarization were also observed recently for other urea inclusion compounds [176].

Figure 5.17 exhibits ^{1}H MAS NMR spectra recorded at 15 kHz for 1,6-dibromo-hexane and 1,10-dibromodecane in urea and urea-d_4. For 1,6-dibromohexane/urea highly resolved ^{1}H NMR spectra are observed even at moderate spinning rates of 15 kHz which indicates a reduced spin diffusion for this UIC. Deuteration of the urea host lattice is accompanied by additional resolution enhancement for the ^{1}H NMR signals of the guest species. Obviously, upon urea deuteration proton spin diffusion is further suppressed, as the large proton spin reservoir from the non-deuterated urea molecules is missing, and only reduced intermolecular dipolar interactions between isolated guests exist. A comparison of the derived ^{1}H chemical shift values again reveals downfield shifts upon enclathration for both urea samples with 1,6-dibromohexane and 1,10-dibromodecane where for 1,6-dibromohexane/urea larger effects are registered (shifts up to 0.4 ppm). As before, these chemical shift alterations are traced back to conformational changes and/or interactions between guest molecules and host matrix.

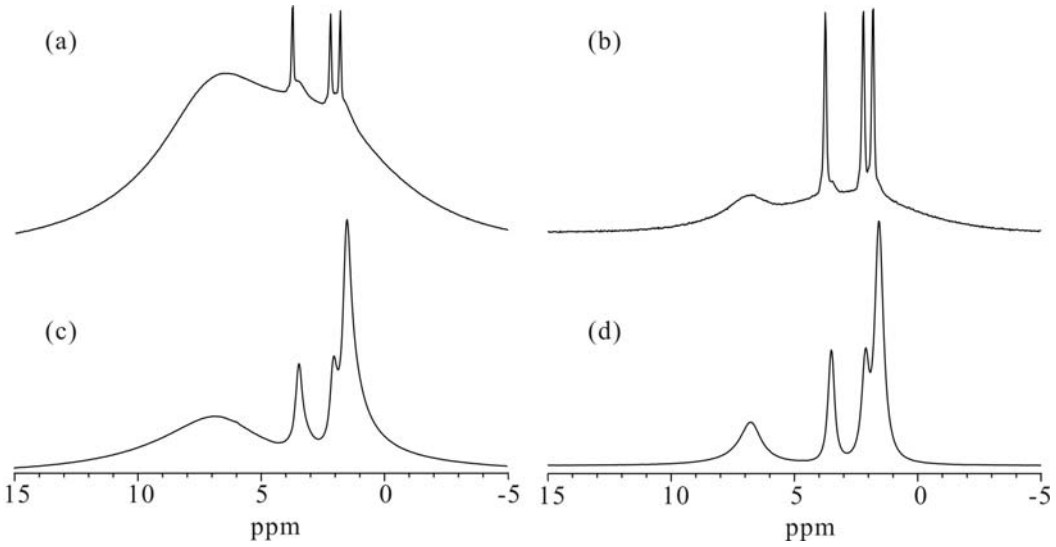

Figure 5.17 ^{1}H MAS NMR spectra of (a) 1,6-dibromohexane/urea, (b) 1,6-dibromodecane/urea-d_4, (c) 1,10-dibromodecane/urea, and (d) 1,10-dibromodecane/urea-d_4.

Further line narrowing can be achieved through sample spinning at 34 kHz (data not shown). However, for 1,6-dibromohexane/urea additional resonances show up which stem from the presence of free guest molecules. That is, due to temperature increase upon fast MAS, guest molecules diffusive out of the urea host lattice and a disintegration of the UIC sets in. Similar effects arising from partial disintegration of the UIC are also found during the variable temperature ^{2}H NMR studies presented below.

The dynamic properties of the guest components are examined by ^{13}C $T_{1\rho}$, ^{13}C T_1 and ^{1}H $T_{1\rho}$ measurements. The derived data are summarized in Tables 5.8 and 5.9. For 1,6-dibromohexane/urea it is found that the ^{13}C $T_{1\rho}$ values slightly vary with chain position, as reflected by a $T_{1\rho}$ increase toward the inner part of the chain. Urea deuteration is characterized by an increase for both the ^{13}C $T_{1\rho}$ and ^{1}H $T_{1\rho}$ values due to reduced effective hetero- and homonuclear dipolar interactions between guest and host components. From the variable temperature ^{13}C $T_{1\rho}$ data it can be concluded that the underlying motions are on the high temperature branch of the relaxation curve.

The ^{13}C T_1 values are slightly longer than the ^{13}C $T_{1\rho}$ values (about a factor of 4), they do not exhibit a distinct position dependence, and are almost unaffected by urea deuteration. Moreover, ^{13}C T_1 minima are found at 305 K, while the UIC with 1,10-dibromodecane/urea behaves completely different. For instance, considerable larger ^{13}C $T_{1\rho}$ and ^{13}C T_1 values of about 400 ms and 8 s, respectively, are observed at room temperature. Further details can be found elsewhere [176].

Table 5.8 $T_{1\rho(C)}$ and $T_{1\rho(H)}$ data for the $BrC_6H_{12}Br$ in urea and urea-d_4.

$BrC_6H_{12}Br$/urea	$T_{1\rho(13C)}$ [ms]				$T_{1\rho(1H)}$
(CT[a]: 0.3ms)	294K	305K	310K	320K	[ms][b]
C-1	45.6	55.9	61.4	64.6	1.2
C-2	57.9	65.7	69.4	71.8	1.2
C-3	63.5	73.8	76.5	82.2	1.2
$BrC_6H_{12}Br$/urea-d_4	$T_{1\rho(13C)}$ [ms]				$T_{1\rho(1H)}$
(CT: 0.9ms)	294K	305K	310K	320K	[ms]
C-1	54.0	73.7	80.7	88.0	9.0
C-2	80.6	87.3	103	114	9.3
C-3	88.8	98.7	122	146	9.4

[a] contact time

[b] value at 294 K

We made an attempt for a semi-quantitative analysis of these ^{13}C relaxation data by using the well-known expressions [172] for $T_{1\rho}$ and T_1 in the presence of isotropic motions and a dominant heteronuclear dipolar interaction

$$\frac{1}{T_1(^{13}C)} = A^2\left[J(\omega_{0,H}-\omega_{0,C})+3\cdot J(\omega_{0,C})+6\cdot J\left(\omega_{0,H}+\omega_{0,C}\right)\right] \tag{5.2}$$

$$\frac{1}{T_{1\rho}(^{13}C)} = \frac{A^2}{2}\left[4\cdot J(\omega_{1,C})+J(\omega_{0,H}-\omega_{0,C})+3\cdot J(\omega_{0,C})+6\cdot J\left(\omega_{0,H}+\omega_{0,C}\right)+6\cdot J(\omega_{0,H})\right] \tag{5.3}$$

with $$J_n(\omega_i) = \frac{\tau_c}{1+\omega_i^2\tau_c^2}; \qquad \omega_i = \gamma B_i \qquad (5.4)$$

Here A^2 is a factor which contains the gyromagnetic ratios of the interacting nuclei, and the average internuclear distance as $<1/r^3>$. $\omega_{0,C}$ and $\omega_{0,H}$ are the Larmor frequencies of the ^{13}C and ^{1}H nuclei, respectively, and $\omega_{1,C}$ is the nutation frequency of the radio frequency field $B_1(^{13}C)$.

Table 5.9 $T_{1(C)}$ data for the $BrC_6H_{12}Br$ in urea and urea-d_4.

$BrC_6H_{12}Br$/urea	$T_{1(13C)}$ [ms]			
(CT[a]: 0.3ms)	294K	305K	310K	320K
C-1	216	203	205	216
C-2	226	193	193	194
C-3	228	216	223	225
$BrC_6H_{12}Br$/urea-d_4	$T_{1(13C)}$ [ms]			
(CT[a]: 0.9ms)	294K	305K	310K	320K
C-1	242	203	209	209
C-2	251	189	193	194
C-3	255	203	211	219

[a] contact time

In a first step, the experimental ^{13}C T_1 curve – which exhibits a minimum (see above) – was fitted by means of equation (5.2). In this way, factor A and the correlation times τ_c of the motion responsible for spin-lattice relaxation were determined. In the second step, we assumed that the same factor A can be employed for the analysis of the experimental ^{13}C $T_{1\rho}$ data. That is, equation (5.3) along with the factor A – derived via the ^{13}C T_1 analysis – were used to obtain the correlation times for the motions which dominate $T_{1\rho}$ relaxation. The two sets of correlation times from the ^{13}C T_1 and $T_{1\rho}$ data analysis are summarized in Tables 5.10 and 5.11. It can be seen that the correlation times derived from the ^{13}C T_1 data analysis are in a very similar range as

those obtained from the quantitative ^2H T_1 analysis discussed below. Nevertheless, the derived kinetic data from the ^{13}C relaxation experiments can be only discussed on a qualitative basis, as a simple isotropic motion was employed during this part of the data analysis. The corresponding ^2H NMR relaxation data analysis, however, is straightforward, as here the correct (anisotropic) motional model for the guest dynamics was employed.

Table 5.10 Kinetic parameters derived from $T_{1\rho(13C)}$ values for the $BrC_6H_{12}Br$ in UICs.

$BrC_6H_{12}Br$/urea	correlation time τ_c [10^{-9} s]				activation energy
(CT: 0.3ms)	294K	305K	310K	320K	[kJ/mole]
C-1	8.5	6.5	6.0	5.6	12.8±2.4
C-2	6.0	5.1	4.6	4.5	9.1±1.9
C-3	6.0	5.0	4.8	4.4	9.3±1.1
$BrC_6H_{12}Br$/urea-d_4	correlation time τ_c [10^{-9} s]				activation energy
(CT: 0.9ms)	294K	305K	310K	320K	[kJ/mole]
C-1	6.9	4.6	4.1	3.7	19.1±3.7
C-2	3.7	3.3	2.5	2.1	17.9±3.8
C-3	3.6	3.1	2.1	1.5	27.4±5.9

On the basis of these results from the semi-quantitative ^{13}C $T_{1\rho}$ analysis it is concluded that (i) ^{13}C T_1 relaxation reflects the same motion being responsible for ^2H T_{1Z} and T_{1Q} relaxation, and (ii) ^{13}C $T_{1\rho}$ relaxation is governed by another motional process which occurs on a slower time-scale. ^{13}C T_1 relaxation is therefore considered to be caused by the aforementioned interconversion between two gauche conformers of the guest molecules, while overall fluctuations of the dibromohexane guests dominate ^{13}C $T_{1\rho}$ relaxation. A discussion of this issue will be provided after the presentation of the ^2H NMR results.

Table 5.11 Kinetic parameters derived from $T_{1(13C)}$ values for the $BrC_6H_{12}Br$ in UICs.

$BrC_6H_{12}Br$/urea	correlation time τ_c [10^{-9} s]			
(CT: 0.3ms)	294K	305K	310K	320K
C-1	2.5	1.6	1.4	1.0
C-2	3.2	1.7	1.6	1.5
C-3	2.5	1.6	1.2	1.1
$BrC_6H_{12}Br$/urea-d_4	correlation time τ_c [10^{-9} s]			
(CT: 0.9ms)	294K	305K	310K	320K
C-1	3.4	1.6	1.2	1.1
C-2	4.1	1.6	1.3	1.2
C-3	3.7	1.6	1.1	1.0

5.2.2 ^{2}H NMR line shapes

Variable temperature ^{2}H NMR studies were performed in a temperature range between 220 and 320 K on two urea samples, prepared with 1,6-dibromohexane selectively deuterated at either at carbon positions C-1/C-6 or positions C-2/C-5. Representative variable temperature ^{2}H NMR line shapes of both samples (from quadrupolar echo experiments with τ_e = 20 μs) are displayed in Figure 5.18. It can be seen that for the lowest temperature typical axially symmetric Pake pattern (asymmetry parameter η = 0.0) are observed. Characteristic spectral alterations occur upon sample heating which imply an onset of the guest motions. The observed non-axially symmetric ^{2}H NMR spectra at higher temperatures, characterized by an averaged value of $\langle\eta\rangle \neq 0.0$, are typical for a molecules undergoing motions in the fast exchange limit with a symmetry lower than C_3. It is further registered that the spectral alterations also depend on the deuterated position of the guest species.

For both compounds variable temperature spin-spin (T_2) relaxation studies were performed (data not shown), from which there was no evidence for motionally

induced spin-spin relaxation effects. These findings clearly demonstrate that the underlying guest motions are too fast and outside the sensitive time-scale for NMR line shape analysis. Rather, as outlined below they occur on a time-scale suitable for spin-lattice relaxation studies.

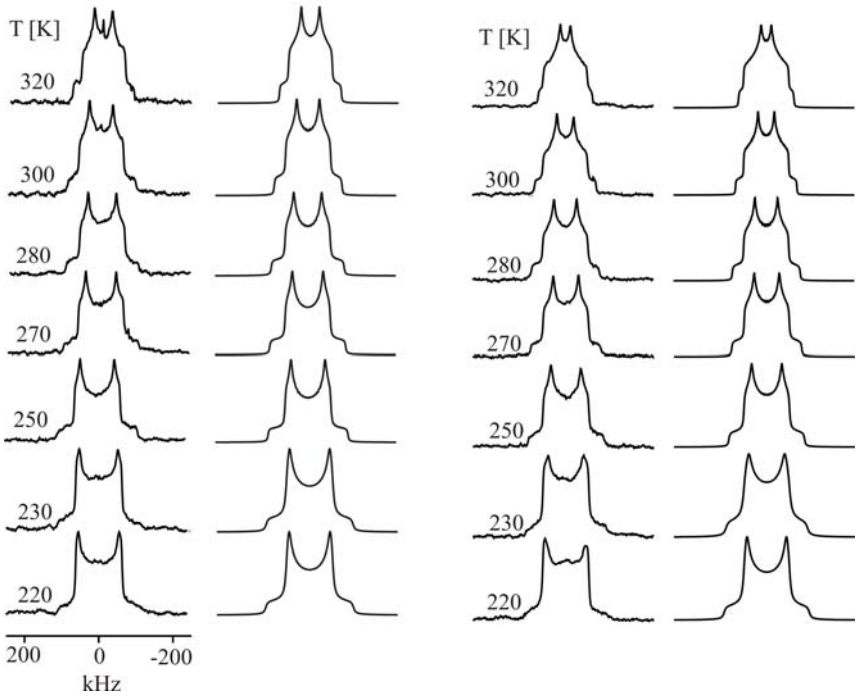

Figure 5.18 ^{2}H NMR line shapes as a function of temperature for 1,6-dibromohexane-1,1,6,6-d_4/urea (left: experiment and simulation) and 1,6-dibromohexane-2,2,5,5-d_4/urea (right: experiment and simulation).

The present variable temperature ^{2}H NMR spectra are identical to those presented in an earlier ^{2}H NMR line shape study on UICs with α-, β- and γ-deuterated 1,6-dibromohexanes [8]. Along with the structural data from a complementary X-ray analysis, the authors described the experimental ^{2}H NMR line shapes by a non-degenerate two-site jump model which was consistent with mutual exchange of the guest species between two coexisting gauche conformers (see Figure 5.19). With the assumption of ideal tetrahedral geometry [8], the jump angles were first calculated to 56° for the α-deuterons and 109° for the β-deuterons. A further refinement [8, 55]

provided a jump angle of $\Delta\varphi_a = 58°$ for the α-deuterons, while the jump angle for the β-deuterons was kept to $\Delta\varphi_b = 109°$.

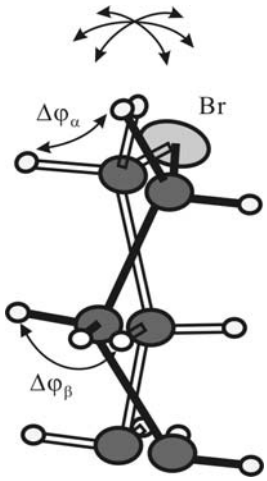

Figure 5.19 Schematic drawing of the two gauche conformers of 1,6-dibromohexane in urea and overall motions discussed in the text.

The theoretical ^{2}H NMR line shapes of 1,6-dibromohexane deuterated in the α- and β-positions, shown in Figure 5.18, were obtained with the same jump angles from the earlier ^{2}H NMR work [8]. However, as there was no evidence for any spin-spin relaxation effects, the motional correlation times were set to the fast exchange limit with $\tau_c = 10^{-8}$ s. The derived populations of the major gauche site slightly differ from the former published data, and are given in Figure 5.20, Tables 5.12 and 5.13 (please note that the given rate constants are derived from the ^{2}H T_1 relaxation data analysis, as outlined below). It can be seen that the populations derived from the analysis of the two deuterated guest species are almost identical. Likewise, the enthalpy differences between the two gauche conformers, calculated from these populations with values of $\Delta H = 9.3$ kJ/mol for the α-deuterated and 8.6 kJ/mol for the β-deuterated samples, are very close to the previously reported value of 8.5 kJ/mol [8].

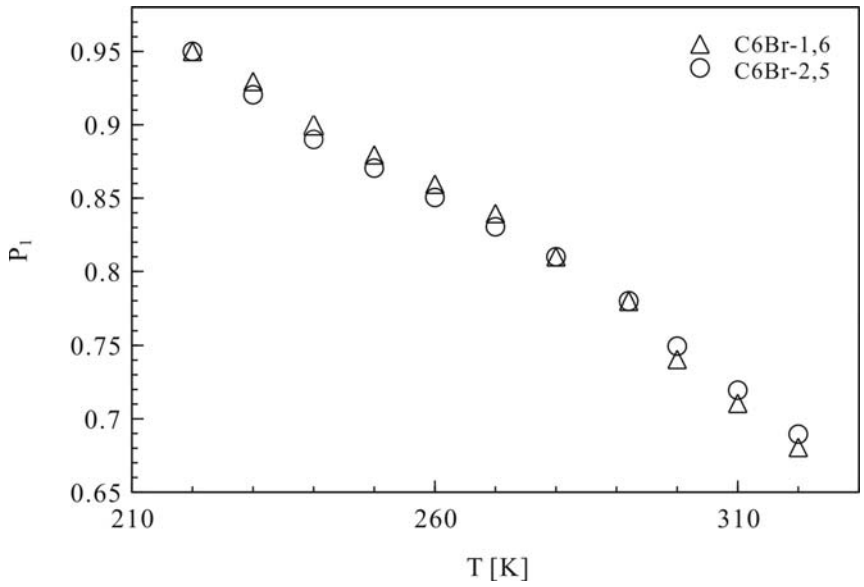

Figure 5.20 Populations of major gauche site as a function of temperature (C6Br-1,6: 1,6-dibromohexane-1,1,6,6-d_4/urea, C6Br-2,5: 1,6-dibromohexane-2,2,5,5-d_4/urea).

The major difference between the present and the former study is the time-scale of gauche-gauche interconversion. Unlike the former work, where the authors proposed that the motions should occur on a time-scale compatible with ^{2}H NMR line shape effects, according to our analysis a faster time-scale has to be considered which matches the sensitive range of spin-lattice relaxation. In fact, there are various arguments which support our assumption:

(i) Model simulations based on the populations and rate constants published in the former work only exhibit subtle effects on the theoretical ^{2}H NMR spectra which hardly can be used to extract accurate motional correlation times.

(ii) Motional induced spin-spin relaxation effects (i. e. angular dependence of T_2) were not found during the quadrupolar echo experiments with variable pulse delay τ_e.

Table 5.12 Simulation parameters for 1,6-dibromohexane-1,1,6,6-d_4/urea.

Temperature	Quadrupolar coupl. const.	Correlation time	Population major site	Rate constant[1]	Rate constant[1]	Line width
T [K]	e^2qQ/h [kHz]	τ_c [s]	p_1	k_{12} [s^{-1}]	k_{21} [s^{-1}]	$1/T_2^0$ [s^{-1}]
320	157	$7\cdot10^{-10}$	0.68	$9.7\cdot10^{8}$	$4.6\cdot10^{8}$	2500
310	160	$8\cdot10^{-10}$	0.71	$8.9\cdot10^{8}$	$3.6\cdot10^{8}$	2500
300	162	$9\cdot10^{-10}$	0.74	$8.2\cdot10^{8}$	$2.9\cdot10^{8}$	3000
292	162	$5\cdot10^{-9}$	0.78	$1.6\cdot10^{8}$	$4.4\cdot10^{7}$	3000
280	162	$6.5\cdot10^{-9}$	0.81	$1.2\cdot10^{8}$	$2.9\cdot10^{7}$	3000
270	164	$1.3\cdot10^{-8}$	0.84	$6.5\cdot10^{7}$	$1.2\cdot10^{7}$	3000
260	164	$1.8\cdot10^{-8}$	0.86	$4.8\cdot10^{7}$	$7.8\cdot10^{6}$	3500
250	164	$2.8\cdot10^{-8}$	0.88	$3.1\cdot10^{7}$	$4.3\cdot10^{6}$	3500
240	165	$4.5\cdot10^{-8}$	0.90	$2\cdot10^{7}$	$2.2\cdot10^{6}$	4000
230	165	$5.7\cdot10^{-8}$	0.93	$1.6\cdot10^{7}$	$1.2\cdot10^{6}$	4500
220	165	$8\cdot10^{-8}$	0.95	$1.2\cdot10^{7}$	$6.3\cdot10^{5}$	5000

[1] k_{ij}: rate constant for transition j → i, jump angle $\Delta\varphi_\alpha = 58°$.

Table 5.13 Simulation parameters for 1,6-dibromohexane-2,2,5,5-d_4/urea.

Temperature	Quadrupolar coupl. const.	Correlation time	Population major site	Rate constant[1]	Rate constant[1]	Line width
T [K]	e^2qQ/h [kHz]	τ_c [s]	p_1	k_{12} [s^{-1}]	k_{21} [s^{-1}]	$1/T_2^0$ [s^{-1}]
320	162	$6.5\cdot10^{-10}$	0.69	$1.1\cdot10^{9}$	$4.8\cdot10^{8}$	1500
310	162	$8\cdot10^{-10}$	0.72	$9\cdot10^{8}$	$3.5\cdot10^{8}$	1500
300	162	$9\cdot10^{-10}$	0.75	$8.3\cdot10^{8}$	$2.8\cdot10^{8}$	1500
292	162	$6\cdot10^{-9}$	0.78	$1.3\cdot10^{8}$	$3.7\cdot10^{7}$	2000
280	162	$8\cdot10^{-9}$	0.81	$1\cdot10^{8}$	$2.4\cdot10^{7}$	2500
270	162	$1.3\cdot10^{-8}$	0.83	$6.4\cdot10^{7}$	$1.3\cdot10^{7}$	2500
260	163	$2.1\cdot10^{-8}$	0.85	$4\cdot10^{7}$	$7.1\cdot10^{6}$	3000
250	164	$3.1\cdot10^{-8}$	0.87	$2.8\cdot10^{7}$	$4.2\cdot10^{6}$	3500
240	164	$4.8\cdot10^{-8}$	0.89	$1.9\cdot10^{7}$	$2.3\cdot10^{6}$	4000
230	164	$7\cdot10^{-8}$	0.92	$1.3\cdot10^{7}$	$1.1\cdot10^{6}$	4500
220	164	$8\cdot10^{-8}$	0.95	$1.2\cdot10^{7}$	$6.3\cdot10^{5}$	5000

[1] k_{ij}: rate constant for transition j → i, jump angle $\Delta\varphi_\beta = 109°$.

(iii) The experimental spin-lattice relaxation data presented below display a strong temperature and pronounced angular dependence (T_{1Z}, T_{1Q} anisotropy), and are therefore a very sensitive tool for the examination of the kinetic properties for the guest molecules.

5.2.3 ^{2}H spin-lattice relaxation data (T_{1Z} and T_{1Q})

The guest dynamics were examined in a quantitative way by spin-lattice relaxation experiments comprising both samples with selectively deuterated guest molecules. For an isolated I = 1 nucleus, two linear combinations of the eigenstate populations (zero-quantum elements) define the Zeeman and quadrupolar order which decay with time constants T_{1Z} and T_{1Q}, respectively. The spin-lattice relaxation rates $1/T_{1Z}$ and $1/T_{1Q}$ depend on the molecular motion responsible for spin relaxation via the spectral densities $J_n(n\omega_0)$, as given earlier by Eqs. (3.87) and (3.88) [150, 186].

Both spectral densities $J_1(\omega_0)$ and $J_2(2\omega_0)$ depend on the time-scale and type of the underlying motional process which yields a distinct angular dependence for the spectral densities and relaxation times T_{1Z} and T_{1Q}. In polycrystalline solids, the anisotropy of T_{1Z} and T_{1Q}, extracted from the corresponding partially relaxed spectra [4, 7, 129, 144, 177], can be further exploited to examine the quality of the model assumptions during the experimental relaxation data analysis.

The experimental T_{1Z} data from inversion recovery experiments are given in Figure 5.21. The T_{1Z} values are powder values and were derived from the analysis of FID intensities from the inversion recovery experiments. It can be seen that the T_{1Z} curves display a shallow minimum of 8.8 ms for the α-deuterons and 7.9 ms for the β-deuterons at 310 K. Moreover, the slope above the T_{1Z} minimum appears to be somewhat smaller than for the low temperature range.

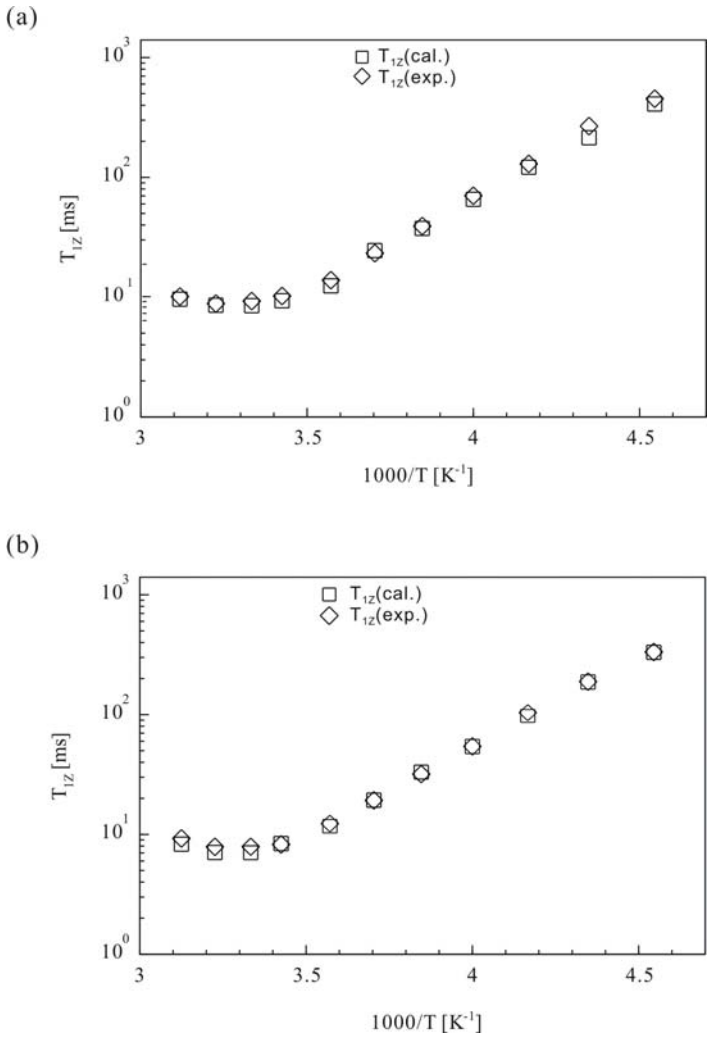

Figure 5.21 Experimental and theoretical T_{1Z} data as a function of temperature for (a) α-deuterons and (b) β-deuterons in 1,6-dibromohexane/urea.

Experimental partially relaxed ^{2}H NMR spectra, obtained from the inversion recovery experiment at 260 K, are given in Figures 5.22a and 5.22b for the samples with 1,6-dibromhexane deuterated at the α- and β-positions, respectively. The experimental data sets are contrasted with the theoretical counterparts, which were obtained by means of the simulation programme described in the experimental part, in general exhibit a very good agreement, supporting the quality of the underlying model assumptions. The same analysis of the partially relaxed spectra was done for the other points of the experimental T_{1Z} curve displayed in Figure 5.21.

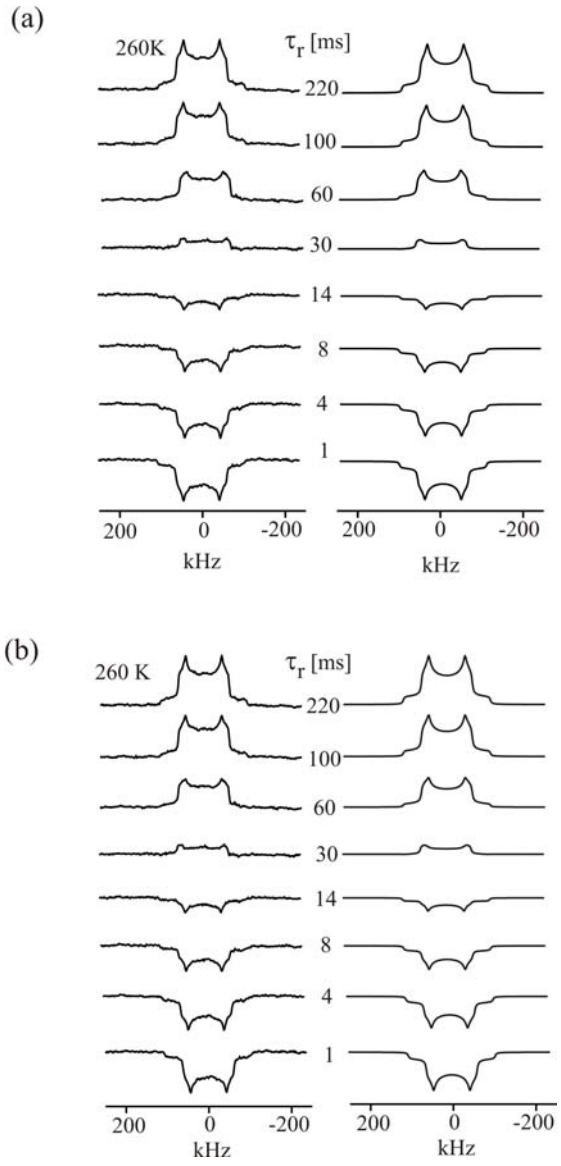

Figure 5.22 Partially relaxed ^{2}H NMR spectra from inversion recovery experiments at 260 K (left: experiment, right: simulation) on (a) 1,6-dibromohexane-1,1,6,6-d_4/urea and (b) 1,6-dibromohexane-2,2,5,5-d_4/urea.

At this stage we also underwent attempts to describe the guest motions by other motional models (eg. degenerate and non-degenerate 2- and 3-site jumps at variable opening angles). However, none of them provided a consistent description of all available experimental data. In particular, as shown by several other applications, the T_{1Z} anisotropy was found to be very sensitive for type and time-scale of the molecular motions.

It should be noted that during this part of the data analysis the same values for the quadrupolar coupling constant, populations and jump angles were used as before during the ^{2}H NMR line shape analysis (see Tables 5.12 and 5.13). The only adjustable variable was the motional correlation time τ_c, which is related to the rate constants k_{12} and k_{21} by equation (5.5).

$$\frac{1}{\tau_C} = \frac{k_{12}}{p_1} = \frac{k_{21}}{p_2} \tag{5.5}$$

Here, k_{ij} represents the pseudo first-order rate constant for the transition from site j to site i with the populations p_i. The rate constants k_{12} and k_{21}, derived from the simulations of the partially relaxed spectra of the inversion recovery experiments, are plotted in Figure 5.23 as a function of the reciprocal temperature. In the Arrhenius representations discontinuities at around 300 K are observed which stem from the fact that the experimental and theoretical T_{1Z} values at the T_{1Z} minimum do not match. That is, the values of the theoretical T_{1Z} minimum were somewhat lower than those for the experimental T_{1Z} minimum. The only way to reproduce the experimental data was by shifting the correlation times to smaller values which then gave rise to the discontinuity in the Arrhenius plots.

Inspection of Table 5.14 reveals that practically the same kinetic parameters were achieved, independent of particular deuterated samples. In this context, it should be emphasized that a completely independent data analysis of both deuterated samples was made. Hence, activation energies $E_{a,12}$ of 20.0 kJ/mol (deuterated α-position) and 19.1 kJ/mol (deuterated β-position) were found below the T_{1Z}-minimum, while $E_{a,12}$ = 6.7 kJ/mol (deuterated α-position) and 11.2 kJ/mol (deuterated β-position) were derived above the T_{1Z}-minimum. The difference ΔH of about 12 kJ/mol between the two activation energy values is somewhat higher than the value of about 9 kJ/mol derived from the temperature dependence of population p_1 (see above).

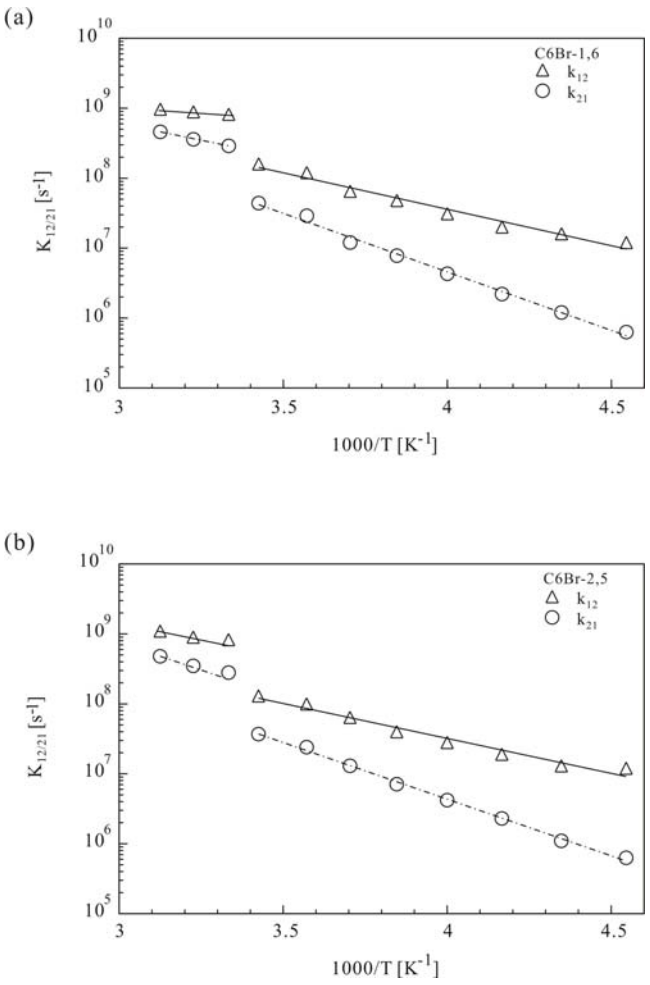

Figure 5.23 Arrhenius representation for rate constants of the gauche-gauche interconversion in 1,6-dibromohexane/urea (C6Br-1,6: 1,6-dibromohexane-1,1,6,6-d_4/urea, C6Br-2,5: 1,6-dibromohexane-2,2,5,5-d_4/urea).

For completeness a variable temperature T_{1Q} study was done for the same temperature range. The experimental T_{1Q} curves are depicted in Figure 5.24, while representative partially relaxed spectra along with their theoretical counterparts are given in Figure 5.25. The experimental T_{1Q} data were calculated from the intensities of the perpendicular singularities, and were obtained by a two-parameter fit using Eq. (3.64) [19]. From the experimental T_{1Q} data, minimum values of 11.2 and 9.3 ms for the α- and β-deuterated samples, respectively, were derived at 300 K.

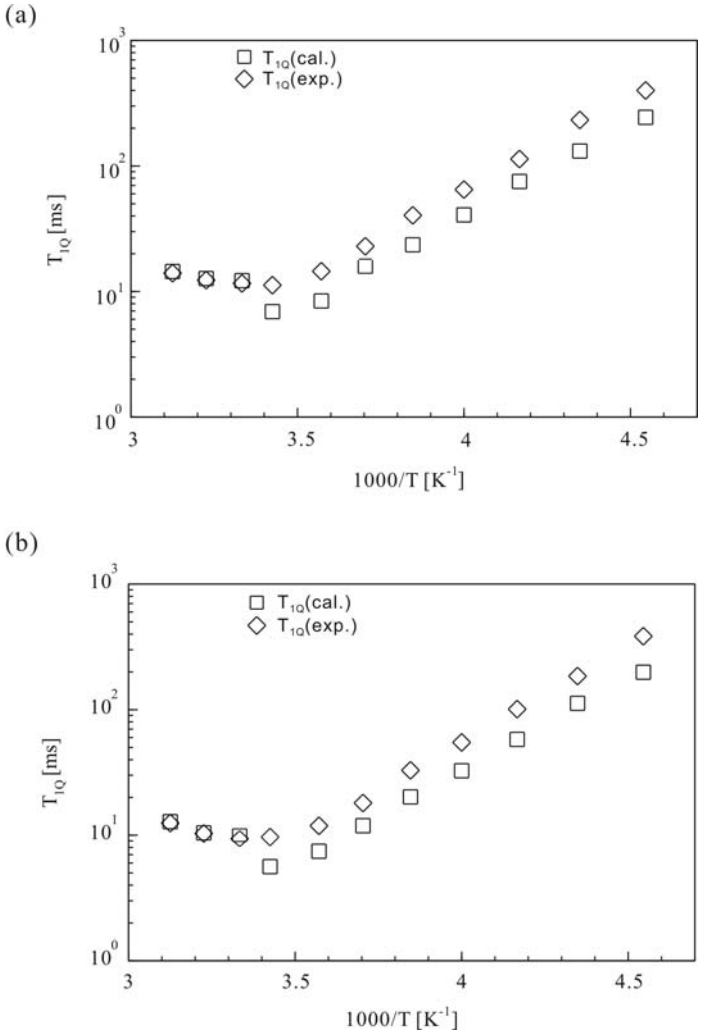

Figure 5.24 Experimental and theoretical T_{1Q} data as a function of temperature for (a) α-deuterons and (b) β-deuterons in 1,6-dibromohexane/urea.

As can be deduced from the representative spectra in Figure 5.25, in general a very satisfactory reproduction of the experimental data can be achieved which also holds for the reproduction of the experimental T_{1Q} values, given in Figure 5.24. In fact, the T_{1Q} analysis yielded the same simulation parameters, given in Tables 5.12 and 5.13, as obtained from the aforementioned T_{1Z} data analysis.

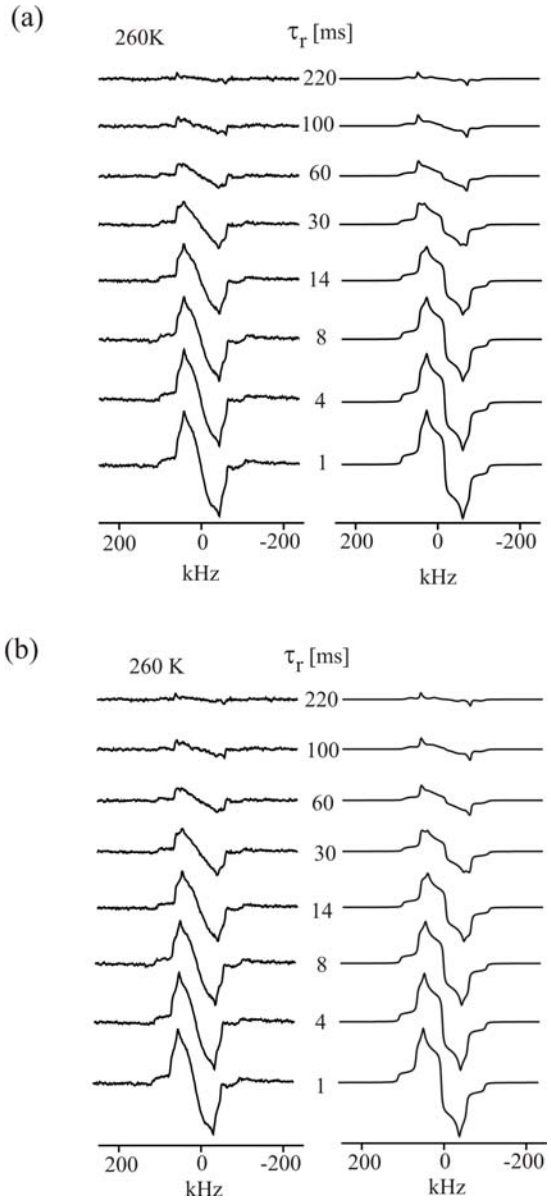

Figure 5.25 Partially relaxed ^{2}H NMR spectra from BBJB experiments at 260 K (left: experiment, right: simulation) on (a) 1,6-dibromohexane-1,1,6,6-d_4/urea, and (b) 1,6-dibromohexane-2,2,5,5-d_4/urea.

5.2.4 Discussion

The present ^{13}C, ^{1}H and ^{2}H NMR study provides a consistent picture for the molecular properties of the 1,6-dibromohexane/urea inclusion compound. The observed strong alterations of the ^{13}C and ^{1}H chemical shifts for the guest molecules upon enclathration clearly point to changes in conformational order, although an influence

by interactions with the urea host lattice also plays some role. The examination of samples with deuterated and non-deuterated urea clearly demonstrates that strong dipolar interactions exist between the guest and host components which is also expressed by an enhanced ^{1}H spin diffusion (shorter ^{1}H $T_{1\rho}$ values) for the non-deuterated sample. Furthermore, it is shown that there exist substantial differences between the ^{13}C and ^{1}H NMR data for the UICs with 1,6-dibromohexane and the long-chain analogue 1,10-dibromodecane. Primarily, they arise from structural differences of the urea lattices which in turn affect the guest mobility and conformational properties.

Table 5.14 Kinetic parameter for gauche-gauche interconversion of 1,6-dibromo-hexane-1,1,6,6-d_4 and 1,6-dibromohexane-2,2,5,5-d_4 in urea.

	1,6-dibromohexane-1,1,6,6-d_4			1,6-dibromohexane-2,2,5,5-d_4		
	$E_{a,12}$ [2]	$E_{a,21}$ [2]	ΔH [2]	$E_{a,12}$ [2]	$E_{a,21}$ [2]	ΔH [2]
	[kJ/mole]			[kJ/mole]		
HT[1]	6.7 ± 0.3	18.4 ± 0.7	11.7	11.2 ± 2.5	21.5 ± 2.8	10.3
LT[1]	20.0 ± 1.3	32.0 ± 1.0	12	19.1 ± 1.3	31.0 ± 0.6	11.9
	A_{12} [3]	A_{21} [3]		A_{12} [3]	A_{21} [3]	
		[s^{-1}]			[s^{-1}]	
HT[1]	1.5×10^{10}	4.7×10^{11}		6.7×10^{10}	1.5×10^{12}	
LT[1]	5.3×10^{11}	2.0×10^{12}		3.1×10^{11}	1.3×10^{13}	

[1] LT: temperature range below relaxation minimum; HT: temperature range above relaxation minimum

[2] $E_{a,ij}$: activation energy for jump from site j to i, ΔH: activation energy difference.

[3] preexponential factors

There is strong evidence that ^{13}C spin-lattice relaxation is caused by the same motional contributions which are responsible for ^{2}H spin-lattice relaxation. This is

born out by the similar temperature dependence of the relaxation curves, and the results from the semi-quantitative analysis of the ^{13}C T_1 data providing similar motional correlation times as derived from the quantitative ^{2}H T_1 data analysis discussed next.

It should be noted that recently a comprehensive ^{13}C NMR relaxation study for a series of n-alkane/UICs was published [187]. It was shown that the ^{13}C T_1 values are almost independent of the particular chain length, and vary with the chain position. Both results were attributed to the overall and internal chain mobility, as also verified, for instance, by variable temperature ^{2}H NMR studies on n-alkane/UICs [5-7].

Reliable information about the guest mobility is obtained from the analysis of the variable temperature ^{2}H NMR data. It could be demonstrated that the experimental ^{2}H NMR line shapes, T_{1Z} and T_{1Q} data are reproducible by a single parameter set (quadrupolar coupling constants, jump angles, site populations) which again emphasizes the quality of the underlying motional model of mutual exchange between two non-degenerate gauche states, as proposed during an earlier NMR work. However, the time-scale of this motional process must lie in the sensitive range of spin-lattice relaxation, and not – as proposed earlier – within the time-scale of line shape effects [8]. Therefore, considerably shorter correlation times (by about one two orders of magnitude) are obtained in the present work.

In summary, it is the commensurability of the 1,6-dibromohexane guest and the urea host substructures, resulting in a monoclinic crystal structure, which gives rise to larger spatial constraints on the guest species and stabilizes the gauche conformational states. In quite contrast, UICs with the long-chain analogues $C_nH_{2n}Br_2$ (n = 10, 11) or n-alkanes are characterized by hexagonal channels in which the guests adopt a nearly all-trans conformational state. The latter guests undergo almost unhindered rotational motions around their long axes, while for the 1,6-dibromohexane guests restricted overall reorientation between two gauche conformations are registered along with a

large activation energy. The nearly identical activation energies of $E_{a,12}$ = 20.0 kJ/mol and 19.1 kJ/mol for the α-and β-deuterons, respectively, below the T_{1Z} minimum clearly demonstrate that the underlying motional process affects the guest molecules as a whole. In quite contrast, for n-hexadecane (12.4 kJ/mol, six-site rotational motions, high temperature phase) [7] and n-nonadecane (8.4 kJ/mol, rotational diffusion) [6] in urea, a low sterical hindrance for the overall rotation is discussed. For alkanes with branched end-groups [177], due to the spatial requirement of the larger end groups, a slightly larger activation energy of 16.7 kJ/mol is reported. For carboxylic acids [4] also larger activation energies are found which are attributed to both interactions between adjacent guest molecules (hydrogen bonding) and between guest species and urea host lattice.

The differences in sterical hindrance are also manifested in the absolute rate constants. Thus, the rate constants for guest motions for 1,6-dibromohexane/urea are found to be several orders of magnitude smaller than those reported for n-alkanes, branched alkanes or long-chain dibromoalkanes incorporated in hexagonal urea channels [5-7, 176, 177].

In connection with the present T_{1Z} and T_{1Q} data analysis it is worth mentioning that the anisotropy of these relaxation times is very useful for the discrimination between different motional models. That is, although it might be possible to reproduce the experimental fast exchange ^{2}H NMR line shapes by different data sets, the corresponding T_{1Z} and T_{1Q} anisotropies – as directly reflected by the line shape alterations of the partially relaxed spectra as a function of the relaxation interval τ_r – strongly vary with the underlying motional model. For instance, in the case of a 2-site jump model it is always possible to describe a fast exchange spectrum by degenerate or non-degenerate jump processes; the only difference would be the jump angle. The corresponding anisotropies of the relaxation times, however, show completely different behavior and can be clearly discriminated.

The discontinuities in the Arrhenius plots around the minima of spin-lattice relaxation curves, resulting in two different slopes above and below the T_1 minima, are addressed next. As mentioned earlier, at first sight they can be traced back to the fact that the theoretical minima of the relaxation curves (based on the assumption of a gauche-gauche interconversion process) are lower than their experimental counterparts. Attempts were therefore made to overcome these discrepancies. Hence, a distribution of correlation times was considered. Likewise, the quadrupolar coupling constant was reduced, and the site populations and jump angles were varied. None of these attempts were successful, since they gave rise to considerable deviations between the experimental and theoretical ^{2}H NMR line shapes. Therefore, these options were not considered any further.

On the other hand, the discontinuities in the Arrhenius plots are surprising, since calorimetric studies do not show any phase transition in this temperature range. However, due to the continuous change of the urea lattice structure [55], the guest molecules might have gained enough spatial freedom that at about room temperature the gauche-gauche interconversion is suddenly accelerated. This assumption is supported by the observation that overall molecular fluctuations, as reflected by the reduction of the quadrupolar coupling constant and by the ^{13}C $T_{1\rho}$ data (see below), also play an important role at higher temperature. Similar discontinuities for the guest overall motions are also observed for other guest-host systems, although first-order phase transition could not be observed [188].

The gain in spatial freedom is also reflected by the lower activation energy above the discontinuity. Likewise, there is evidence for lateral diffusion of the guests at higher temperatures which also requires sufficient spatial freedom. The presence of lateral motion is indirectly visible by an isotropic signal in the ^{2}H NMR spectra at elevated temperatures which stems from free, non-clathrated 1,6-dibromohexane escaped from the urea lattice. As mentioned earlier, free non-clathrated 1,6-dibromohexane can be also deduced from ^{1}H MAS spectra of samples spun at 34 kHz.

^{13}C $T_{1\rho}$ relaxation is assumed to be caused by overall fluctuations of the guest molecules. This assumption is supported by the increase of ^{13}C $T_{1\rho}$ towards the center of the alkyl chains. That is, the fluctuations are more efficient for the chain ends giving rise to shorter ^{13}C $T_{1\rho}$ values. Moreover, the reproduction of the overall experimental ^{2}H spectral widths required smaller quadrupolar coupling constants (see Table 5.12 and 5.13) at higher temperatures. This effect is more pronounced at the chain ends than in the center of the chains which again gives strong evidence that the reduction in overall spectral width stems from fast overall fluctuations.

The amplitude of guest wobbling is extremely sensitive to the channel diameter [189], and becomes larger if the channel is allowed to deform. X-ray studies [55] have demonstrated that the guest molecules coil into gauche conformations and tilt away from the channel axis by about 12 to 14°. The net result is that the host channel experiences a lattice strain arising from the internal stress due to the guest molecules, and gradually shifts from a monoclinic toward hexagonal symmetry upon temperature increase [8, 55] along with enhanced fluctuations of the guest molecules.

In summary, the correlation times for overall fluctuations are about one order of magnitude smaller than the values for gauche-gauche interconversion. The actual activation energies for the non-deuterated UICs are about 10 kJ/mol, and 20 kJ/mol for the deuterated UICs (see Table 5.10). The stronger temperature dependence for the guest fluctuations in the deuterated UIC can be explained by weaker hydrogen bonds and a reduced host lattice stability. As a consequence, a stronger temperature dependence is found for the guest fluctuations.

The theoretical description of the ^{2}H NMR line shapes required a temperature dependent residual line width $1/T_2^0$ (see Tables 5.12 and 5.13). This line width reduction with increasing temperature can be attributed to a reduction of the heteronuclear dipolar interactions between guest molecules and host matrix due to the increasing guest mobility and/or the temperature dependent increase of the channel

diameter (see also former discussion of ^{13}C NMR line widths and ^{2}H NMR relaxation data). Similar temperature dependent changes of the residual NMR line widths have been reported for other systems [7, 176].

5.2.5 Conclusions

The molecular properties of 1,6-dibromohexane in its urea inclusion compound are investigated by means of a multinuclear solid-state NMR spectroscopy. ^{13}C CP/MAS and ^{1}H MAS NMR studies (line shapes, spin-lattice relaxation measurements) were performed for the first time to probe the guest dynamics and conformational order. Variable temperature ^{2}H NMR studies comprising line shape analysis as well as spin-lattice relaxation (T_{1Z}, T_{1Q}) experiments were done on samples with guest molecules selectively deuterated at two different positions. A quantitative analysis of the experimental data proves that the guest dynamics are dominated by mutual exchange between two gauche conformers. It is shown that these guest motions unequivocally can be quantified (type and time-scale) by a comprehensive analysis of the T_{1Z} and T_{1Q} data. In addition, there is evidence that other motional contributions, such as overall molecular fluctuations and lateral motions, also contribute to spin relaxation. The molecular behaviour of 1,6-dibromohexane in urea is completely different from that reported for the long chain analogues or for n-alkanes where typically unhindered overall rotational motions of the guests in their all-trans conformation around the urea channel long axis are discussed. The differences in guest ordering and dynamics are a direct consequence of the differences of the urea lattice structures (monoclinic vs. hexagonal urea lattice).

5.3 1-bromodecane/urea inclusion compounds

Variable temperature ^{2}H NMR spectroscopy was carried out between 120 K and room temperature on urea inclusion compounds with 1-bromodecane selectively deuterated

at the end CH_2Br group (see Fig. 5.26). Solid-state ^1H MAS and ^{13}C CP MAS NMR studies were performed for the inclusion systems of non-deuterated guest species. Differential scanning calorimetry shows that the phase transition arising from the distortion of the urea channel for 1-bromodecane/urea occurs at ca. 133 K. The phase transition temperature is lower than for 1,10-dibromodecane/urea with a value of 141 K [23, 53, 176] and higher than the value for n-decane/urea inclusion compounds for which a phase transition temperature of 111 K is found [23, 85]. Obviously, the solid-solid phase transition is shifted to higher temperature with increasing number of Br substituents. This implies that the change in urea crystal symmetry from the orthorhombic to the hexagonal form, established by x-ray diffraction [23, 77, 85], is affected by the Br substituent, most probably due to an increase of intermolecular interactions between the guest and host as well as guest and guest species.

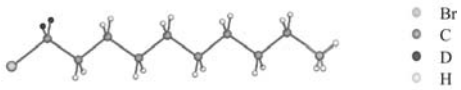

Figure 5.26 Chemical structure of 1-bromodecane selective deuterated at the bromated methylene group.

5.3.1 ^1H MAS and ^{13}C CP/MAS NMR measurements

Figure 5.27 depicts ^1H MAS (top trace) and ^{13}C CP/MAS (bottom trace) NMR spectra of 1-bromodecane/urea. The ^{13}C spectrum displays two resonances at 15.6 and 15.3 ppm for the CH_3 group, whereas the resonances from other carbons within the molecule appear as single peaks. For asymmetric guest molecules $X(CH_2)_nY$ in urea inclusion compounds, the two different chemical shift values of the terminal groups are attributed to different arrangements. It was first demonstrated by Hollingsworth et al. [57, 58] that the terminal groups of the asymmetric guest molecules can be aligned in terms of head-to-head, tail-to-tail and head-to-tail. Based on a former report on 1-fluorotetradecane/urea inclusion compounds [103], it is concluded that the resonance at 15.6 ppm reflects $CH_3…H_3C$ end-group environment while the

resonance at 15.3 ppm results from the $CH_3…BrH_2C$ end-group environment. The intensity ratio of the two resonances is found to be 1:1, which indicates that for a given CH_3 (or CH_2Br) group, there is an equal chance of having either CH_3 or CH_2Br as a neighbour - neither alignment is more preferable over the other.

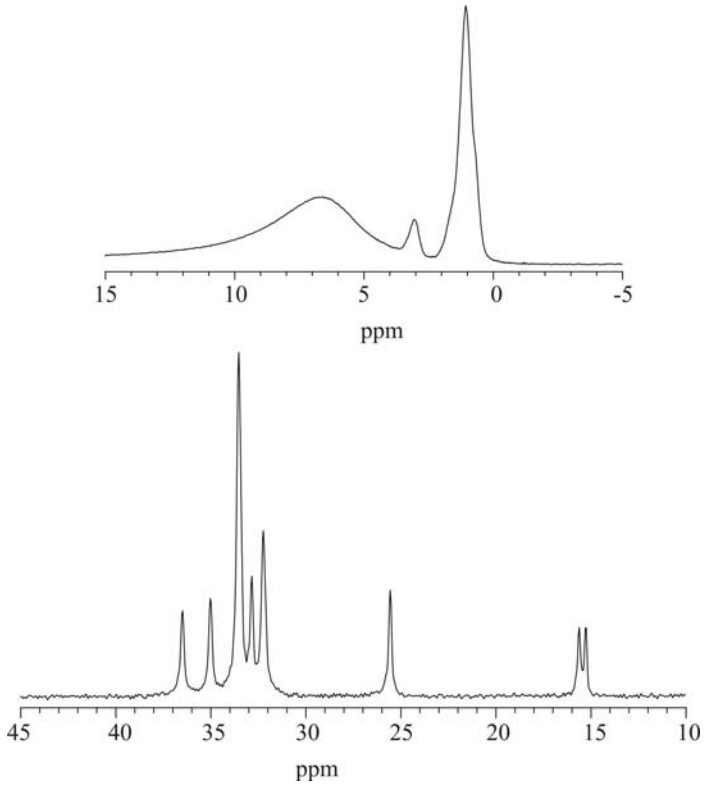

Figure 5.27 ^{1}H MAS (top trace) and ^{13}C CP/MAS (bottom trace) NMR spectra of 1-bromodecane/urea.

Cross-polarization was used for ^{13}C NMR spectra recording to improve the signal/noise ratio. In general, the decay of the ^{13}C signal as a function of contact time is determined by ^{1}H $T_{1\rho}$ [163, 164]. In order to assess whether the $CH_3…H_3C$ and $CH_3…BrH_2C$ peak intensities (the ratio of 1:1) relate to the populations of the different sites, ^{13}C CP MAS NMR spectra are recorded as a function of contact time ranging from 0.5 to 10 ms. The ratio of 1:1 between the two resonances at 15.6 and 15.3 ppm respectively is obtained for all contact times, which clarifies that the relative intensities of the two end CH_3 group peaks are consistent with the ratio of

aforementioned 1:1 of the CH_3…H_3C and CH_3…BrH_2C arrangements [58, 190].

Likewise, for the CH_2Br end-group, two different environments of CH_2Br…H_3C and CH_2Br…BrH_2C arrangements should co-exist. Thus, it is expected that two different resonances corresponding to these two arrangements should be observed. However, only one distinguishable resonance is recorded. This finding indicates a dominant influence of the directly bonded Br substituent on the chemical shift values while the interaction with CH_3 and CH_2Br groups are of minor importance. It is because of the longer C-Br bond (1.96 Å [22]) than the C-H bond (1.09 Å [191]) that CH_3 and CH_2Br end groups could not approach the carbon of the CH_2Br as closely as for the CH_3 group. Thus the carbon nucleus of the end CH_2Br group cannot feel the alternation of the electronic environments resulting from CH_2Br…H_3C and CH_2Br…BrH_2C arrangements. Therefore, only one resonance at 36.5 ppm for CH_2Br end-group can be resolved.

According to previous studies of urea inclusion compounds containing n-alkanes with a terminal functional group [11, 103], the assignments of ^{1}H MAS and ^{13}C CP/MAS resonances are listed in Tab. 5.15 along with the chemical shifts of the corresponding guest molecules in solution. It is found that the packing effect is responsible for the downfield shift of the ^{13}C resonances of the guest molecules if compared with the signals in solution [11, 192]. The downfield shift of about 2.5 ppm for CH_2Br carbon resonance is consistent with the presence of an all-trans conformation for the guest molecules in urea and mutual exchange between the gauche and trans conformation in solution [9, 23, 34, 36, 38, 193, 194].

^{1}H MAS spectra of 1-bromodecane in urea exhibit a much lower resolution due to the strong ^{1}H dipolar coupling. Only two peaks are observed, corresponding to the protons of CH_2Br and the others within the molecules. It is the strong ^{1}H spin diffusion that gives rise to the same ^{1}H $T_{1\rho}$ values of each hydrogen (with exception

of CH_3 which has a smaller ^1H $T_{1\rho}$ value due to the end methyl rotation [7, 20, 23]) along the chain, as listed in Tab. 5.16. Table 5.16 also gives the temperature-dependent ^{13}C $T_{1\rho}$ data. In general, the ^{13}C $T_{1\rho}$ data of the carbons within the chain increase with rising temperature, which indicates that the undergoing motions are on the high temperature branch of the relaxation curve. It will be shown below that the rotation of the guest molecules along the channel axis is very fast, thus is not expected to affect ^{13}C $T_{1\rho}$. ^{13}C $T_{1\rho}$ value decreases towards the center of the chain, which might reflect that overall guest fluctuation motion, being sensitive to the change of the position between the guests and hosts, dominates ^{13}C relaxation in the rotating frame.

Table 5.15 NMR parameters from ^{13}C and ^1H NMR studies on 1-bromodecane in solution and UICs.

$C_{10}H_{21}Br$	δ_{13C} [ppm]		$C_{10}H_{21}Br$	δ_{1H} [ppm]	
CT: 1.5ms	solution[a]	urea[b]		solution[c]	urea[d]
C1+Br	33.8	36.5	H1+Br	3.4	3.5
C2	33.0	35.0	H2	1.8	1.5
C3-4	28.9-28.3	32.2	H3	1.5	1.5
C5-C7	29.5-29.4	33.5	H4-9	1.3	1.5
C8	32.0	32.9	H10	0.9	1.1
C9	22.7	25.6			
C10…CH_3	14.1	15.6			
C10…BrH_2C	14.1	15.3			

[a] ^{13}C chemical shifts of 1-bromodecane in $CDCl_3$ [192].

[b] ^{13}C chemical shifts of 1-bromodecane in their UICs derived in this work from ^{13}C CP/MAS studies.

[c] ^1H chemical shifts of 1-bromodecane in $CDCl_3$ [181].

[d] ^1H chemical shifts of 1-bromodecane in their UICs derived in this work from ^1H MAS experiments.

Table 5.16 $T_{1\rho(13C)}$ and $T_{1\rho(1H)}$ data for the $C_{10}H_{21}Br$ in urea.

$C_{10}H_{21}Br$	$T_{1\rho(13C)}$ [ms]				$T_{1\rho(1H)}$
(CT[a]: 1.5m)	294K	300K	310K	320K	[ms][b]
C-1	196	193	200	268	13
C-2	195	198	232	292	13
C-3,4	190	195	195	258	14
C-5,7	182	186	190	232	14
C-8	200	194	225	337	14
C-9	252	254	257	322	13
C10…CH_3	249	279	262	425	8.8
C10…BrH_2C	298	227	209	298	9.0

[a] contact time

[b] value at 294 K

5.3.2 ^{2}H NMR line shapes and spin-spin relaxation data

The temperature-dependent ^{2}H NMR line shapes, shown in Fig. 5.28, were recorded between 120 K and room temperature for 1-bromodecane/urea inclusion compounds. The spectrum at 120 K is typical for a static powder pattern, with a 116 kHz splitting between the two perpendicular singularities.

Upon sample heating, characteristic variations of the line shapes are observed, indicating that dynamic processes occur with rate constants in the order of the quadrupole coupling constant. Above 160 K, the line shapes are found to be independent of temperature, suggesting that the motion enters the fast exchange limit. Thus, the splitting of the perpendicular singularities remains constant with a value of 52 kHz.

In two former studies [53, 176] it was found that the spectrum of 1,10-dibromo-decane/urea inclusion compounds has a greater splitting of 124 kHz at 120 K and is

somewhat narrower with a value of 46 kHz at room temperature between the two perpendicular singularities.

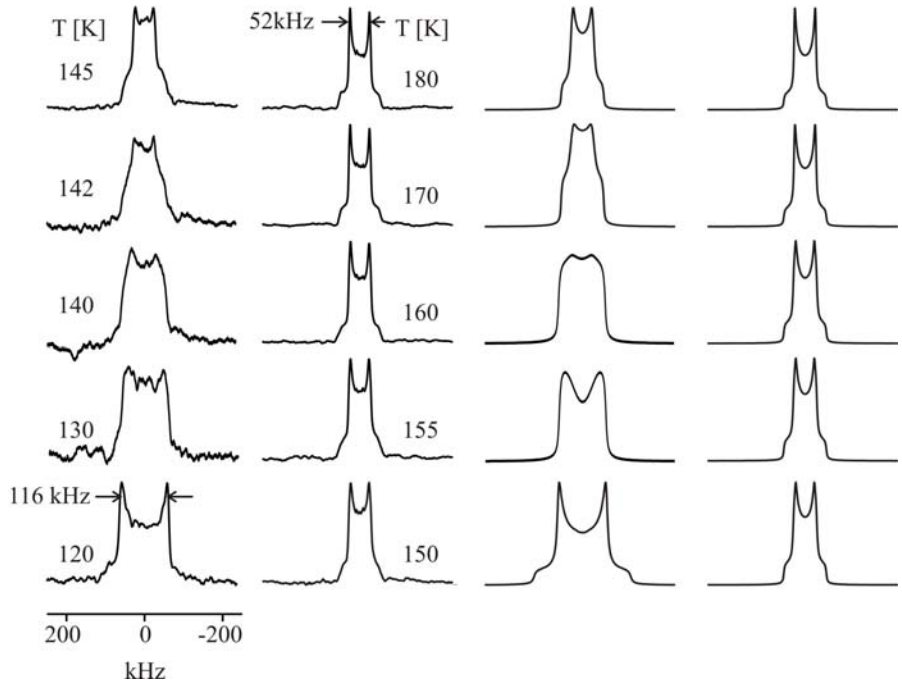

Figure 5.28 Variable temperature ^{2}H NMR line shapes of 1-bromodecane-1,1-d_2 in urea (left: experiment, right: simulation).

The 1-bromodecane guest molecule is constrained in the urea channel and exists in the all-trans conformation [9, 34, 193, 194]. The angle between each C-D bond and the channel axis is therefore 90°, assuming ideal tetrahedral angles. To account for the dynamic properties of the guest molecules, various types of motional models were examined. Numerous theoretical simulations have shown that a three-site jump model combined with an overall chain small angle fluctuation can be used to interpret the motion of the guest molecules investigated. Due to the C_6 symmetry of the urea channel, 6-site jump model is more realistic for the guest motion. Because 3- and 6-site models cannot be distinguished, all simulations were done with the 3-site jump model.

For the 3-site jump model (see Fig. 5.29), the angle θ between the rotation axis and the C–D bond is set to 90° and the azimuthal angle $\Delta\phi$ among the jump sites is −120°, 0° and 120°, respectively. Two sites have identical fractional populations denoted by p_2 and p_3, respectively, which in most general case are different from the population denoted by p_1 of the unique site 1 which has a minimum potential, i.e. $p_2 = p_3 \neq p_1$, and the summation of the populations of all the three sites is unity ($p_1 + p_2 + p_3 = 1$).

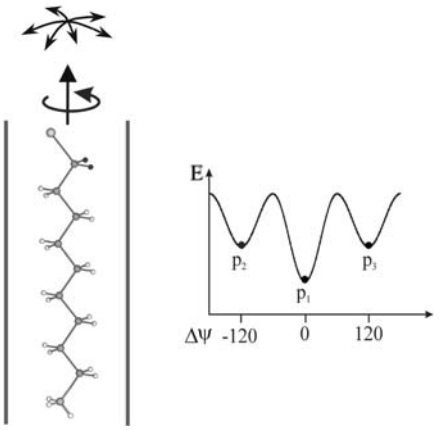

Figure 5.29 Possible motions of the guest molecules in urea and schematic drawing of 3-site jump motion model.

The simulated line shapes are presented in Fig. 5.28 as well. A best-fit reproduction of the experimental spectrum at 120 K is obtained for the static case with a quadrupole coupling constant of 165 kHz and an asymmetry parameter $\eta = 0$. In order to get the good reproduction of the experimental spectra, the quadrupole coupling constant was slightly reduced at elevated temperatures. Above the phase transition, a value of 145 kHz is used. This can be attributed to the occurrence of a fluctuation motion. If the guest molecules undergo a rotational motion in the rapid motional regime (with symmetry $\geq C_3$), the ^{2}H NMR spectrum regains the axially symmetric Pake powder pattern line shape but its spectral width is half of that of the spectrum in the slow motional regime [7]. However, the experimental results demonstrate that the reduction of the spectral width is more than a factor of 1/2, the additional reduction is attributed to small-angle fluctuations perpendicular to the long molecular axis.

Sometimes, different models can result in the same motionally averaged line shape, but can be distinguished by a different pulse spacing dependence in the quadrupole echo experiments in the intermediate motional regime. Hence, if one motional model is thought to be suitable for a system, it should be possible to reproduce the line shapes as well as the pulse spacing dependence of the line shapes and the spin-spin (T_2) relaxation times. The experimental T_2 values (overall powder values) for the 1-bromodecane/urea are plotted in Fig. 5.30. Figure 5.31 exhibits two representative series of partially relaxed ^{2}H NMR spectra, at 130 K and 150 K, as a function of the pulse intervals in the quadrupole echo sequence along with the calculated counterparts derived from the assumed 3-site jump model. The theoretical partially relaxed ^{2}H NMR spectra are obtained with the same parameters (population, quadrupole coupling constant and correlation times) as used in the simulations of the ^{2}H NMR line shapes in Fig. 5.28. Clearly, the calculated partially relaxed spectra agree very well with the experimental results.

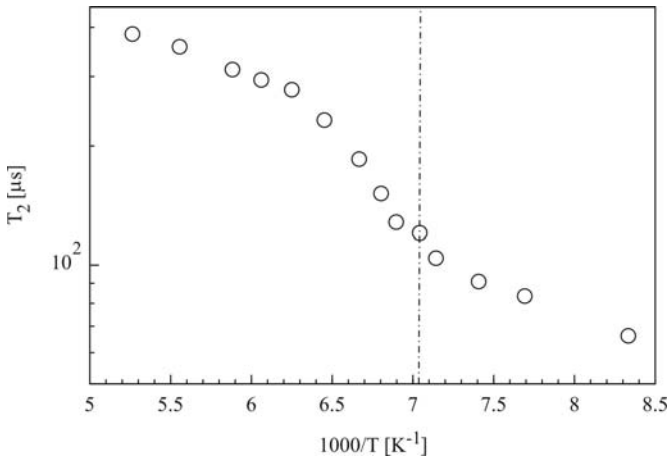

Figure 5.30 Experimental ^{2}H spin-spin relaxation data T_2 as a function of temperature for 1-bromodecane-1,1-d_2 in urea (dashed line denotes solid-solid phase transition).

The simulation of ^{2}H NMR line shapes and partially relaxed spectra provides the correlation times for the temperature below 160 K, as listed in Tab. 5.17. An Arrhenius plot of the correlation times for the 3-site jump motion of 1-bromodecane

in urea is shown in Fig. 5.32.

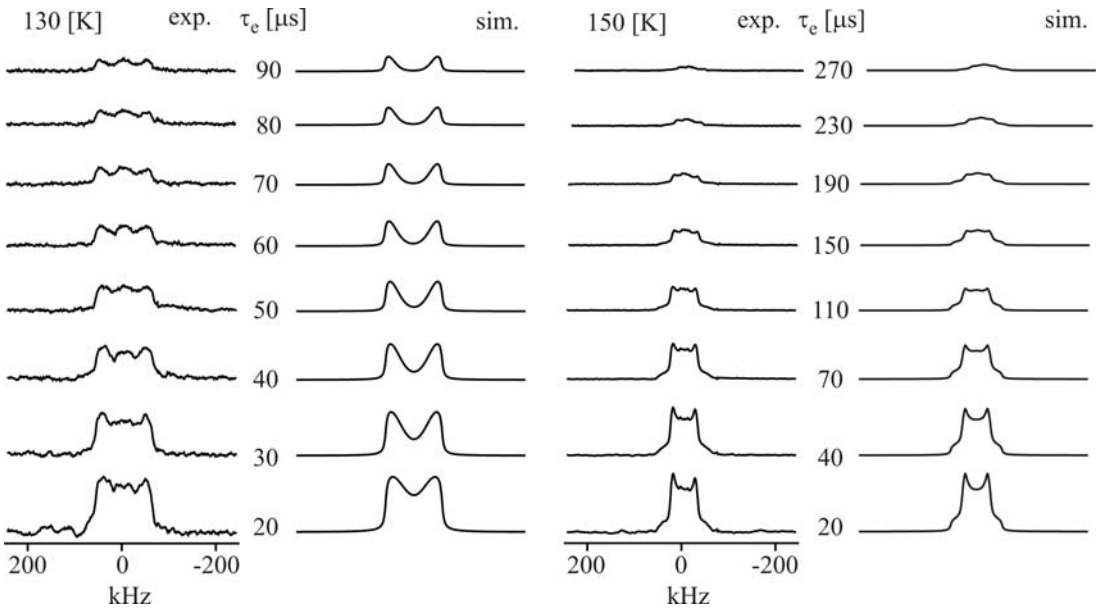

Figure 5.31 Experimental partially relaxed ^{2}H NMR spectra from quadrupole echo sequence at 130 K and 150 K. The theoretical simulations were done with correlation times $\tau_c = 6\times10^{-7}$ s (130 K) and $\tau_c = 2\times10^{-8}$ s (150 K).

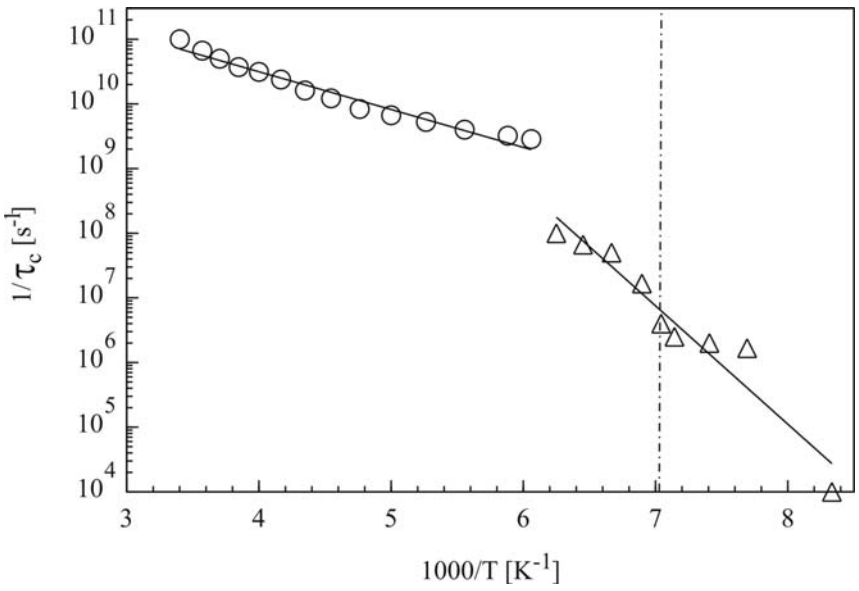

Figure 5.32 Arrhenius plots for the rotational motions of 1-bromodecane-1,1-d_2 in urea (dashed line denotes solid-solid phase transition).

5.3.3 ^{2}H spin-lattice relaxation data (T_{1Z} and T_{1Q})

If the undergoing motion is in the fast motional limit with correlation times from 10^{-7} to 10^{-12} s, the guest dynamics can be examined in a quantitative way by spin-lattice relaxation experiments.

The experimental and theoretical overall T_{1Z} data as a function of temperature are given in Fig. 5.33. A minimum value of 13.7 ms is recorded at 160 K and the two branches separated by the T_{1Z} minimum value exhibit different slopes. A representative series of partially relaxed ^{2}H NMR spectra measured at 290 K from inversion recovery sequence is shown in Fig. 5.34 together with their theoretical counterparts obtained with a jump rate of 1×10^{11} s^{-1}. The good agreement between the experimental and theoretical relaxation data and their anisotropies (visible in the partially relaxed spectra) indicates that the assumed motional model is suitable for the guest dynamics. The obtained correlation times for the temperature above 160 K are

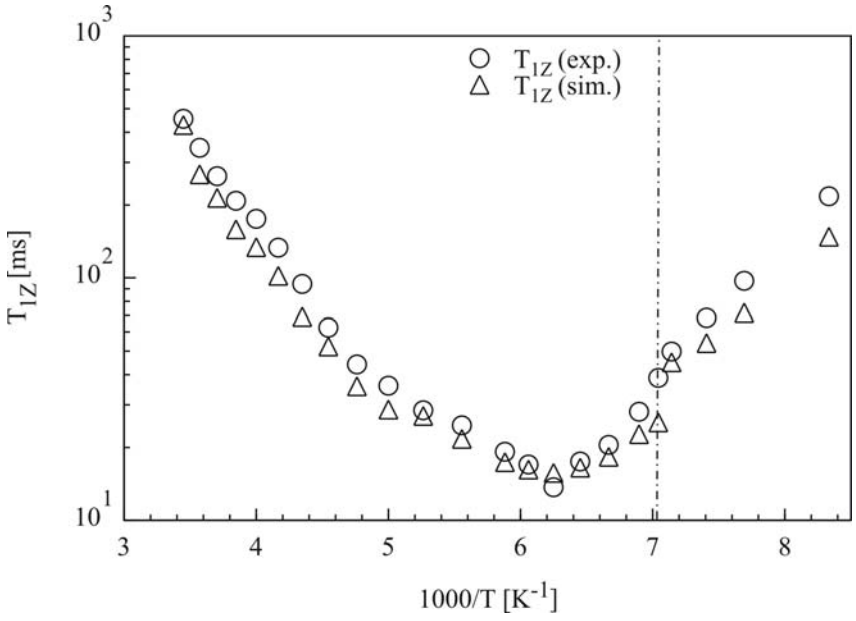

Figure 5.33 Experimental and simulated ^{2}H spin-lattice relaxation data T_{1Z} (Zeeman order) as a function of temperature (dashed line denotes solid-solid phase transition).

listed in Tab. 5.17 as well. It is worth mentioning that the theoretical T_{1Z} data for the temperature below 160 K are calculated with the same parameters used in the simulations of ^2H NMR line shapes and T_2 data.

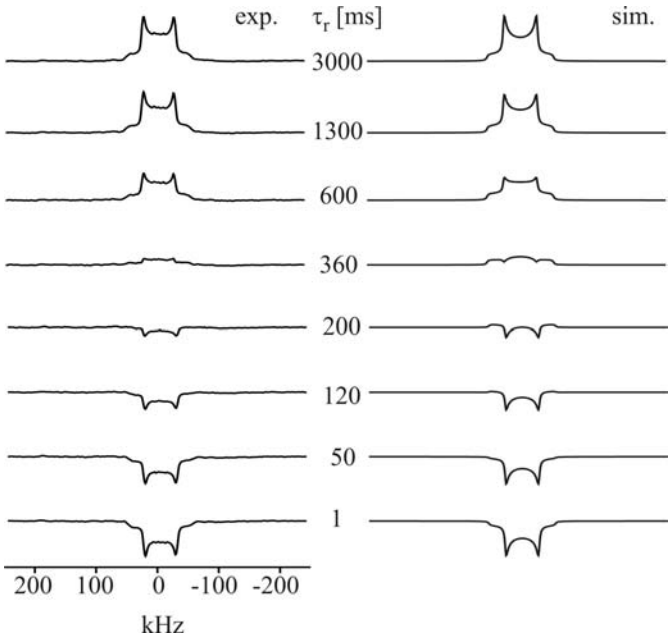

Figure 5.34 Experimental and theoretical partially relaxed ^2H NMR spectra from inversion recovery experiments at 290 K (correlation time $\tau_c = 1 \times 10^{-11}$ s).

A further independent proof for the chosen motional model is obtained from the variable temperature T_{1Q} data and partially relaxed ^2H NMR spectra (see Figs. 5.35 and 5.36). Again, the theoretical spectra and T_{1Q} values were derived by using the same simulation parameters as taken in T_{1Z} data analysis. The good reproduction of these later experimental data further supports the used 3-site jump model for the present system.

It should be emphasized again that for the simulations of the experimental data (including line shapes, T_2, T_{1Z} and T_{1Q}) shown above a single set of simulation parameters was used. The population of the major site was slightly changed in order

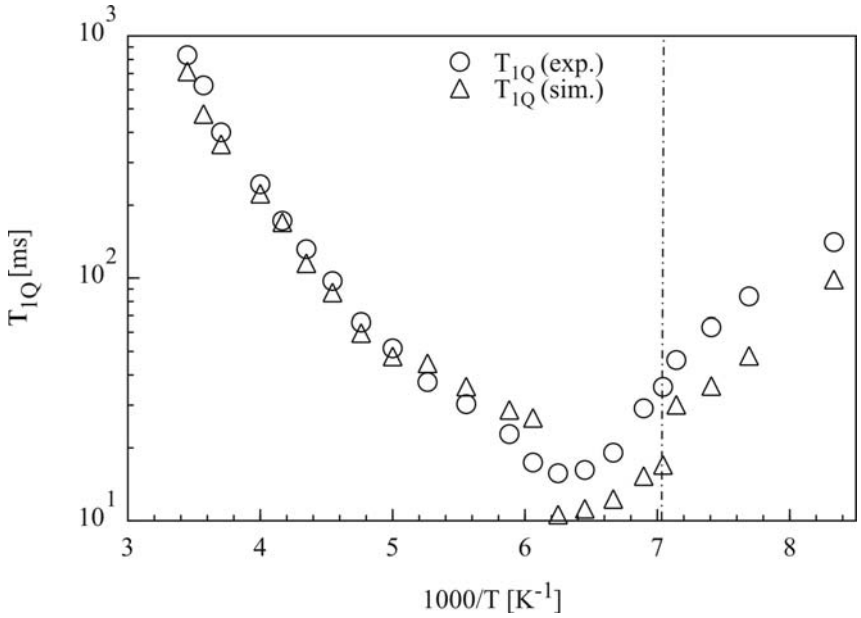

Figure 5.35 Experimental and simulated ^{2}H spin-lattice relaxation data T_{1Q} (quadrupolar order) as a function of temperature (dashed line denotes solid-solid phase transition).

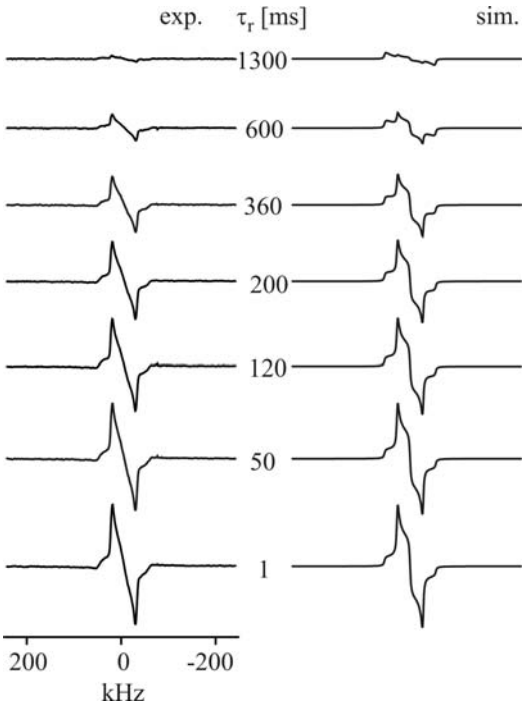

Figure 5.36 Experimental and theoretical partially relaxed ^{2}H NMR spectra from broadband Jeener-Broakaert experiments at 290 K (correlation time $\tau_c = 1 \times 10^{-11}$ s).

to fit the shape of the perpendicular singularities below 160 K. Here a value of 0.36 was necessary to match the slight inclination of the perpendicular singularities, while above 160 K a value of 0.33 has been taken. The line width ($1/T_2^0$) was varied from 5 kHz at 120 K to 2 kHz at 160 K, which can be attributed to a loss of the heteronuclear dipolar interactions between the guest molecules and the rigid urea matrix due to the increased mobility at higher temperature. Similar observations were reported previously [7, 176].

From the Arrhenius plot of the correlation times (see Fig. 5.32), for the high temperature phase an activation energy of 11 kJ/mole was determined, while 35 kJ/mole is derived for the low temperature phase, which correspond to the two different slopes of the high and low temperature phases separated by T_{1Z} and T_{1Q} minima at the T_{1Z} and T_{1Q} curves, respectively. When reproducing the experimental T_{1Z} and T_{1Q} values, it is found that the theoretical T_{1Z} and T_{1Q} minima (5.5 and 5.5 ms) do not match with the experimental ones (13.7 and 13.7 ms). That is, the values of the theoretical T_{1Z} and T_{1Q} minima were somehow lower than those for the experimental T_{1Z} and T_{1Q} minima. The only way to reproduce the experimental data was by shifting the correlation times to smaller values, therefore a discontinuity of the correlation time in Arrhenius plot is observed at the temperature corresponding to the T_{1Z} and T_{1Q} minima. This phenomenon was also reported for other systems [176, 188]. Attempts were made to overcome this discontinuity, for instance, by reducing the quadrupole coupling constant, varying the site population and using the distribution of the correlation time. However, none of these attempts were successful. Therefore, these options were not taken into account any further.

The discontinuity of the correlation time is therefore ascribed to the change of urea lattice structure and the type of the guest molecules. For n-alkane/urea inclusion compounds, this discontinuity takes place at phase transition temperature [7] where the average symmetry of urea channel structure changes from orthorhombic in low

Table 5.17 Simulation parameters for 1-bromodecane-1,1-d_2/urea.

Temperature T [K]	Quadrupole[1] coupl. const. e^2qQ/h^* [kHz]	Correlation time τ_c [s]	Population major site p_1	Line width $1/T_2^0$ [s^{-1}]
290	145	$1\cdot10^{-11}$	0.33	1500
280	145	$1.5\cdot10^{-11}$	0.33	1500
270	145	$2\cdot10^{-11}$	0.33	1500
260	145	$2.7\cdot10^{-11}$	0.33	1500
250	145	$3.2\cdot10^{-11}$	0.33	1500
240	145	$4.2\cdot10^{-11}$	0.33	1500
230	145	$6.2\cdot10^{-11}$	0.33	1500
220	145	$8.2\cdot10^{-11}$	0.33	1500
210	145	$1.2\cdot10^{-10}$	0.33	1500
200	145	$1.5\cdot10^{-10}$	0.33	1500
190	145	$1.9\cdot10^{-10}$	0.33	1500
180	145	$2.5\cdot10^{-10}$	0.33	1500
170	145	$3.1\cdot10^{-10}$	0.33	1500
165	145	$3.5\cdot10^{-10}$	0.33	1500
160	145	$1\cdot10^{-8}$	0.36	2000
155	145	$1.8\cdot10^{-8}$	0.36	2500
150	145	$2\cdot10^{-8}$	0.36	2500
145	145	$6\cdot10^{-8}$	0.36	2500
142	145	$2.5\cdot10^{-7}$	0.36	2500
140	145	$4\cdot10^{-7}$	0.36	3000
135	145	$5\cdot10^{-7}$	0.36	3500
130	160	$6\cdot10^{-7}$	0.36	4000
120	165	$1\cdot10^{-4}$	0.36	5000

[1] qudrupole coupling constant, * effective values used in the simulations)

temperature phase to hexagonal in high temperature phase [20, 23]. Pronounced changes of the T_1 and T_2 data and ^2H NMR spectra were observed for this system at the phase transition, which were associated to the abrupt change in the dynamic

properties of the guest molecules [7]. Above the phase transition temperature the symmetry of the urea channels allows the alkyl chains to rotate rapidly and almost unrestrictedly around the channel long axis, while below the phase transition the alkyl chains were found to experience fast but restricted rotational motions due to the loss of the symmetry of the urea channels [7]. However, for the di- or mono-bromo-alkane/urea inclusion compounds, the bromine atom has a larger diameter (compared with that of a proton). For the 1-bromodecane included within the confined space of the urea channel, the longer C–Br bond (relative to the C–H bond) can protrude the guest molecules to move toward the channel wall, which induces a repulsive local interaction and results in some local distortion of the host structure. Thus the urea channel imposes more resistance to the motion of guest molecules. Even across the phase transition temperature, with a slightly enlarged diameter of the urea channel, the dynamic properties of the guest molecules cannot alter dramatically. That is why no discontinuity at the phase transition temperature is observed in the T_1 and T_2 curves for di- or mono-bromoalkane/urea inclusion compounds [53, 176], instead of a pronounced discontinuity for n-alkane/urea inclusion compounds [7]. It is thus found that the dynamic properties of the guest molecules continuously change with the elevating temperature even crossing the phase transition temperature. Once the effect of local distortion of the urea channels caused by the long C-Br bond (1.96 Å [22]) is eliminated by a widening of the channel diameter, the motion of the guest molecules becomes suddenly very fast. A similar discontinuity of the dynamic properties of the guest molecules at the temperature corresponding to the T_{1Z} minimum, as reflected by a discontinuity of the Arrhenius plots, is also observed for di-bromoalkane/urea inclusion compounds [44, 176].

The phenomenon, that the transition of the molecular behaviour of the guests is delayed to a higher temperature than the phase transition temperature, was also observed in stearic acid/urea inclusion compounds [195]. Raman spectroscopy showed that there were abrupt discontinuities in the behaviour of the bands from urea

at the temperature range of 232-236 K (only within an interval of 4 K), as a consequence of the phase transition centered at ~ 234 K. In contrast, the Raman bands of the guest molecule stearic acid displayed a continuous change in the range from 223 to 253 K, i.e. a transition covering ~ 30 K. Thus, it can be concluded that the molecular behaviour of the guests in urea is related to both the change of the urea lattice matrix and the type of the guest molecules, and that the structural changes of the urea host lattice do not necessarily correlate with discontinuous changes of the guest motions.

It is found from the T_{1Q} curve in Fig. 5.35 that the theoretical T_{1Q} values slightly deviate from the experimental counterparts in the low temperature phase. A possible explanation lies in the fact that T_{1Q}, which only depends on $J_1(\omega_0)$, is far more sensitive to small angle fluctuations – so far not considered in the ^{2}H NMR relaxation data analysis – than T_{1Z} which additionally contains a contribution from $J_2(2\omega_0)$ [161, 196]. The amplitude of guest fluctuation is extremely sensitive to the channel diameter [189], and this would be larger if the channel is allowed to deform. Therefore, it can be concluded that fluctuations of the guests can affect T_{1Q}, but have negligible effects on the T_{1Z} data.

For both 1-bromodecane and 1,10-dibromodecane in their urea inclusion compounds [176], the guest dynamics can both be explained in terms of the superposition of a small angle fluctuation and the aforementioned 3-site jump model in the temperature range investigated. With respect to the 3-site jump model, the comparison of the kinetic parameters for 1-bromodecane/urea and 1,10-dibromodecane/urea shows that at the same temperature, the correlation time for both is similar. However, the quadrupole coupling constant and the population of the major site are quite different. For instance, for 1-bromodecane an effective quadrupole coupling constant of 145 kHz is found at 135 K while for 1,10-dibromodecane this value is not reached until 280 K (the small angle fluctuation mainly contributes to the reduction of the spectral

width, which is reflected by the reduced quadrupole coupling constant). Likewise, for 1-bromodecane the populations of all three sites are assumed to be equal at 160 K while for 1,10-dibromodecane even at room temperature the population of major site is set as 0.36. For the 3-site jump motion in the high temperature branches of the T_{1Z} and T_{1Q} curves, the activation energy of 11 kJ/mole for 1-bromodecance is derived while 13 kJ/mole for 1,10-dibromodecane. These findings indicate that the larger number of Br substituents enhances the spatial hindrance of the overall rotation motion.

For the phase transition temperatures of urea inclusion compounds with n-decane, 1-bromodecane and 1,10-dibromodecane it is found that with an increasing number of Br substituents in the guest molecules the phase transition temperature is shifted to higher temperatures. The onset of the order-disorder transition of the guest molecules in urea is thus related to the number of the Br substituents because the interaction of the bromine with the channel wall is much stronger than for the proton, and the C-Br bond is longer than the C-H bond as well. The longer C-Br bond occupies more space of the urea channel and enhances the steric hindrance for the guest motion. These effects also give rise to the fact that the discontinuity of the guest motions for di- and mono-bromoalkane/urea inclusion compounds is shifted to a higher temperature than the solid-solid phase transition temperature for n-alkane/urea inclusion compounds. Thus, the guest-host and guest-guest interactions increase with the number of Br substituents.

5.3.4 Conclusions

For asymmetric guest molecules in urea, the end-groups of two adjacent guest molecules may arrange in three different ways: head-head, head-tail and tail-tail. Solid-state ^{1}H and ^{13}C NMR spectroscopy is used to study the structural properties of 1-bromodecane in urea. It is found that the end groups of the guest molecules are

randomly arranged. The dynamic characteristics of 1-bromodecane in urea inclusion compounds are probed by variable-temperature solid-state ^{2}H NMR spectroscopy (line shapes, spin-spin relaxation: T_2, spin-lattice relaxation: T_{1Z} and T_{1Q}) between 120 K and room temperature. Based on the assumption of a non-degenerate 3-site/6-site jump process in the low temperature phase and a degenerate 3-site/6-site jump in the high temperature phase, in combination with the small-angle wobbling motion, the experimental data can be reproduced in a quantitative way and the kinetic parameters are derived.

5.4 MAS NMR studies on selected urea inclusion compounds

5.4.1 ^{13}C CP MAS and ^{1}H MAS NMR spectra

Figure 5.37 shows high resolution ^{13}C NMR spectra of urea inclusion compounds with different guest molecules. According to previous studies [11, 103, 181], the assignments of these five urea inclusion compounds were done. They are listed in Tables 5.18 to 5.20 along with chemical shifts of these guest molecules in solution. In the ^{13}C NMR spectra of these UICs, high resolution is achieved, suggesting that the guest molecules are of high mobility. Because the guest molecules are isolated by the urea channels, dipolar coupling between the guests is reduced.

For 1-fluorodecane/urea inclusion compounds, the CH_2F group gives rise to two broadened resonances at 85.2 and 83.2 ppm due to dipolar coupling between the F nucleus and the directly bonded carbon [103] (the ^{13}C NMR spectrum is recorded with only proton decoupling), as illustrated in Fig. 5.37b. For urea inclusion compounds with asymmetric guest molecules, two adjacent guest molecules can arrange in three different ways: head-head, head-tail and tail-tail [57, 58]. The relative ratio of these arrangements depends on the interaction strength of the end functional groups [58,

176]. Thus, in 1-fluorodecane, for the CH_2F group with two different arrangements, $CH_2F…H_3C$ and $CH_2F…FH_2C$, four resonances might be observed. However, only two broadened resonances arising from the dipolar coupling between the F atom and the directly bonded carbon are registered, suggesting that the electronic environment of the carbon in the CH_2F group is not affected by the different end arrangements. Compared with dipolar coupling, the influence of the different end arrangements on the ^{13}C chemical shift in the CH_2F group is too weak to be observed. Likewise, the CH_3 group exists in two different arrangements, $CH_3…FH_2C$ and $CH_3…H_3C$. Again, due to the dipolar coupling between the F atom and its neighbour carbons [103], one resonance of the CH_3 arising from the $CH_3…FH_2C$ arrangement is pronouncedly broadened, flanking the other resonance of the CH_3 at 14.8 ppm which reflects the $CH_3…H_3C$ arrangement [103].

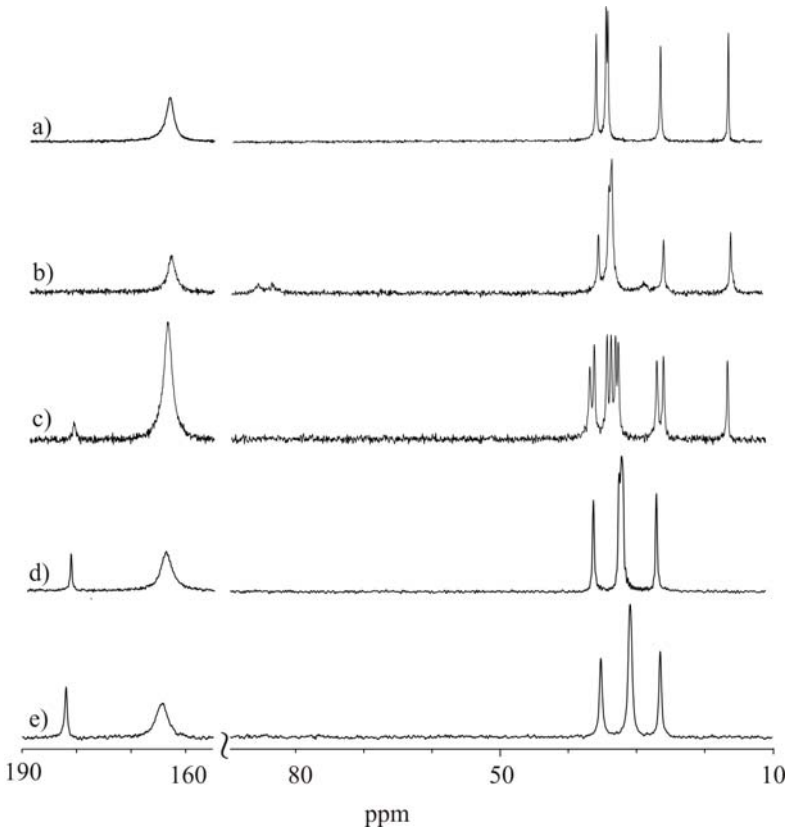

Figure 5.37 ^{13}C CP MAS NMR spectra of urea inclusion compounds with guest molecules: a) n-decane, b) 1-fluorodecane, c) decanoic acid, d) dodecanedioic acid, e) sebacic acid.

For the decanoic acid/urea inclusion compound, a surprising high resolved ^{13}C NMR spectrum is registered (see Fig. 5.37c). The chemical shift of every carbon in the chain can be distinguished. In contrast to two peaks of the end group in other asymmetric guest molecules [57, 58, 103], the resonances of the CH_3 or COOH end-group of decanoic acid display a single peak. As reported previously [23, 35, 197], the aliphatic mono-carboxylic acids form exclusively head-to-head dimers in urea channels. Thus both CH_3 and COOH end-groups have only one arrangement, i.e. $CH_3 \ldots CH_3$ and COOH…COOH which correspond to two single peaks recorded at 15.6 and 182 ppm, respectively. Spectra of dodecanedioic acids/urea, Fig. 5.37d, and sebacic acids/urea, Fig. 5.37e, are similar. The two guest molecules have the COOH groups at the both ends and thus are expected to form infinite one-dimensional intra-channel hydrogen-bonded chains of guests [23].

^{1}H MAS spectra of urea inclusion compounds containing n-alkanes with different functional groups at the chain ends are shown in Fig. 5.38. It is found that, in general, the resolution of these ^{1}H NMR spectra is very low due to the strong ^{1}H dipolar coupling.

^{13}C NMR spectra of pentadecane and hexadecane in urea and urea-d_4 are shown in Fig. 5.39. The assignments of the peaks and the ^{13}C NMR line widths are summarized in Table 5.21 along with the chemical shifts of the guest species in solution. The comparison of the ^{13}C NMR line widths in the UICs from urea and urea-d_4 shows a larger value for the guest species in urea-d_4 (see Table 5.21). Because the ^{13}C NMR spectra are recorded with only proton decoupling, ^{13}C-^{2}H dipolar coupling between the guest species and the host matrix causes the additional line broadening of the guest species in urea-d_4. However, the ^{13}C NMR line width of the urea carbonyl group is found to become smaller upon urea deuteration, which is attributed to interference effects [178, 179] between the ^{1}H decoupling r.f. field and the urea reorientation motions, i.e., 180° flips around the C=O and the C-N bonds [39, 180]. This is

supported by a broadening for the carbonyl ^{13}C NMR signal with an increase of the ^{1}H decoupler power. Similar observations were found for other UICs [44, 176].

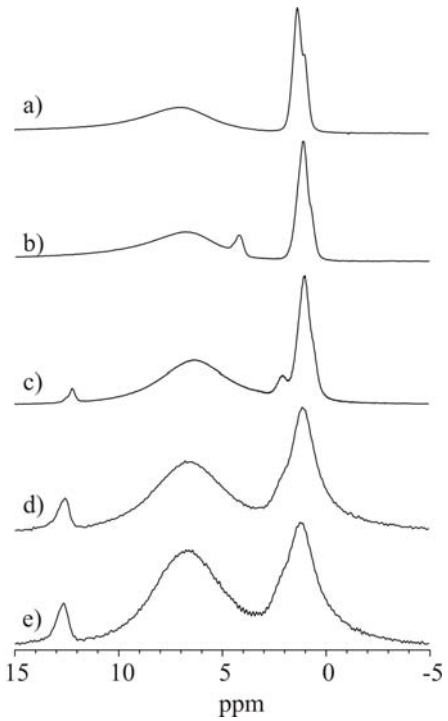

Figure 5.38 ^{1}H MAS NMR spectra of urea inclusion compounds with guest molecules: a) n-decane, b) 1-fluorodecane, c) decanoic acid, d) dodecanedioic acid, e) sebacic acid.

When the signal intensity is recorded as a function of contact time for cross-polarization, the optimum contact time with maximal signal intensity is found to vary considerably with guest species and deuteration of the urea matrix. Thus, for hexadecane/urea, a maximum ^{13}C CP signal was observed at contact times of 0.5 ms and 4 ms for urea and urea-d_4, respectively. As a consequence of the loss of the urea protons, a longer contact time is required for the deuterated urea clathrates, suggesting that the urea protons contribute to magnetization transfer during cross-polarization as well. Similar trends for the ^{13}C signal intensity during cross-polarization were also observed recently for other urea inclusion compounds [44, 176]. It is surprising that this is not found for pentadecane/urea. The contact time of 0.5 ms is found to be

suitable for the pentadecane guest molecules in both urea and urea-d_4, which can be correlated to the ^1H $T_{1\rho}$ values, as shown below in Tables 5.22 and 5.23. A ratio of about 7 of ^1H $T_{1\rho}$ in urea-d_4 to that in urea is obtained for hexadecane while a value of about 2.5 is derived for pentadecane.

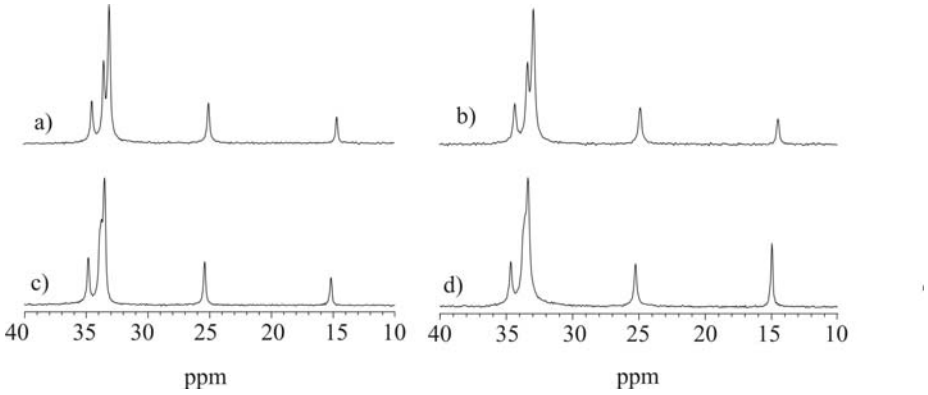

Figure 5.39 ^{13}C CP MAS NMR spectra of n-pentadecane in: a) urea, b) urea-d_4, and n-hexadecane in: c) urea, d) urea-d_4.

Figure 5.40 exhibits ^1H MAS NMR spectra recorded at a sample spinning rate of 34 kHz for pentadecane and hexadecane in urea and urea-d_4. Very low resolved ^1H NMR spectra are observed, which again indicates that there is strong ^1H dipolar coupling in these UICs.

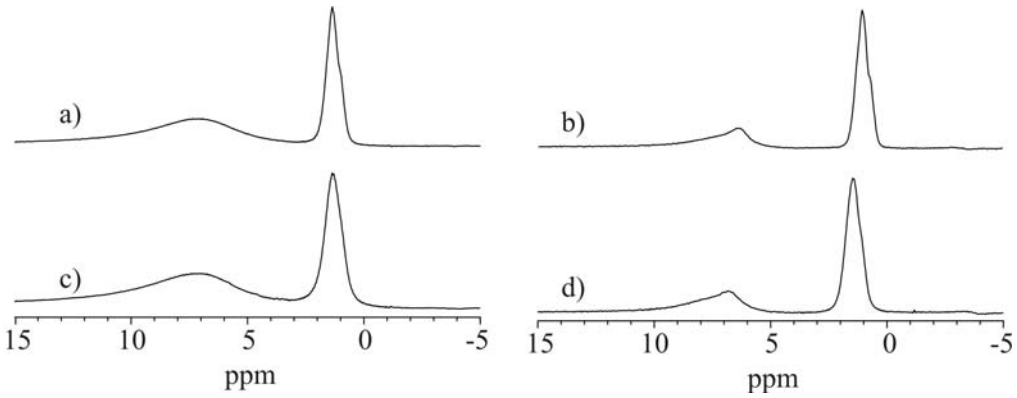

Figure 5.40 ^1H MAS NMR spectra of n-pentadecane in: a) urea, b) urea-d_4, and n-hexadecane in: c) urea, d) urea-d_4.

The comparison of the chemical shifts of the guest species in urea and in solution shows that the chemical shifts of the guest species in urea exhibit a downfield shift. As reported previously [25, 177], these chemical shift alterations can be traced back to conformational changes. On the basis of these observations and the results from ^{2}H NMR, Raman, IR and X-ray investigations [4-7, 11, 25, 177], it was concluded that the guest species in urea adopt a nearly all-trans conformational state while in solution a fast equilibrium between gauche and trans conformers exists. For the methyl group in n-alkane and in decanoic acid, these effects are less pronounced, which can be attributed to the presence of a small fraction of gauche conformers and/or fast methyl rotation established from IR and ^{2}H NMR spectroscopy [4-7].

The ^{13}C chemical shift alteration of the dodecanedioic acid carbonyl group is much larger than that of the decanoic acid carbonyl group, which might be related to the particular situation that decanoic acid exists in head-to-head dimers with the two facing COOH groups [23, 35, 197]. These dimers can be regarded as one guest molecule, and thus the acid alkyl chains of decanoic acid/urea have conformations similar to those of the pure n-alkane chain. This was also reported previously [4, 26, 35, 195]. However, the dodecanedioic acid forms one-dimensional infinite intra-channel chains by hydrogen-bonds [23]. It might well be that in the latter case a stronger hydrogen bond occurs which gives rise to the larger change of the chemical shift value.

5.4.2 $T_1(C)$, $T_{1\rho}(C)$ and $T_{1\rho}(H)$ relaxation data

The dynamic properties of the guest components are assessed by ^{13}C $T_{1\rho}$, ^{13}C T_1 and ^{1}H $T_{1\rho}$ measurements. The derived data are summarized in Tables 5.18, 5.19, 5.20, 5.22 and 5.23. In general each proton of the guest molecule has the same ^{1}H $T_{1\rho}$ value (apart from the COOH group due to the large steric hindrance of the COOH group, and the methyl group which has a smaller value because of the rotation of the methyl group) due to the strong proton spin diffusion.

Table 5.18 NMR parameters from ^{13}C CP MAS and ^{1}H MAS NMR studies on n-decane/urea.

$C_{10}H_{22}$/urea	δ [ppm]		$T_{1\rho(H)}$	$T_{1\rho(C)}$	$T_{1(C)}$
CT[a]: 1.5ms	solution[b]	urea[c]	[ms]	[ms]	[s]
C1	14.2	15.1	4.1	247	1.8
C2	22.9	25.2	9.7	301	3.8
C3	32.2	34.8	9.2	255	4.3
C4	29.6	33.1	10	271	4.8
C5	29.9	33.3	10	223	4.6

[a] contact time

[b] ^{13}C chemical shifts of n-decane in $CDCl_3$ [181]

[c] ^{13}C chemical shifts of n-decane in their UICs in this work

For 1-fluorodecane/urea, the ^{13}C $T_{1\rho}$ values of all carbons within the chains are identical and rather small (see table 5.19), which can be related to the fast overall chain rotation of the guest molecules. ^{13}C T_1 values of all carbons within the chains are much longer than ^{13}C $T_{1\rho}$ values. The methyl group in the $CH_3…CH_3$ arrangement has a smaller ^{13}C T_1 value compared to other carbons in the chains, which is attributed to the fast methyl group rotation as observed for n-alkane/urea inclusion compounds. Again, a similar ^{13}C T_1 value is recorded for all other carbons within the chains. Obviously, there is no efficient relaxation process present which affects ^{13}C T_1 relaxation.

For decanoic acid, dodecanedioic acid and sebacic acid, the ^{13}C $T_{1\rho}$ and ^{13}C T_1 values of the carboxyl group are relatively large (see table 5.20), which can be attributed to the formation of hydrogen bonds between the guests and guests and the reduced internal conformational mobility. The head-to-head arrangement is a tight unit as a result of strong hydrogen bonding and the conformation of the chain in the proximity of the molecular head is quite rigid [198].

Table 5.19 NMR parameters from ^{13}C CP MAS and ^{1}H MAS NMR studies on 1-fluorodecane/urea.

$C_{10}H_{21}F$/urea	δ [ppm]	$T_{1\rho(H)}$	$T_{1\rho(C)}$	$T_{1(C)}$
CT[a]: 6ms	urea[b]	[ms]	[ms]	[s]
C1+F	85.2			
C1+F	83.2			
C2	32.5	10	6.7	8.5
C3	27.8			
C4-7	32.9	9.5	6.0	6.8
C8	34.5	11	6.7	8.5
C9	24.8	11	7.2	8.5
C10…C10	14.8	9.3	6.2	4.6

[a] contact time

[b] ^{13}C chemical shifts of 1-fluorodecane in their UICs in this work

The ^{13}C $T_{1\rho}$ and ^{13}C T_1 values of the decanoic acid are position-dependent, the ^{13}C $T_{1\rho}$ and ^{13}C T_1 values increase towards the two ends of the dimers. Although ^{2}H NMR studies on monocarboxylic acids/urea show that the monocarboxylic monomers or dimers experience a fast uniform rotation diffusion about the c-axis on the ^{2}H NMR time-scale [4], it is also shown that alkanoic acid chains wobble slowly at a limited angle about a perpendicular arc [4]. This slower and limited wobbling motion might explain the ^{13}C $T_{1\rho}$ and ^{13}C T_1 values of the decanoic acid, which is consistent with the position-dependent behaviour of ^{13}C $T_{1\rho}$ and ^{13}C T_1 values.

The position-dependent ^{13}C $T_{1\rho}$ and ^{13}C T_1 values of the decanoic acid might also reflect the presence of some internal chain mobility. This is supported by ^{2}H NMR studies on single-crystals of monocarboxylic acids/urea compounds with n = 8, 12 and 16 at ambient temperature with the long axis of the crystal perpendicular to the static magnetic field. For the spectra of the three compounds doublets for methyl and bulk

Table 5.20 NMR parameters from ^{13}C CP MAS and ^{1}H MAS NMR studies on sebacic acid, dodecanedioic acid, and decanoic acid in urea.

$HOOCC_8H_{16}COOH$/urea					
CT[a]: 1ms	δ [ppm]		$T_{1\rho(H)}$	$T_{1\rho(C)}$	$T_{1(C)}$
	solution[b]	urea[c]	[ms]	[ms]	[s]
COOH		182	1.3	514	5.6
C2		35.2	1.5	187	2.3
C3		26.5	1.6	194	2.1
C4-5		30.9	1.5	175	2.4
$HOOCC_{10}H_{20}COOH$/urea (CT[a]: 0.3ms)					
COOH	174	182	0.8	292	2.3
C2	33.6	35.6	1.1	177	3.4
C3	24.5	26.3	1.1	194	3.1
C4	28.8	31.8	1.1	161	2.9
C5-6	28.7	31.4	1.1	177	3.3
$CH_3C_8H_{16}COOH$/urea (CT[a]: 1ms)					
COOH	181	182	3.5	408	5.7
C2	34.3	36.1	4.0	139	2.5
C3	24.8	26.1	4.1	164	2.3
C4	29.2	31.9	4.2	216	2.9
C5	29.4	32.3	4.3	189	2.3
C6	29.5	33.5	4.1	157	2.6
C7	29.4	32.9	4.0	162	2.9
C8	32.0	35.4	4.3	196	3.1
C9	22.8	25.1	4.1	232	3.4
C10	14.1	15.6	4.2	259	4.0

[a] contact time

[b] ^{13}C chemical shifts of sebacic acid, dodecanedioic acid, and decanoic acid in $CDCl_3$ [181]

[c] ^{13}C chemical shifts of sebacic acid, dodecanedioic acid, and decanoic acid in their UICs in this work

methylene deuterons were observed and for the longer chain guests separate signals for penultimate methylene groups were resolved as well [4]. From the data analysis it was shown that at room temperature a small gauche population occurs near the methyl end of the alkanoic acid chains.

Unlike the position dependence of ^{13}C $T_{1\rho}$ and ^{13}C T_1 values of decanoic acid, for dodecanedioic acid and sebacic acid the ^{13}C $T_{1\rho}$ and ^{13}C T_1 values at different positions in the chain are almost identical (with the exception of carboxyl carbon due to larger spatial hindrance of two facing COOH groups), which implies that there is no internal chain mobility for these two UICs as for monocarboxylic acids/urea. The dicarboxylic acids in urea have two COOH groups at both chain ends, and thus form infinite H-bonded chains [23]. Hence the guest chain may experience fast and uniform motion and this motion is too fast to affect ^{13}C $T_{1\rho}$ and ^{13}C T_1 relaxation.

For hexadecane/urea and pentadecane/urea it is found that the ^{13}C $T_{1\rho}$ values slightly vary with chain position, as reflected by a $T_{1\rho}$ decrease towards the center of the chain (see Tables 5.22 and 5.23). This finding indicates that besides the rapid rotation of the overall chains established by ^2H NMR studies [4-7], the guest molecules also possess internal chain mobility, for instance, torsional libration about the penultimate C-C bond, methyl rotation about its local threefold symmetry axis C_3 and gauche-trans isomerization which were examined by ^2H NMR studies [20]. Urea deuteration is characterized by an increase for both the ^{13}C $T_{1\rho}$ and ^1H $T_{1\rho}$ values due to reduced effective hetero- and homonuclear dipolar interactions between guest and host components.

The ^{13}C T_1 values are much longer than the ^{13}C $T_{1\rho}$ values, and they both exhibit distinct position dependence. Thus, the ^{13}C $T_{1\rho}$ values decrease towards the center of the chain while ^{13}C T_1 values increase towards the center of the chain. The position-dependent ^{13}C T_1 values might reflect internal chain mobility as well. Upon urea deuteration, the ^{13}C T_1 values of the pentadecane/urea increase due to reduced

effective hetero- and homonuclear dipolar interactions between guest and host components, however the ^{13}C T_1 values of the hexadecane/urea are almost unaffected by urea deuteration. The ^{13}C T_1 and ^{1}H $T_{1\rho}$ of the end methyl groups for both samples show smaller values, as a consequence of the high mobility of end methyl which was proved by ^{2}H NMR studies [4-7].

Table 5.21 NMR parameters from ^{13}C CP MAS and ^{1}H MAS NMR studies on n-pentadecane and n-hexadecane in urea and urea-d_4.

$C_{15}H_{32}$/urea	δ_{13C} [ppm]			$\Delta\nu_{1/2(13C)}$[c] [Hz]	
	solution[a]	urea[b]	urea-d_4	urea	urea-d_4
C1	14.2	14.7	14.5	15.4	17.6
C2	22.8	25.1	24.9	17.3	21.5
C3	32.1	34.5	34.3	18.2	22.1
C4	29.5	33.1	32.9	19.3	23.1
C5-7	29.9	33.5	33.4	26.3	27.2
C=O		164	164	108	69.8
$C_{16}H_{34}$/urea-d_4					
C1	14.1	15.2	15.2	15.4	13.3
C2	22.8	25.4	25.4	16.2	17.7
C3	32.0	34.8	34.8	17.7	19.3
C4	29.5	33.5	33.5	24.5	43.3
C5-8	29.9	33.8	33.8	25.9	43.3
C=O		164	164	115	62.1

[a] ^{13}C chemical shifts of pentadecane and hexadecane in $CDCl_3$ [181]

[b] ^{13}C chemical shifts of pentadecane and hexadecane in their UICs in this work

[c] ^{13}C NMR line width

Moreover, from the variable temperature ^{13}C $T_{1\rho}$ data a minimum is found at 300 K for pentadecane/urea and 310 K for hexadecane/urea. A semi-quantitative analysis of these ^{13}C $T_{1\rho}$ relaxation data was done by using the well-known expressions [172] for

$T_{1\rho}$ in the presence of isotropic motions and a dominant heteronuclear dipolar interaction

$$\frac{1}{T_{1\rho}(^{13}C)} = \frac{A^2}{2}\left[4 \cdot J(\omega_{1,C}) + J(\omega_{0,H} - \omega_{0,C}) + 3 \cdot J(\omega_{0,C}) + 6 \cdot J\left(\omega_{0,H} + \omega_{0,C}\right) + 6 \cdot J(\omega_{0,H})\right] \quad (5.6)$$

with $$J_n\left(\omega_i\right) = \frac{\tau_c}{1 + \omega_i^2 \tau_c^2}; \qquad \omega_i = \gamma B_i \quad (5.7)$$

Here A^2 is a factor which contains the gyromagnetic ratios of the interacting nuclei, and the average internuclear distance as $<1/r^3>$. $\omega_{0,C}$ and $\omega_{0,H}$ are the Larmor frequencies of the ^{13}C and ^{1}H nuclei, respectively, and $\omega_{1,C}$ is the nutation frequency of the radio frequency field $B_1(^{13}C)$.

Table 5.22 $T_{1\rho}(C)$, $T_{1\rho}(H)$ and $T_1(C)$ values as a function of temperature for n-pentadecane in urea and urea-d_4.

$C_{15}H_{32}$/urea	$T_{1\rho(C)}$ [ms]						$T_{1\rho(H)}$	$T_{1(C)}$
(CT[a]: 0.5ms)	294K	300K	305K	310K	315K	320K	[ms][b]	[s][b]
C1	204	136	169	212	360	404	8.2	2.7
C2	189	142	189	230	246	260	6.3	4.9
C3	150	135	138	172	175	207	6.0	5.7
C4	176	136	146	173	187	202	5.8	5.9
C5-7	139	126	129	153	166	179	5.9	6.0
$C_{15}H_{32}$/urea-d_4	(CT[a]: 0.5ms)							
C1	346	240	178	262	482	574	14	4.5
C2	328	325	242	291	597	628	16	9.5
C3	289	231	198	222	355	489	16	11
C4	367	237	205	240	386	556	16	12
C5-7	298	205	186	204	311	404	16	13

[a] contact time

[b] value at 294 K

Table 5.23 $T_{1\rho}(C)$, $T_{1\rho}(H)$ and $T_1(C)$ values as a function of temperature for n-hexadecane in urea and urea-d_4.

$C_{16}H_{34}$/urea	$T_{1\rho(C)}$ [ms]							$T_{1\rho(H)}$	$T_{1(C)}$
(CT[a]: 0.5ms)	294K	300K	305K	310K	315K	320K	325K	[ms][b]	[s][b]
C1	262	248	240	131	188	255		2.4	2.6
C2	357	279	251	154	201	248		2.7	6.2
C3	235	217	204	137	172	185		2.6	8.7
C4	261	200	189	125	161	178		2.4	8.9
C5-8	184	161	161	110	138	164		2.4	9.1
$C_{16}H_{34}$/urea-d_4	(CT[a]: 4ms)								
C1	746	729	661	649	572	686	----	8.1	2.3
C2	687	668	547	507	474	545	652	14	5.4
C3	479	381	362	351	310	327	347	16	7.0
C4	595	494	407	363	314	355	402	17	7.5
C5-8	284	280	277	269	263	317	331	18	9.2

[a] contact time

[b] value at 294 K

By fitting the ^{13}C $T_{1\rho}$ minimum with equation (5.6), factor A and the correlation time τ_c of the motion corresponding to the minimum were calculated. Substituting the derived factor A back into equation (5.6), a set of correlation times as a function of temperature are obtained by fitting the experimental ^{13}C $T_{1\rho}$ curve, as summarized in Tables 5.24 and 5.25. It is found from Tables 5.24 and 5.25 that the correlation times of hexadecane are slightly longer than those of pentadecane at the same temperature, which implies that the pentadecane guest molecules have a higher mobility than hexadecane guests. This is related to the interactions between the guests and hosts, because steric repulsion between host and guest atoms dominates, longer chains have more atoms in contact with the urea channel. These findings are in agreement with the results from the ^2H NMR studies, as reflected by an approximately linear dependence of activation energies on increasing chain length for alkane guest rotation about the long axis [4, 176].

Table 5.24 The correlation times as a function of temperature for n-pentadecane in urea and urea-d_4.

$C_{15}H_{32}$/urea	correlation time τ_c [s]					
	294K	300K	305K	310K	315K	320K
C1	$6.4\cdot10^{-6}$	$2.5\cdot10^{-6}$	$1.3\cdot10^{-6}$	$8.9\cdot10^{-7}$	$4.8\cdot10^{-7}$	$4.2\cdot10^{-7}$
C2	$5.3\cdot10^{-6}$	$2.4\cdot10^{-6}$	$1.2\cdot10^{-6}$	$8.5\cdot10^{-7}$	$7.7\cdot10^{-7}$	$7.1\cdot10^{-7}$
C3	$3.8\cdot10^{-6}$	$2.5\cdot10^{-6}$	$2.2\cdot10^{-6}$	$1.2\cdot10^{-6}$	$1.1\cdot10^{-6}$	$9.2\cdot10^{-7}$
C4	$5.2\cdot10^{-6}$	$2.5\cdot10^{-6}$	$1.7\cdot10^{-6}$	$1.1\cdot10^{-6}$	$1\cdot10^{-6}$	$9.5\cdot10^{-7}$
C5-7	$3.8\cdot10^{-6}$	$2.4\cdot10^{-6}$	$1.9\cdot10^{-6}$	$1.3\cdot10^{-6}$	$1.1\cdot10^{-6}$	$1\cdot10^{-6}$
$C_{15}H_{32}$/urea-d_4						
C1	$8.8\cdot10^{-6}$	$5.6\cdot10^{-6}$	$2.5\cdot10^{-6}$	$9.6\cdot10^{-7}$	$4.7\cdot10^{-7}$	$3.9\cdot10^{-7}$
C2	$5.5\cdot10^{-6}$	$5.4\cdot10^{-6}$	$2.4\cdot10^{-6}$	$1.3\cdot10^{-6}$	$5.2\cdot10^{-7}$	$4.9\cdot10^{-7}$
C3	$6.1\cdot10^{-6}$	$4.3\cdot10^{-6}$	$2.4\cdot10^{-6}$	$1.5\cdot10^{-6}$	$7.5\cdot10^{-7}$	$5.3\cdot10^{-7}$
C4	$8\cdot10^{-6}$	$4.3\cdot10^{-6}$	$2.4\cdot10^{-6}$	$1.4\cdot10^{-6}$	$7\cdot10^{-7}$	$4.7\cdot10^{-7}$
C5-7	$6.9\cdot10^{-6}$	$3.8\cdot10^{-6}$	$2.4\cdot10^{-6}$	$1.6\cdot10^{-6}$	$8.1\cdot10^{-7}$	$6\cdot10^{-7}$

On the basis of these results it is concluded that for pentadecane and hexadecane ^{13}C $T_{1\rho}$ relaxation does not reflect the motions being responsible for ^2H T_{1Z} relaxation [7], but is governed by another motional process which occurs on a slower time-scale. It can be seen that the correlation times of ca. 10^{-6} s derived from the ^{13}C $T_{1\rho}$ data analysis are much longer than those reported previously from the quantitative ^2H T_{1Z} analysis – correlation time of ca. 10^{-10} s for rapid and almost unrestricted rotation of the alkyl chains around the channel long axis [7]. That is, the motion dominating the ^{13}C $T_{1\rho}$ relaxation is much slower than that for ^2H T_{1Z} relaxation. Chain fluctuations of the n-alkane guests may dominate ^{13}C $T_{1\rho}$ relaxation. This assumption is supported by the position-dependent behavior of ^{13}C $T_{1\rho}$ values. Lateral motion is sensitive to the variation of the distance, position and interaction between the guest and host, thus it can also provide some contribution to the ^{13}C $T_{1\rho}$ relaxation, as reflected by an increase of ^{13}C $T_{1\rho}$ values on urea deuteration.

Table 5.25 The correlation times as a function of temperature for n-hexadecane in urea and urea-d_4.

$C_{16}H_{34}$/urea	correlation time τ_c [s]						
	294K	300K	305K	310K	315K	320K	325K
C1	$9.3\cdot10^{-6}$	$8.7\cdot10^{-6}$	$8.4\cdot10^{-6}$	$2.4\cdot10^{-6}$	$9.8\cdot10^{-7}$	$6.7\cdot10^{-7}$	
C2	$1.1\cdot10^{-5}$	$8.1\cdot10^{-6}$	$7.1\cdot10^{-6}$	$2.4\cdot10^{-6}$	$1.1\cdot10^{-6}$	$8.5\cdot10^{-7}$	
C3	$7.5\cdot10^{-6}$	$6.9\cdot10^{-6}$	$6.4\cdot10^{-6}$	$2.4\cdot10^{-6}$	$1.2\cdot10^{-6}$	$1\cdot10^{-6}$	
C4	$9.5\cdot10^{-6}$	$6.9\cdot10^{-6}$	$6.4\cdot10^{-6}$	$2.4\cdot10^{-6}$	$1.2\cdot10^{-6}$	$1\cdot10^{-6}$	
C5-7	$7.4\cdot10^{-6}$	$6.2\cdot10^{-6}$	$6.1\cdot10^{-6}$	$2.4\cdot10^{-6}$	$1.2\cdot10^{-6}$	$9.4\cdot10^{-7}$	
$C_{16}H_{34}$/urea-d_4							
C1	$5.2\cdot10^{-6}$	$5\cdot10^{-6}$	$4.3\cdot10^{-6}$	$4.2\cdot10^{-6}$	$2.4\cdot10^{-6}$	$1.3\cdot10^{-6}$	
C2	$6.1\cdot10^{-6}$	$5.8\cdot10^{-6}$	$4.2\cdot10^{-6}$	$3.5\cdot10^{-6}$	$2.4\cdot10^{-6}$	$1.4\cdot10^{-6}$	$1\cdot10^{-6}$
C3	$6.7\cdot10^{-6}$	$4.8\cdot10^{-6}$	$4.3\cdot10^{-6}$	$4.1\cdot10^{-6}$	$2.4\cdot10^{-6}$	$1.7\cdot10^{-6}$	$1.3\cdot10^{-6}$
C4	$8.5\cdot10^{-6}$	$6.8\cdot10^{-6}$	$5.1\cdot10^{-6}$	$4.2\cdot10^{-6}$	$2.4\cdot10^{-6}$	$1.5\cdot10^{-6}$	$1.2\cdot10^{-6}$
C5-7	$3.7\cdot10^{-6}$	$3.5\cdot10^{-6}$	$3.4\cdot10^{-6}$	$3\cdot10^{-6}$	$2.4\cdot10^{-6}$	$1.3\cdot10^{-6}$	$1.2\cdot10^{-6}$

On the other hand, there is evidence that the motions of long alkyl chains are quite different in the middle of the chain and at its ends. In particular, NMR [199], Raman [34], and molecular dynamics [200] results have shown that in n-alkane UICs gauche defects may be localized only at the ends of the chains, in good agreement with the smaller chemical shift alteration of end carbons of the guest species in urea and in solution (see above). Despite the strong confinement of the chains by the urea channel, the end CD_3 groups and the CD_2 groups near the chain ends have more space to undergo reorientation, as proved, for instance, for nonadecane/urea by the separate ^2H NMR splittings of the α and β segments. All the other bulk CD_2 groups are in the trans conformation, and their C-D bonds are perpendicular to the channel axis. Moreover, since the conformational defects are in fast exchange, they might provide some contributions to the factor A in equation (5.6), thus give rise to the position-dependent ^{13}C $T_{1\rho}$ values of urea inclusion compounds with hexadecane and pentadecane.

Recently a comprehensive ^{13}C NMR relaxation study for a series of n-alkane/UICs was published [187]. It was shown that the ^{13}C T_1 values are almost independent of the particular chain length, and vary with the chain position. Both results were attributed to the overall and internal chain mobility, as also verified, for instance, by variable temperature ^{2}H NMR studies on n-alkane/UICs [5-7]. Similar observations as described above are obtained from the present work.

As mentioned above, the decanoic acid head-to-head dimer has some similarities with the n-alkane/urea inclusion compounds [4, 26, 35, 195]. Head-head dimers of the aliphatic monocarboxylic acids in urea channel can be regarded as one guest molecule, and the acid alkyl chains of decanoic acids/urea have conformations similar to those of the pure n-alkane chain [4, 26, 35, 195]. Therefore, the position-dependent behaviour of the ^{13}C $T_{1\rho}$ and ^{13}C T_1 values for decanoic acid is also similar to those of the n-alkane (see tables 5.18, 5.22 and 5.23).

5.4.3 Conclusions

Urea inclusion compounds with different guest species were studied by ^{13}C CP MAS and ^{1}H MAS NMR spectroscopy. It is shown that for the asymmetric guest species, the arrangement of the end groups of two adjacent guest molecules depends on the interaction strength of the end functional groups. The interaction between the guests and hosts is confirmed by ^{13}C CP/MAS NMR experiments on n-alkanes in urea and urea-d_4. Variable temperature ^{13}C relaxation studies about the n-alkanes show that chain fluctuations and lateral motion might explain the ^{13}C $T_{1\rho}$ relaxation.

Chapter 6 Summary

Urea inclusion compounds are suitable to study the dynamics of the guest molecules and the interactions between guest and guest as well as guest and host molecules under very confined spatial conditions. The understanding of the functional group interactions and the molecular dynamics can provide useful information for practical applications. In this work we have studied the dynamic properties of the guest molecules and the effect of the end functional group on the dynamics of the guest molecule as well as the structural features of urea inclusion compounds with different guest species via solid-state NMR spectroscopy.

1,10-Dibromodecane and 1,11-dibromoundecane/urea inclusion compounds

The structural features of urea inclusion compounds with the guest molecules 1,10-dibromodecane and 1,11-dibromoundecance were examined by solid-state ^{13}C CP MAS and ^{1}H MAS NMR spectroscopy. The comparison of the ^{13}C and ^{1}H chemical shifts of the guest species in urea and solution shows downfield shifts upon enclathration for both samples with 1,10-dibromodecane and 1,11-dibromoundecane, which supports an almost all-trans conformation of the guests in urea. Larger ^{13}C NMR line widths for the guest species in urea-d_4 than for the samples made from non-deuterated urea are observed, which illustrates the variation of the dipolar interactions between the guest and host compounds.

Differential scanning calorimetry shows that the phase transition for 1,10-dibromo-decane/urea occurs at 141 K and for 1,11-dibromoundecane/urea at 167 K, which mainly reflects a structural change of the urea host lattice from orthorhombic to hexagonal symmetry. The dynamic properties of urea inclusion compounds with the guest molecules 1,10-dibromodecane and 1,11-dibromoundecance selectively deuterated at both end groups, were studied by means of dynamic ^{2}H NMR spectroscopy. Variable temperature line shapes, spin-spin relaxation and spin-lattice

relaxation data were obtained between 100 K and room temperature.

The spectra at 100 K are a typical powder pattern for rigid deuterons. Upon heating the temperature, characteristic ^{2}H NMR line shapes are recorded, indicating that dynamic processes occur with rate constants in the order of the quadrupole coupling constant. No pronounced discontinuity is observed at the phase transition for both samples. At room temperature axially symmetric ^{2}H NMR spectra with a reduced spectral width are registered which reflect high mobility of the guest molecules.

By examining the various motional models, it is shown that ^{2}H NMR line shape effects can at best be reproduced by a superposition of a non-degenerate 3-site or 6-site jump model and an overall chain wobbling motion with a maximal wobbling angle of 24° at room temperature, as reflected by a reduced quadrupole coupling constant at elevated temperatures. The suitability of the assumed model for describing the dynamics of the guest molecules is supported by the good reproduction of the partially relaxed ^{2}H NMR spectra from quadrupole echo experiments in the low temperature range which reflects the angular dependence of T_2. For the 3-site or 6-site jump motion around the channel long axis in the low temperature phase below the T_{1Z} minimum, an activation energy of 4.6 kJ/mol for 1,10-dibromodecane-d_4/urea and 2.9 kJ/mol for 1,11-dibromoundecane-d_4/urea is found.

The experimental T_{1Z} relaxation curves for both samples exhibit a similar shape, two distinguishable slopes above and below T_{1Z} minima are observed, which implies different molecular processes that contribute to spin-lattice relaxation in these regimes. When reproducing the experimental T_{1Z} data in the low temperature phase with the same parameters as in the aforementioned ^{2}H NMR line shape and T_2 relaxation data analysis, it is found that all theoretical T_{1Z} values are higher than the experimental ones since the overall wobbling process is not explicitly considered to contribute to spin-lattice relaxation. In order to get correlation times for the wobbling contribution ($T_{1Z,\ wobb}$), we used a degenerate 19-site wobbling model. The derived

correlation times for the wobbling contribution follow an Arrhenius behaviour from which activation energies of 6.7 kJ/mol for 1,10-dibromodecane-d_4/urea and 3.1 kJ/mol for 1,11-dibromoundecane-d_4/urea were determined.

In the high-temperature phase, the molecular motions are too fast to affect the ^2H NMR line shapes and spin-spin relaxation data. Thus, both the spin-lattice times and the partially relaxed spectra, which reflect the T_{1Z} anisotropy from the inversion recovery experiments, have been analyzed. Both the absolute T_{1Z} values and the anisotropy can be reproduced very well with only the 3-site jump model, i.e., in the high temperature phase the contribution of the overall wobbling process to T_{1Z} relaxation was too small and T_{1Z} relaxation is dominated by the overall rotational process. For the 3-site jump motion around the channel long axis in the high temperature phase above the T_{1Z} minimum, the derived activation energy is 13.1 kJ/mol for 1,10-dibromodecane-d_4/urea and 13.8 kJ/mol for 1,11-dibromoundecane-d_4/urea.

1,6-Dibromohexane/urea inclusion compounds

The structural and dynamic properties of 1,6-dibromohexane in urea were explored by solid-state NMR spectroscopy. Samples were first checked by differential scanning calorimetry. No solid-solid state phase transitions could be observed between 130 K and the disintegration point of the inclusion compound at 337 K.

^{13}C CP/MAS NMR spectra show unusual large shifts up to about 5 ppm, which is attributed to the conformation change of the guests from the co-existence of the gauche and trans conformers in solution to exclusive gauche conformational states in urea. The interaction between guest and host is confirmed by ^{13}C CP/MAS and ^1H MAS NMR experiments on the guests in urea and urea-d_4. Compared with those of the sample made from non-deuterated urea, larger line widths of the guest species in urea-d_4 are found and deuteration of the urea host lattice is accompanied by additional resolution enhancement for the ^1H NMR signals of the guest species. These findings

reflect the changes for the intermolecular dipolar interactions between guest and host components.

The dynamic properties of the guest components were examined by ^{13}C $T_{1\rho}$, ^{13}C T_1 and ^{1}H $T_{1\rho}$ measurements. From a semi-quantitative analysis of variable temperature ^{13}C relaxation data it is found that the correlation times derived from the ^{13}C T_1 data analysis are in a very similar range as those found during the quantitative ^{2}H T_1 analysis. Thus it is concluded that (i) ^{13}C T_1 relaxation reflects the same motion being responsible for ^{2}H T_{1Z} and T_{1Q} relaxation, and (ii) ^{13}C $T_{1\rho}$ relaxation is governed by another motional process which occurs on a slower time-scale.

Variable temperature ^{2}H NMR studies were performed in a temperature range between 220 and 320 K on two samples with non-deuterated urea, and 1,6-dibromohexane deuterated either at carbons C-1/C-6 (α–positions) or at carbons C-2/C-5 (β-positions). For the lowest temperature typical axially symmetric Pake pattern (asymmetry parameter $\eta = 0.0$) are observed. Characteristic spectral alterations occur upon sample heating which imply an onset of the guest motions. The observed non-axially symmetric ^{2}H NMR spectra at higher temperatures, characterized by an averaged value of $\langle\eta\rangle \neq 0.0$, are typical for molecules undergoing motions in the fast exchange limit with a symmetry lower than C_3. It is further registered that the spectral alterations also depend on the deuterated position of the guest species.

Since spin-spin relaxation effects were not observed, the data analysis primarily relies on spin-lattice relaxation data (T_{1Z}, T_{1Q}). The quantitative analysis of the variable temperature ^{2}H NMR line shape experiments and spin-lattice relaxation studies supports the proposed non-degenerate 2-site jump model which describes mutual exchange between the two gauche conformers within the urea matrix with a jump angle of $\Delta\varphi_a = 58°$ for the α-deuterons as well as the jump angle of $\Delta\varphi_b = 109°$ for the β-deuterons. It is concluded that the gauche-gauche exchange process is the dominant source for ^{2}H and ^{13}C spin-lattice relaxation of 1,6-dibromohexane in urea. Analysis

of the T_{1Z} and T_{1Q} data provides the correlation times for this motional process. The activation energy of about 20 kJ/mol for the low temperature range is rather large, and reflects considerable spatial constraints imposed by the surrounding urea matrix. Above room temperature, a lower activation energy of about 9 kJ/mol along with a discontinuous change for the mobility is observed which is attributed to the gain in spatial freedom. Moreover, it is assumed that ^{13}C $T_{1\rho}$ relaxation is caused by overall fluctuations of the guest molecules which are also responsible for the temperature dependent reduction of the overall widths in the ^{2}H NMR spectra. Finally, an isotropic signal in the ^{2}H NMR spectra at elevated temperatures and additional resonances in ^{1}H MAS spectra of samples spun at 34 kHz are observed, which stem from free, non-clathrated 1,6-dibromohexane escaped from the urea lattice and which give evidence for lateral motions of the guests at elevated temperatures.

In general, compared with its long-chain analogues, 1,6-dibromohexane guest molecules in urea experience slower and more hindered motions. Its long-chain analogues possess an incommensurate relationship between the host and guest substructures, and the end-groups primarily adopt the trans-conformation. The host and guest substructures of the 1,6-dibromohexane UIC are thought to be commensurate. The 1,6-dibromohexane guests are therefore fixed in well-defined positions within the urea substructure. As a result, the end-groups of the incorporated 1,6-dibromohexanes are exclusively stabilized in a gauche conformational state even upon cooling down to 90 K.

1-bromodecane /urea inclusion compounds

Differential scanning calorimetry studies show that the phase transition arising from the distortion of the urea channel for 1-bromodecane/urea occurs at 133 K. The phase transition temperature is lower than the value for 1,10-dibromodecane/urea, 141 K, and higher than that for n-decane/urea inclusion compounds, 111 K. Obviously, the solid-solid phase transition is shifted to higher temperature with increasing number of Br substituents. This implies that the change in urea crystal symmetry from the

orthorhombic to the hexagonal form is affected by the Br substituent, most probably due to an increase of intermolecular interactions between the guest and host as well as guest and guest species.

The structural and dynamic properties of 1-bromodecane guest molecules in urea were investigated by solid-state NMR spectroscopy. ^{13}C CP/MAS NMR studies of 1-bromodecane/urea inclusion compounds reveal that for the CH_3 group the intensity ratio of the two resonances reflecting different end-group environments is 1:1, which implies that there is no preference for a particular arrangement of the chain ends, i.e. no preference for head-head, head-tail or tail-tail arrangement.

The dynamic properties of the 1-bromodecane guests were examined by ^{2}H NMR spectroscopy including line shape, spin-spin (T_2) and spin-lattice relaxation (T_{1Z} and T_{1Q} studies). The quantitative analysis of the experimental data shows that a non-degenerate 3-site or 6-site jump process can describe the motion of the guests in the low temperature phase while the dynamic characteristics of the guests in the high temperature phase are described by a degenerate 3-site or 6-site jump model. An activation energy of 11 kJ/mole is derived for the high temperature phase and 35 kJ/mole for the low temperature phase, which correspond to the two different slopes of the high and low temperature phases separated by T_{1Z} and T_{1Q} minima at the T_{1Z} and T_{1Q} curves, respectively. For the guest motion, a small angle fluctuation, which gives rise to a reduction of the quadrupole coupling constant in ^{2}H NMR spectra, is also considered in the whole temperature range investigated.

MAS NMR studies on selected urea inclusion compounds

Urea inclusion compounds with different guest species were investigated by ^{13}C CP MAS and ^{1}H MAS NMR experiments. ^{13}C NMR spectra of 1-fluorodecane/urea show that the methyl group gives rise to two peaks reflecting different end-group environments. However, for carboxylic acid, the resonances of the CH_3 or COOH end-group of decanoic acid display a single peak, which is attributed to the formation

of exclusively head-head dimers in the urea channels via hydrogen bonding.

Urea inclusion compounds with hexadecane and pentadecane in urea and urea-d_4 were investigated by ^{13}C CP MAS and ^{1}H MAS NMR experiments. The comparison of the ^{13}C NMR chemical shifts of the guest species in urea and in solution shows a downfield shift for the guest species in urea, and these chemical shift alterations are again traced back to conformational changes. The comparison of the ^{13}C NMR line widths in the UICs from urea and urea-d_4 shows a larger value for the guest species in urea-d_4, which reflects the change of the interaction between the guests and hosts. These findings are in good agreement with observations for α, ω-dibromodecane/urea inclusion compounds. ^{13}C relaxation studies show that the ^{13}C T_1 and ^{13}C $T_{1\rho}$ values exhibit a distinct position dependence. The ^{13}C $T_{1\rho}$ values decrease towards the center of the chain while ^{13}C T_1 values increase towards the center of the chain. They both reflect internal chain mobility. From the semi-quantitative ^{13}C $T_{1\rho}$ analysis of urea inclusion compounds with hexadecane and pentadecane, correlation times of ca. 10^{-6} s are obtained. It is argued that chain fluctuations and lateral motion of n-alkane guests may contribute to the ^{13}C $T_{1\rho}$ relaxation, although a final proof is still missing.

Chapter 7 Zusammenfassung

Harnstoff-Einschlussverbindungen sind geeignete Modellsysteme zum Studium von Gast-Gast- und Gast-Wirt-Wechselwirkungen sowie der molekularen Beweglichkeit von Gastmolekülen unter sehr eingeschränkten räumlichen Bedingungen. Der Einbau von funktionellen Gruppen kann zu einer deutlichen Veränderung dieser molekularen Eigenschaften führen, was auch für praktische Anwendungen von Relevanz ist. Im Rahmen dieser Arbeit wurde der Einfluss von funktionellen Endgruppen in verschiedenen Gastmolekülen auf die dynamischen und strukturellen Eigenschaften von Harnstoff-Einschlussverbindungen untersucht, wobei als zentrale Untersuchungsmethode die Festkörper-NMR-Spektroskopie zum Einsatz kam.

Harnstoff-Einschlussverbindungen mit 1,10-Dibromdecan und 1,11-Dibromundecan

Die konformativen Eigenschaften der Gastmoleküle in diesen Einschlussverbindungen wurde mittels ^{1}H und ^{13}C MAS NMR-Spektroskopie untersucht. Der Vergleich der ^{13}C und ^{1}H Resonanzen der Gastmoleküle in den Einschlussverbindungen und in Lösung zeigt eine deutliche Tieffeldverschiebung für die Einschlussverbindungen beider Gastmoleküle, was die Ausbildung und Stabilisierung einer all-*trans*-Konformation der Gastspezies anzeigt. Gleichzeitig werden größere ^{13}C NMR-Linienbreiten für die Einschlussverbindungen mit deuteriertem Harnstoff beobachtet, was mit intermolekularen ^{13}C-^{2}H dipolaren Kopplungen zwischen Gast- und Wirtskomponente erklärt werden kann.

In den DSC-Untersuchungen werden Fest-Fest-Phasenübergänge bei 141 K für 1,10-Dibromdecan und bei 167 K für 1,11-Dibromundecan gefunden, was im Wesentlichen mit strukturellen Veränderungen des Wirtsgitters (von orthorhombisch nach hexagonal) verbunden ist. Das Bewegungsverhalten der Gastmoleküle wurde mit dynamischen ^{2}H NMR-Verfahren (Linienprofilanalyse, Spin-Spin- und Spin-Gitter-

Relaxationsmessungen) erfasst, die einen Temperaturbereich von 100 K und 298 K abdeckt. Für diese Messungen wurden die Gastmoleküle jeweils an den Endmethylengruppen selektiv deuteriert.

Die ^{2}H NMR-Spektren bei 100 K zeigen die typische Linienform, wie sie für Proben gefunden werden, die auf der NMR-Zeitskala immobil sind. Eine Erhöhung der Probentemperatur führt zu charakteristischen Veränderungen der ^{2}H NMR-Linienformen, was auf einsetzende Bewegungen der Gastmoleküle mit Geschwindigkeitskonstanten in der Größenordnung der Quadrupolkopplungskonstanten zurückgeführt werden kann. Bei Raumtemperatur findet man wiederum ein axialsymmetrisches Pulverspektrum mit reduzierter Aufspaltung, welches eine hohe Mobilität der Gastmoleküle anzeigt. Interessanterweise zeigen sich keine ausgeprägten Diskontinuitäten der spektralen Veränderungen im Bereich der erwähnten Fest-Fest-Phasenübergänge.

Die quantitative Analyse der experimentellen Daten zeigt, dass ein 3-Site- bzw. aus Symmetriegründen ein 6-Site-Sprungmodell mit ungleich besetzten Sprungsites für die Molekülrotation um die Kettenlängsachse, kombiniert mit einem schnellen "Wobble"-Prozess (d.h. Fluktuationsprozess mit maximalem Auslenkungswinkel von 24°) im schnellen Grenzfall, für die Beschreibung der experimentellen ^{2}H NMR-Spektren am besten geeignet ist. Dies wird auch durch die gute Reproduzierbarkeit der experimentellen teilrelaxierten ^{2}H NMR-Spektren aus den Quadrupolecho-Experimenten unterstützt. Aus der Datenanalyse erhält man für den Tieftemperaturbereich unterhalb des T_{1Z}-Minimums Aktivierungsenergien von 4.6 kJ/mol und 2.9 kJ/mol für die Harnstoffeinschlussverbindungen mit 1,10-Dibromdecan bzw. 1,11-Dibromundecan.

Die experimentellen T_{1Z}-Kurven beider Einschlussverbindungen sind sehr ähnlich, wobei man oberhalb und unterhalb des T_{1Z}-Minimums verschiedene Steigungen beobachtet, was auf ein unterschiedliches Bewegungsverhalten in beiden Bereichen schließen lässt. Die berechneten T_{1Z}-Daten im Tieftemperaturbereich auf der Basis

des oben erwähnten Modells liefern generell zu große Werte. Durch die explizite Berücksichtigung des "Wobble"-Prozesses erhält man jedoch eine gute Übereinstimmung mit den experimentellen Daten. Die daraus erhaltenen Aktivierungsenergien ergeben sich für den "Wobble"-Prozess zu 6.7 kJ/mol bzw. 3.1 kJ/mol für 1,10-Dibromdecan bzw. 1,11-Dibromundecan in Harnstoff.

In der Hochtemperaturphase oberhalb des T_{1Z}-Minimums sind die Gastmolekülbewegungen so schnell, dass sie nur noch aus den Spin-Gitter-Relaxationsdaten (einschließlich Analyse der entsprechenden teilrelaxierten Spektren) ermittelt werden können. Hier trägt nur noch die Rotationsbewegung des Gastmoleküle zur Relaxation bei, während die "Wobble"-Bewegung bereits zu schnell ist. Für die Rotationsbewegungen werden hier Aktivierungsenergien von 13.1 kJ/mol und 13.8 kJ/mol für die Einschlussverbindungen mit 1,10-Dibromodecan und 1,11-Dibromoundecan ermittelt.

1,6-Dibromhexan/Harnstoff-Einschlussverbindung

Mittels Festkörper-NMR-Techniken wurden die molekularen Eigenschaften von 1,6-Dibromhexan in Harnstoff untersucht. Zunächst wurden DSC-Messungen zum Phasenverhalten durchgeführt, wobei im Bereich von 130 K bis zur Zersetzung der Einschlussverbindung kein weiterer Fest-Fest-Phasenübergang zu beobachten ist.

Die ^{13}C CP/MAS NMR-Spektren zeigen ungewöhnlich starke Tieffeldverschiebungen, die auf konformative Änderungen zurückgeführt wurden. Während in Lösung ein Gleichgewicht zwischen *gauche*- und *trans*-Konformeren existiert, liegt 1,6-Dibromhexan in der Einschlussverbindung ausschließlich in einem *gauche*-Zustand vor. Auch hier findet man Unterschiede zwischen den ^{13}C NMR-Spektren der Gastkomponente, die in undeuteriertem bzw. deuteriertem Harnstoff beobachtet wurden. In den ^{13}C NMR-Spektren für die deuterierte Harnstoffprobe findet man wiederum größere Linienbreiten, welche auf die verbleibenden ^{13}C-^{2}H dipolaren Kopplungen zurückgeführt werden können. Gleichzeitig verbessert sich die Auflösung in den ^{1}H MAS

NMR-Spektren der Gastverbindungen, was an der sehr geringen Zahl an verbleibenden Harnstoff-Protonen liegt. Beide Effekte sind also eine direkte Folge der intermolekularen Dipol-Dipol-Kopplungen zwischen den Gast- und Wirtsmolekülen.

Hinweise zum dynamischen Verhalten der Gastspezies ergeben sich aus den ^{13}C $T_{1\rho}$, ^{13}C T_1 und ^{1}H $T_{1\rho}$-Messungen. Eine semiquantitative Analyse der temperaturabhängigen ^{13}C-Relaxationsdaten zeigt, dass die ^{13}C T_1-Daten durch die gleichen Bewegungen dominiert werden wie die entsprechenden ^{2}H T_{1Z}- und T_{1Q}-Daten. Gleichzeitig deuten die ^{13}C $T_{1\rho}$-Experimente die Gegenwart eines weiteren Bewegungsprozesses an, der jedoch auf einer deutlich langsameren Skala stattfindet und vermutlich von Gesamtmolekülfluktuationen herrührt.

Temperaturabhängige ^{2}H NMR-Studien wurden im Bereich von 220 bis 320 K an Harnstoff-Einschlussverbindungen mit zwei selektiv deuterierten 1,6-Dibromhexanen (Deuterierung an der α- bzw. β-Position) durchgeführt. Bei tiefen Temperaturen findet man typische ^{2}H NMR-Pulverspektren von eingefrorenen Proben. Deutliche spektrale Veränderungen zeigen sich aufgrund einsetzender Gastmolekülbewegungen bei höheren Temperaturen. Für die höchsten Temperaturen findet man charakteristische, bewegungsgemittelte Spektren, die Molekularbewegungen niederer Symmetrie andeuten (nicht axial-symmetrische Spektren, Asymmetrieparameter $\eta \neq 0$). Weiterhin hängen die experimentellen Linienformen von der deuterierten Molekülposition ab.

Die experimentellen ^{2}H NMR-Linienprofile und Spin-Gitter-Relaxationsdaten lassen sich quantitativ mit einem 2-Site-Sprungmodell beschreiben, welches den Übergang zwischen den beiden *gauche*-Sites reflektiert. Offensichtlich wird sowohl die ^{2}H als auch die ^{13}C-Relaxation der Gastmoleküle durch diesen Bewegungsprozess dominiert. Für den Tieftemperaturbereich erhält man aus den Relaxationsdaten eine Aktivierungsenergie von ca. 20 kJ/mol, die eine ausgeprägte räumliche Behinderung durch das Wirtsgitter anzeigt. Oberhalb Raumtemperatur ist die Beweglichkeit deutlich weniger

eingeschränkt, was sich in der niedrigeren Aktivierungsenergie von 9 kJ/mol und der sprunghaften Verkürzung der Bewegungskorrelationszeiten widerspiegelt. Die ^{13}C $T_{1\rho}$-Daten werden vermutlich durch Fluktuationen der Gastmoleküle dominiert, die auch eine Abnahme der ^{2}H NMR-Spektrenbreite zur Folge haben. Bei erhöhten Temperaturen findet man in den ^{2}H NMR-Spektren ein zusätzliches isotropes Signal, was auf nicht eingeschlossenes 1,6-Dibromhexan zurückgeführt werden kann.

Zusammenfassend lässt sich feststellen, dass 1,6-Dibromhexan in Harnstoff deutlich langsamere und stärker eingeschränkte Bewegungen aufweist als die langkettigen Dibromalkane. Dies liegt in erster Linie daran, dass für die langkettigen Systeme eine Inkommensurabilität der Gast- und Wirt-Substrukturen vorliegt und die Kettenenden primär in der all-*trans*-Konformation auftreten. Für 1,6-Dibromhexan in Harbstoff wird dagegen eine Kommensurabilität diskutiert wird, d.h. die Gastmoleküle sitzen zunächst auf definierten Plätzen im Harnstoffgitter. Dadurch werden die Endgruppen ausschließlich in der *gauche*-Konformation stabilisiert, was auch noch für Temperaturen bis ca. 90 K beobachtet wird.

1-Bromdecan/Harnstoff-Einschlussverbindung

Aus kalorimetrischen Untersuchungen dieser Verbindung wurde ein Fest-Fest-Phasenübergang bei 133 K gefunden. Dieser Übergang liegt niedriger als der entsprechende Wert für den Einschluss mit 1,10-Dibromdecan (141 K) und höher als der Wert für Decan/Harnstoff (111 K). Offensichtlich steigt die Phasenübergangs-temperatur mit zunehmender Zahl an Br-Substituenten an, was vermutlich an den stärkeren intermolekularen Wechselwirkungen liegt.

Festkörper-NMR-Verfahren wurden zur molekularen Charakterisierung der Gast-moleküle eingesetzt. In den ^{13}C MAS NMR-Spektren werden zwei Methylresonanzen beobachtet, was auf unterschiedliche Einlagerungen der Gastmoleküle in diesen Systemen (Kopf-Kopf- bzw. Kopf-Schwanz-Anordnung) zurückgeführt werden kann. Offensichtlich treten die beiden Anordnungsmöglichkeiten jedoch mit gleicher

Wahrscheinlichkeit auf.

Die Bewegungsverhalten der Gastmoleküle wurden mittels dynamischer ^{2}H NMR-Verfahren (Linienprofilanalyse, Analyse von T_{1Z} und T_{1Q}-Relaxationsdaten) studiert. Die Analyse zeigt auch hier, dass – wie bereits bei den langkettigen Dibromalkanen – das Relaxationsverhalten durch einen 3-Site- bzw. 6-Site-Sprungprozess, der die Rotation der Moleküle um ihre lange Molekülachse (in der nahezu all-*trans*-Konformation) beschreibt, dominiert wird. In der Tieftemperaturphase mit Sprüngen zwischen ungleich besetzten Sprung-Sites wird eine Aktivierungsenergie von 35 kJ/mol beobachtet, während in der Hochtemperaturphase mit gleich besetzten Sprung-Sites 11 kJ/mol gefunden werden. Zusätzlich müssen über den gesamten Temperaturbereich noch schnelle "Wobble"-Bewegungen der Gastmoleküle berücksichtigt werden, was der reduzierten experimentellen Quadrupolkopplungskonstante entnommen wurde.

MAS NMR-Studien an ausgewählten Harnstoff-Einschlussverbindungen

An mehreren Harnstoff-Einschlussverbindungen mit langkettigen Alkanderivaten wurden ^{13}C CP/MAS und ^{1}H MAS NMR-Messungen durchgeführt. In den ^{13}C NMR-Spektren für 1-Fluordecan/Harnstoff findet man wiederum zwei Signale für die Methylgruppen, welches ein gleichzeitiges Vorliegen der Kopf-Kopf- und Kopf-Schwanz-Anordnung anzeigt. Bei den Monocarbonsäuren findet man dagegen nur ein einziges Signal, was durch eine Dimerbildung erklärt werden kann.

Die ^{13}C chemischen Verschiebungswerte für die Harnstoff-Einschlussverbindungen mit Hexadecan und Pentadecan deuten ebenfalls die Stabilisierung einer nahezu all-*trans*-Konformation für diese Gastkomponenten an. Gleichzeitig findet man größere ^{13}C NMR-Linienbreiten für den Komplex mit deuteriertem Harnstoff, was – wie bereits erwähnt – mit intermolekularen ^{13}C-^{2}H dipolaren Kopplungen (zwischen Gast- und Wirtskomponenten) erklärt werden kann. Ferner wurden ^{13}C T_1- und $T_{1\rho}$-Messungen durchgeführt, für die eine ausgeprägte Kettenpositionsabhängigkeit

beobachtet wird. Die semiquantitative Analyse der experimentellen ^{13}C $T_{1\rho}$-Daten liefert Korrelationszeiten im Bereich von ca. 10^{-6} s. Bis jetzt ist allerdings noch offen, ob hier laterale Bewegungen oder Fluktuationsbewegungen der Gastmoleküle für die ^{13}C $T_{1\rho}$-Relaxation verantwortlich sind.

References

[1] Atwood, J. L.; Davies, J. E. D.; MacNicol, D. D. *Inclusion Compounds*, Vol. 1-3; Academic Press: New York, **1984**.

[2] Atwood, J. L.; Davies, J. E. D.; MacNicol, D. D. *Inclusion Compounds*, Vol. 4 and 5; Oxford University Press: Oxford, **1991**.

[3] Atwood, J. L.; Davies, J. E. D.; MacNicol, D. D.; Vögtle, E. *Comprehensive Supramolecular Chemistry*, Pergamon Press: London, **1996**.

[4] Vold, R. L.; Hoatson, G. L.; Subramanian, R. *J. Chem. Phys.* **1998**, *108***,** 7305.

[5] Casal, H. L.; Cameron, D. G.; Kelusky, E. C. *J. Chem. Phys*. **1984**, *80*, 1407.

[6] Greenfield, M. S.; Vold, R. L.; Vold, R. R. *Mol. Phys*. **1989**, *66*, 269.

[7] Schmider, J.; Müller, K. *J. Phys. Chem. A* **1998**, *102*, 1181.

[8] Werner-Zwanziger, U.; Brown, M. E.; Chaney, J. D.; Still, E. J.; Hollingsworth, M. D. *Appl. Magn. Reson*. **1999**, *17*, 265.

[9] Smart, S. P.; Baghdadi, A. E.; Guillaume, F.; Harris, K. D. M. *J. Chem. Soc. Faraday Trans*. **1994**, *90*, 1313.

[10] Rubio-Pena, L.; Breczewski, T.; Bocanegra, E. H.; Madariaga, G. *Ferroelectrics* **2003**, *290*, 177.

[11] Imashiro, F.; Maeda, T.; Nakai, T.; Saika, A.; Terao, T. *J. Phys. Chem*. **1986**, *90*, 5498.

[12] Ripmeester, J., *Inclusion Compounds*, edited by: Atwood, J. L.; Davies, J. E. D.; MacNicol, D. D., Oxford University Press: Oxford, **1991**, Vol. 5, page 37.

[13] Hollingsworth, M. D.; Harris, K. D. M., *Comprehensive Supramolecular Chemistry*, Pergamon Press: London, **1996**, Vol. 6, page 177.

[14] Fukushima, K. *J. Mol. Struct*. **1976**, *34*, 67.

[15] Fukushima, K.; Sugiura, K. *J. Mol. Struct*. **1977**, *41*, 41.

[16] Gilson, D. R. F.; McDowell, C. A. *Mol. Phys.* **1961**, *4*, 125.

[17] Vashishta, P., *Fast Ion Transport in Solids,* edited by: Mundy, J. N.; Shenoy, G. K., North-Holland press: Amsterdam, **1979**.

[18] Ferry, J. D. *Viscoelastic Properties of Polymers,* Wiley press: New York, **1980**.

[19] Pastor, R. W.; Venable, R. M.; Karplus M.; Szabo, A. *J. Chem. Phys.* **1988**, *89*, 1128.

[20] Harris, K. D. M. *J. Solid State Chem.* **1993**, *106*, 83.

[21] Baghdadi, A. E.; Dufourc, E. J.; Guillaume, F. *J. Phys. Chem*. **1996**, *100*, 1746.

[22] Kanesaka, I.; Matsuzawa, S.; Ishioka, T.; Kitagawa, Y.; Ohno, K.; *Spectrochim. Acta A* **2004**, *60*, 2621.

[23] Chatani, Y.; Anraku, H.; Taki, Y. *Mol. Cryst. Liq. Cryst.* **1978**, *48*, 219.

[24] Okazaki, M.; Naito, A.; McDowell, C. A. *Chem. Phys. Lett*. **1983**, *100*, 15.

[25] Okazaki, M.; McDowell, C. A. *J. Mol. Struct.* **1984**, *118*, 149.

[26] Meirovitch, E.; Belsky, I. *J. Phys. Chem*. **1984**, *88*, 6407.

[27] Guillaume, F.; Smart, S. P.; Harris, K. D. M.; Dianoux, A. J. *J. Phys.: Condens. Matter*. **1994**, *6*, 2169.

[28] Smart, S. P.; Guillaume, F.; Harris, K. D. M.; Sourisseau, C.; Dianoux, A. J. *Phys. B* **1992**, *180&181*, 687.

[29] Girard, P.; Aliev, A. E. Guillaume, F.; Harris, K. D. M.; Hollingsworth, M. D.; Dianoux, A. J.; Jonsen, P. *J. Chem. Phys.* **1998**, *109*, 4078.

[30] Segre, U.; Brustolon, M.; Maniero, A. L.; Bonon, F. *J. Phys. Chem.* **1993**, *97*, 2904.

[31] Brustolon, M. *Radiat. Phys. Chem*. **1995**, *45*, 953.

[32] Bonon, F.; Brustolon, M.; Maniero, A. L.; Segre, U. *Appl. Magn. Reson.* **1992**, *3*, 779.

[33] Menziani, M. C.; de Benedetti, P. G.; Segre, U.; Brustolon, M. *Mol. Phys.* **1997**, *92*, 903.

[34] EI Baghdadi, A.; Guillaume, F. *J. Raman Spectrosc.* **1995**, *26*, 155.

[35] Davies, J. E. D.; Tabner, V. A. *J. Incl. Phenom. Macro.* **1998**, *31*, 99.

[36] Smith, A. E. *Acta Crystallogr*. **1952**, *5*, 224.

[37] Forst, R.; Jagodzinski, H.; Boysen, H.; Frey, F. *Acta Crystallogr*. **1986**, *B43*, 187.

[38] Forst, R.; Jagodzinski, H.; Boysen, H.; Frey, F. *Acta Crystallogr*. **1989**, *B46*, 70.

[39] Heaton, N. J.; Vold, R. L.; Vold, R. R. *J. Am. Chem. Soc.* **1989**, *111*, 3211.

[40] Heaton, N. J.; Vold, R. L.; Vold, R. R. *J. Magn. Reson.* **1989**, *84*, 333.

[41] Aliev, A. E.; Smart, S. P.; Harris, K. D. M. *J. Mater. Chem*. **1994**, *4*, 35.

[42] Huang, Y.; Vold, R. L.; Hoatson, G. L. *J. Chem. Phys*. **2006**, *124*, 104504.

[43] Aliev, A. E.; Harris, K. D. M.; Champkin, P. H. *J. Phys. Chem. B* **2005**, *109*(49), 23342.

[44] Yang, X.; Mueller, K. *J. Mol. Struct.* **2007**, *831*, 75.

[45] Spiess, H. W.; Sillescu, H. *J. Magn. Reson*. **1981**, *42*, 381.

[46] Spiess, H. W. *J. Chem. Phys*. **1980**, *72*, 6755.

[47] Ronald, Y. D. *J. Magn. Reson*. **1986**, *66*, 422.

[48] Kurze, V.; Steinbauer, B.; Huber, T.; Beyer, K. *Biophys. J*. **2000**, *78*, 2441.

[49] Griffin, R. G. *Methods Enzymol.* **1981**, *72*, 108.

[50] Davis, J. H. *Biochim. Biophys. Acta* **1983**, *737*, 117.

[51] Spiess, H. W. *Adv. Polym. Sci.* **1985**, *66*, 23.

[52] Greenfield, M. S.; Vold, R. L.; Vold, R. R. *J. Chem. Phys.* **1985**, *83*, 1440.

[53] Aliev, A. E.; Smart, S. P.; Shannon, I. J.; Harris, K. D. M. *J. Chem. Soc., Faraday Trans.* **1996**, *92(12)*, 2179.

[54] Elizabe, L.; Baghdadi, A. E.; Smart, S. P.; Guillaume, F.; Harris, K. D. M. *J. Chem. Soc. Faraday Trans*. **1996**, *92*, 267.

[55] Hollingsworth, M. D.; Werner-Zwanziger, U.; Brown, M. E.; Chaney, J. D.; Huffman, J. C.; Harris, K. D. M.; Smart, S. P. *J. Am. Chem. Soc*. **1999**, *121*, 9732.

[56] Hoatson, G. L.; Tse, T. Y.; Vold, R. L. *J. Magn. Reson*. **1992**, *98*, 342.

[57] Hollingsworth, M. D.; Palmer, A. R. *J. Am. Chem. Soc*. **1993**, *115*, 5881.

[58] Hollingsworth, M. D. *N. Cyr, Mol. Cryst. Lip. Cryst*. **1990**, *187*, 135.

[59] Bengen, M. F. (Farbenindustrie, I. G.) *Ger. Pat. Appl.* OZ **1940**, 123438; Bengen, M. F. *Ger. Pat.* **1953**, 869070 (*Chem. Abstr*. **1954**, *48*, 11479c).

[60] Bengen, M. F.; Schlenk, W.; Jr, *Experientia*, **1949**, *5*, 200.

[61] Bengen, M. F. *Angew. Chem.* **1951**, *63*, 207.

[62] Hermann, C.; Lenne, H. –U. *Naturwissen*. **1952**, *39*, 234.

[63] Hollingsworth, M. D.; Brown, M. E.; Santarsiero, B. D.; Huffman, J. C.; Goss, C. R. *Chem. Mater*. **1994**, *6*, 1227.

[64] McAdie, H. G.; Forst, G. B. *Can. J. Chem*. **1958**, *36*, 635.

[65] McAdie, H. G. *Can. J. Chem*. **1962**, *40*, 2195.

[66] Harris, K. D. M. *J. Phys. Chem. Solids* **1992**, *53*, 529.

[67] Harris, K. D. M.; Thomas, J. M. *J. Chem. Soc., Faraday Trans*. **1990**, *86*, 2985.

[68] Mullen, D.; Hellner, E. *Acta Crystallogr, Sect. B* **1978**, *34*, 1624.

[69] Fetterly, L. C., *Resins Analysis*, edited by: Lappelmeier, C. P. A., Wiley: New York, **1959**, chap. XV-B.

[70] George, A. R.; Harris, K. D. M. *J. Mol. Graphics* **1995**, *13*, 138.

[71] Lee, S.; Kariuki, B. M.; Harris, K. D. M. *New J. Chem*. **2005**, *29*(10), 1266.

[72] Rennie, A. J. O.; Harris, K. D. M. *J. Chem. Phys*. **1992**, *96*, 7117.

[73] Otto, J. *Acta Crystallogr*. *B* **1972**, *28*, 543.

[74] Hollingsworth, M. D.; Goss, C. R. *Mol. Cryst. Lip. Cryst*. **1992**, *43*, 219.

[75] Hollingsworth, M. D.; Santarsiero, B. D.; Harris, K. D. M. *Angew. Chem. Int. Ed. Engl*. **1994**, *33*, 649.

[76] Brown, M. E.; Hollingsworth, M. D. *Nature* **1995**, *376*, 323.

[77] Harris, K. D. M.; Smart, S. P.; Hollingsworth, M. D. *J. Chem. Soc. Faraday Trans*. **1991**, *87*, 3423.

[78] Shannon, I. J.; Stainton, N. M.; Harris, K. D. M. *J. Mater. Chem*. **1993**, *3*, 1085.

[79] Harris, K. D. M.; Hollingsworth, M. D. *Proc. R. Soc. London, A* **1990**, *431*, 245.

[80] Fukao, K.; Miyaji, H.; Asai, K. *J. Chem. Phys*. **1986**, *84*, 6360.

[81] Hollingsworth, M. D.; Brown, M. E.; Hillier, A. C.; Santarsiero, B. D.; Chaney, J. D. *Science* **1996**, *273*, 1355.

[82] Lauritzen Jr, J. I. *J. Chem. Phys*. **1958**, *28*, 118.

[83] Mahdyarfar, A.; Harris, K. D. M. *J. Chem. Soc., Chem. Commun*. **1993**, 51.

[84] Parsonage, N. G.; Pemberton, R. C. *Trans. Faraday Soc*. **1967**, *63*, 311.

[85] Pemberton, R. C.; Parsonage, N. G. *Trans. Faraday Soc*. **1965**, *61*, 2112.

[86] Pemberton, R. C.; Parsonage, N. G. *Trans. Faraday Soc*. **1966**, *62*, 553.

[87] Cope, A. F. G.; Parsonage, N. G. *J. Chem. Thermodyn*. **1969**, *1*, 99.

[88] Fukao, K. *J. Chem. Phys*. **1990**, *92*, 6867.

[89] Fukao, K.; Horiuchi, T.; Taki, S.; Matsushige, K. *Mol. Cryst. Lip. Cryst*. **1990**, *180B*, 405.

[90] Chatani, Y.; Taki, Y.; Tadokoro, H. *Acta Crystallogr*. **1977**, *B33*, 309.

[91] Isfort, O.; Geil, B.; Fujara, F. *J. Magn. Reson*. **1998**, *130*, 45.

[92] Dong, R. Y.; Richards, G. M. *Chem. Phys. Lett*. **1986**, *127*(6), 571.

[93] Canet, I.; Courtieu, J.; Loewenstein, A.; Meddour, A.; Pechine, J. M. *J. Am. Chem. Soc*. **1995**, *117*, 6520.

[94] Domenici, V.; Madsen, L. A.; Choi, E. J.; Samulski, E. T.; Veracini, C. A. *Chem. Phys. Lett*. **2005**, *402*, 318.

[95] Taylor, A. M.; Gröbner, G.; Williamson, P. T. F.; Watts, A. *Biochemistry-us* **1999**, *38*, 11172.

[96] Drobnies, A. E.; van der Ende, B.; Thewalt, J. L.; Cornell, R. B. *Biochemistry-us* **1999**, *38*, 15606.

[97] Prosser, R. S.; Davis, J. H. *Biochemistry-us* **1992**, *31*, 9355.

[98] Prosser, R. S.; Davis, J. H. *Biophys. J*. **1994**, *66*, 1429.

[99] Glaubitz, C.; Burnett, I. J.; Gröbner, G.; Mason, A. J.; Watts, A. *J. Am. Chem. Soc*. **1999**, *121*, 5787.

[100] Torchia, D. A.; Szabo, A. *J. Magn. Reson.* **1982**, *42*, 107.

[101] Smaalen, S. V. *Crystallogr. Rev*., **1995**, *4*, 79.

[102] Forst, R., Boysen, H., Frey, F., Jagodzinski, H., Zeyen, C. *J. Phys. Chem. Solids*, **1986**, *47*, 1089.

[103] Nordon, A.; Harris, R. K.; Yeo, L.; Harris, K. D. M. *Chem. Commun*. **1997**, 2045.

[104] Parsonage, N. G.; Staveley, A. K., *Disorder on Crystals*, edited by: Rowlinson, J. S.; Baldwin, J. E., Clarendon Press: Oxford, **1978**.

[105] Frank, S. G. *J. Pharmacol. Sci*. **1975**, *64*, 1585.

[106] McNicol, D. D.; McKendrick, J. J.; Wilson, D. R. *Chem. Soc. Rev*. **1978**, *7*, 65.

[107] Cope, A. F. G.; Gannon, D. J.; Parsonage, N. G. *J. Chem. Thermodyn*. **1972**, *4*, 829, 843.

[108] Macphail, R. A.; Snyder. R. G.; Strauss, H. L. *J. Chem. Phys*. **1982**, *77*, 1118.

[109] Bell, J. D.; Richards, R. E. *Trans. Faraday Soc*. **1969**, *65*, 2529.

[110] Harris, K. D. M.; Jonsen, P. *Chem. Phys. Lett*. **1989**, *154*, 593.

[111] Kobayashi, M.; Koizumi, H.; Cho, Y. *J. Chem. Phys*. **1990**, *93*, 4659.

[112] Bovey, F. A.; Mirau, P. A. *NMR of polymers*, Academic Press: New York, **1996**.

[113] Lyerla, J. R., *High resolution NMR spectroscopy of synthetic polymers in bulk*, edited by: Komoroski, R. A., VCH Press: Florida, **1986**.

[114] Schmidt-Rohr, K.; Speiss, H. W. *Multidimensional solid-state NMR and polymers*, Academic Press: New York, **1994**.

[115] McBrierty, V.; Douglass, D.; Kwei, T. *Macromolecules* **1978**, *11*, 1265.

[116] Slichter, C. P. *Principles of Magnetic resonance*, Springer-Verlag: Berlin, **1980**.

[117] Kaplan, J. I. *J. Chem. Phys*. **1958**, *28*, 278.

[118] Alexander, S. *J. Chem. Phys*. **1962**, *37*, 967.

[119] Vold, R. R., *NMR probes of Molecular Dynamics*, edited by: Tycko, R., Kluwer: Dordrecht, **1994**, Page 27.

[120] Ernst, R. R.; Bodenhausen, G.; Wokaun, A. *Princuples of Nuclear Magnetic Resonance in One and Two Dimensions*, Clarendon: Oxford, **1987**.

[121] Jeener, J. *Adv. Magn. Reson*. **1982**, *10*, 1.

[122] Mehring, M. *Principles of High Resolution NMR in Solids*, Springer-Verlag: Berlin, 2nd ed., **1983**.

[123] Abragam, A. *Principles of Nuclear Magnetisms*, Oxford University Press: London, **1961**.

[124] Spiess, H. W. *NMR Basic Principles and Progress*, edited by: Diehl, P., Fluck, E., Kosfeld, R., Springer-Verlag: Berlin, **1978**, Vol. 15.

[125] Fyfe, C. A. *Solid State NMR for Chemists*, C. F. C. Press: Ontario, **1983**.

[126] Seelg, J. Q. *Rev. Biophys*. **1977**, *10*, 353.

[127] Brink, D. M.; Satchler, G. R., *Angular Momentum*, Vol. 3, Oxford University Press Inc.: New York, 3rd ed., **1993**.

[128] Müller, K.; Meier, P.; Kothe, G. *Prog. Nucl. Magn. Reson. Spectrosc*. **1985**, *17*, 211.

[129] Wittebort, R. J.; Olejniczak, E. T.; Griffin, R. G. *J. Chem. Phys*. **1987**, *86*, 5411.

[130] Pake, G. E. *J. Chem. Phys*. **1948**, *16*, 327.

[131] Powles, J. G.; Strange, J. H. *Proc. Phys. Soc*. **1963**, *82*, 6.

[132] Vega, A. J.; Luz, Z. *J. Chem. Phys*. **1987**, *86*, 1803.

[133] Gordon, R. G.; Messenger, T., *Electronic Spin Relaxation in Liquids*, edited by: Muus, L. T., Atkins, P. W., Plnum: New York, **1972**, page 341.

[134] Farrar, T. C.; Becker, E. D. *Pulse and Fourier Transform NMR*, Academic Press: New York, **1971**.

[135] Jeffrey, K. R. *Bull. Magn. Reson*. **1981**, *3*, 69.

[136] Heaton, N. J., Vold, R. R., Vold, R. L. *J. Magn. Reson*. **1988**, *77*, 572.

[137] Wimperis, S. *J. Magn. Reson*. **1990**, *86*, 46.

[138] Hoatson, G. L. *J. Magn. Reson*. **1991**, *94*, 152.

[139] Brown, M. J.; Hoatson, G. L.; Vold, R. L. *Solid State Nucl. Magn. Reson*. **1996**, *6*, 167.

[140] Schmidt, C.; Bluemich, B.; Spiess, H. W. *J. Magn. Reson*. **1988**, *79*, 269.

[141] Torchia, D. A.; Szabo, A. *J. Magn. Reson*. **1982**, *49*, 107.

[142] Hoatson, G. L.; Vold, R. L.; Tse, T. Y. *J. Chem. Phys*. **1994**, *100*, 4756.

[143] Greenfield, M. S.; Ronemus, A. D.; Vold, R. L.; Vold, R. R.; Ellis, P. D.; Raidy, T. E. *J. Magn. Reson*. **1987**, *72*, 89.

[144] Villanueva-Garibay, J. A.; Müller, K. *Lect. Notes Phys.* **2006**, *684*, 65.

[145] McConnell, H. M. *J. Chem. Phys*. **1958**, *28*, 430.

[146] Johnson, C. S. Jr., *Advances in Magnetic Resonance*, edited by: Waugh, J. S., Academic: New York, **1965**, Vol. 1, page 33.

[147] Hirschinger, J.; English, A. D. *J. Magn. Reson*. **1989**, *85*, 542.

[148] Hirschinger, J.; Miura, H.; Gardner, K. H. English, A. D. *Macromol*. **1990**, *23*, 2153.

[149] Hirschinger, J.; Kranig, W.; Spiess, H. W. *Coll. Poly. Sci*. **1991**, *269*, 993.

[150] Redfield, A. G. *Adv. Magn. Reson*. **1965**, *1*, 1.

[151] Baldo, M.; Grassi, A.; Perly, B. *Mol. Phys*. **1988**, *64*, 51.

[152] Halstead, T. K.; Metcalfe, K.; Jones, T. C. *J. Magn. Reson*. **1982**, *47*, 292.

[153] Wittebort, R. J.; Szabo, A. *J. Chem. Phys*. **1978**, *69*, 1722.

[154] Ebelhäuser, R., Spiess, H. W. *Ber. Bunsen-Ges. Phys. Chem*. **1985**, *89*, 1208.

[155] Beshah, K.; Olejniczak, E. T.; Griffin, R. G. *J. Chem. Phys*. **1987**, *86*, 4730.

[156] Wimperis, S. *J. Magn. Reson*., **1989**, *83*, 509.

[157] Müller, K. *Phys. Chem. Chem. Phys*. **2002**, *4*, 5515.

[158] Liebelt, A.; Detken, A.; Müller, K. *J. Phys. Chem. B* **2002**, *106*, 7781.

[159] Gelerinter, E.; Luz, Z.; Poupko, R.; Zimmermann, H. *J. Phys. Chem*. **1990**, *94*, 8845.

[160] Poupko, R.; Furman, E.; Müller, K.; Luz, Z. *J. Chem. Phys*. **1991**, *95*, 407.

[161] Vold, R. R.; Vold, R. L. *Adv. Magn. Opt. Res*. **1991**, *16*, 85.

[162] Ronemus, A. D.; Vold, R. R.; Vold, R. L. *J. Chem. Soc., Faraday Trans*. **1988**, *84*, 3761.

[163] Stejskal, E. O.; Schaefer, J.; Sefcik, M. D.; McKay, R. A. *Macromol*. **1981**, *14*, 275.

[164] Schaefer,J.; Stejskal, E. O.; Buchdahl, R. *Macromol*. **1977**, *10*(2), 384.

[165] Torchia, D. A. *J. Magn. Reson.* **1978**, *30*, 613.

[166] Andrew, E. R. *Progr. NMR. Spectrosc*. **1971**, *8*, 1.

[167] Andrew, E. R.; Hinshaw, W. S. *Phys. Lett*. **1973**, *43A*, 113.

[168] Andrew, E. R.; Hinshaw, W. S.; Riffen, R. S. *Phys. Lett*. **1973**, *46A*, 57.

[169] Pines, A.; Gibby, M. G.; Waugh, J. S. *J. Chem. Phys*. **1973**, *59*, 569.

[170] Haeberlen, U. "*High Resolution NMR in Solids: Selective Averaging*": *Adv. Magn. Reson*. **1976**, Suppl. 1.

[171] Hartmann, S. R.; Hahn, E. L. *Phys. Rev*. **1962**, *128*, 2042.

[172] Harris, R. K. *Nuclear Magnetic Resonance Spectroscopy*, Pitman Press: London, **1983**.

[173] Westermark, B. *J. Labelled Compd. Rad*. **1988**, *25*, 1381.

[174] Oldfield, E.; Meadows, M.; Rice, D.; Jacobs, R. *Biochem*. **1978**, *14*, 2727.

[175] Cobas, J. C.; Sardina, F. J. *Concept Magn. Reson. A*, **2003**, *19A*, 80.

[176] Yang, X.; Mueller, K., in preparation.

[177] Handel, T.; Lissner, F.; Schleid, T.; Müller, K. *Appl. Magn. Reson.* **2004**, *27*, 225.

[178] VanderHart, D. L.; Earl, W. L.; Garroway, A. N. *J. Magn. Reson.* **1981**, *44*, 361.

[179] Rothwell, W. P.; Waugh, J. S. *J. Chem. Phys.* **1981**, *74*, 2721.

[180] Williams, J. C.; McDermott, A. E. *J. Phys. Chem.* **1993**, *97*, 12393.

[181] AIST: Integrated Spectral Database System of Organic Compounds (data are provided by the National Institute of Advanced Industrial Science and Technology (Japan)).

[182] Schmidt C., Kuhn K. J., Spiess H. W. *Progr. Colloid & Polymer Sci*. **1985**, *71*, 71.

[183] Viras F., Viras K., Campbell C., King T. A., Booth C. *J. Polym. Sci. Polym. Phys*. **1991**, *29*, 1467.

[184] Francisco, C.; Vicens, G.; Angel, G. *Synthesis* **1987**, *5*, 511.

[185] Sato, F.; Sato, S.; Kodama, H.; Sato, M. *J. Organomet. Chem.* **1977**, *142*, 71

[186] Jacobsen, J. P.; Bildsoe, H. K.; Schaumburg, K. *J. Magn. Reson.* **1976**, *23*, 153.

[187] Nakaoki, T.; Nagano, H, Yanagida, T *J. Mol. Struct.* **2004**, *699*, 1.

[188] Villanueva-Garibay, J. A.; Müller, K. *J. Phys. Chem. B* **2004**, *108*, 15057.

[189] Vold, R. L.; Vold, R. R.; Heaton, N. J. *Adv. Magn. Reson*. **1989**, *13*, 17.

[190] Alemany, L. B.; Grant, D. M.; Pugmire, R. J.; Alger, T. D.; Zilm, K. W. *J. Am. Chem. Soc.*, **1983**, *105*, 2133.

[191] Roy, R. S. *J. Phys. B* **1968**, *1*, 445.

[192] Elguero, J.; Espada, M. *Anales de Quimica* (1968-1979), **1979**, *75*(9-10), 771.

[193] Wood, K. A.; Snyder, G. G.; Strauss, H. L. *J. Chem. Phys.*, **1989**, *91*, 5255.

[194] Casal, H. L. *J. Phys. Chem.*, **1990**, *94*, 2232.

[195] Casal, H. L.; Cameron, D. G.; Kelusky, E. C.; Tulloch, A. P. *J. Chem. Phys.*, **1984**, *81*(10), 4322.

[196] Vold, R. L.; Vold, R. R.; Warner, M. *J. Chem. Soc., Faraday Trans.*, **1988**, *84*, 997.

[197] Laves, F.; Nicolaides, N.; Pend, K. C. *Zeit. Krist*. **1965**, *121*, 258.

[198] Brustolon, M.; Maniero, A. L.; Marcomini, A.; Segre, U. *J. Mater. Chem*. **1996**, *6*(10), 1723.

[199] Imashiro, F.; Kuwahara, D.; Nakai, T.; Terao, T.; *J. Chem. Phys*. **1989**, *90*, 3356.

[200] Lee, K. J.; Mattice, W. L.; Snyder, R. G. *J. Chem. Phys*. **1992**, *96*, 9138.